Characteristics of Defect Modes, Slow Light, and Disorder in Photonic Crystals

by

Michelle Lynn Povinelli

B. A. Physics, University of Chicago (1997)
M. Phil. Physics, University of Cambridge (1998)

Submitted to the Department of Physics
in partial fulfillment of the requirements for the degree of

Doctor of Philosophy in Physics

at the

MASSACHUSETTS INSTITUTE OF TECHNOLOGY
[June 2004]
April 2004

Author .....
Department of Physics
April 28, 2004

Certified by .....
John D. Joannopoulos
Frances Wright Davis Professor of Physics
Thesis Supervisor

Accepted by .....
Thomas J. Greytak
Associate Department Head for Education

Characteristics of Defect Modes, Slow Light, and Disorder in Photonic Crystals

by

Michelle Lynn Povinelli

Submitted to the Department of Physics
on April 28, 2004, in partial fulfillment of the
requirements for the degree of
Doctor of Philosophy in Physics

Abstract

Chapter 1 introduces the subject of photonic crystals and reviews the basic physical principles underlying the formation of a band gap and the creation of localized defect modes. Proposed applications, fabrication techniques, and numerical simulation methods are surveyed.

Chapter 2 demonstrates the construction of 2D-like defect modes in a 3D photonic crystal with a complete gap. The modes are similar to those in 2D photonic crystals in terms of polarization, field profile, and projected band structures. The results should facilitate the implementation of 2D photonic-crystal devices in realistic 3D systems.

Chapter 3 explores the possibility of using photonic-crystal defect modes to design magnetic metamaterials: structures that exhibit magnetic properties despite the nonmagnetic character of their constituents. A synthetic magnetic moment is provided by a point-defect mode studied in Chapter 2. Quantitative analysis of the far-field radiation pattern proves that the mode has a primarily magnetic character: over 98% of the emitted power goes into magnetic multipole radiation.

Chapter 4 calculates the radiation pressure on the surface of a waveguide formed by omnidirectionally reflecting mirrors. In the absence of losses, the pressure goes to infinity as the distance between the mirrors is reduced to the cutoff separation of the waveguide mode. The divergence results from the reduction of the modal group velocity to zero, which causes slow-light magnification of the field intensity at constant power input.

Chapter 5 analyzes slow-light, band-edge waveguides for compact, integrated, tunable optical time delays. Slow group velocities at the photonic band edge give rise to large changes in time delay for small changes in refractive index, shrinking device size. Figures of merit are defined for tuning sensitivity and signal dispersion. Exact calculations for a realistic, three-dimensional grating structure are shown to be well predicted by a simple quadratic-band model, simplifying device design.

Chapter 6 derives a general, coupled-mode theory for disorder-induced scattering in strongly periodic systems. The analytical results allow the comparison of photonic-crystal waveguides to similar index-guided waveguides. In the realistic limit of weak

disorder, reflections are identical while transmission is higher for the photonic-crystal waveguide. The general results, verified by direct numerical simulations in an example system, suggest a new mechanism for the design of low-loss waveguides.

Thesis Supervisor: John D. Joannopoulos
Title: Frances Wright Davis Professor of Physics

Acknowledgments

I would like to thank my advisor, Professor John D. Joannopoulos, for the many contributions he has made to my time as a graduate student and my development as a scientist. John is truly dedicated to his students' well-being, both professional and personal. His constantly energetic attitude, optimism, can-do spirit, and results-oriented outlook have been extremely helpful in guiding my thesis work, as has been his care in maintaining a positive and collaborative environment in the Joannopoulos research group.

Special thanks also goes to Dr. Steven G. Johnson, my academic "older brother," for many hours of illuminating discussion and fruitful collaboration.

I would also like to thank all of my coworkers and colleagues who have contributed to the development of this thesis and made my time at MIT more enjoyable, including Dr. Solomon Assefa, Dr. Peter Bienstman (Ghent University, Belgium), Reginald E. Bryant, Professor Federico Capasso (Harvard University), Dr. Gabor Csanyi (University of Cambridge, U. K.), Professor Shanhui Fan (Stanford University), Dr. Michael Geis (Lincoln Laboratory), Kerwyn Casey Huang, Dr. Davide Iannuzzi (Harvard University), Mihai Ibanescu, Professor Erich P. Ippen, Aristeides Karalis, Dr. David Kielpinski, Professor Leslie A. Kolodziejski, Dr. Elefterios Lidorikis, Dr. Marko Lončar (Harvard University), Chiyan Luo, Dr. Theodore Lyszczarz (Lincoln Laboratory), Professor Nergis Mavalvala, Professor John B. Pendry (Imperial College, U. K.), Dr. Gale S. Petrich, Dr. Evan Reed, Dr. Marin Soljačić, Dr. Steven J. Spector (Lincoln Laboratory), Dr. Mariano Troccoli (Harvard University), Dr. Lorenz G. L. Wegener (Cambridge Ultrasonics, U. K.), past and present members of the MIT Women in Physics group, and Mehdi Yahyanejad, for continuous optimism and encouragement.

Financial support is gratefully acknowledged from the following sources: the Lucent GRPW Fellowship program, the MIT Karl Taylor Compton Fellowship, the Materials Research Science and Engineering Center program of the National Science Foundation under award no. DMR-940034, and the Department of Defense/Office of Naval Research MURI Grant no. N00014-01-1-0803. The work in Chapter 5 was sup-

ported by the Defense Advanced Research Projects agency under Air Force Contract #F19628-00-C-002. Opinions, interpretations, conclusions, and recommendations are those of the authors and are not necessarily endorsed by the United States Government.

Contents

List of Figures

List of Tables

Chapter 1

Introduction to Photonic Crystals

The study of photonic crystals began in 1987, when Yablonovitch [1] and John [2] simultaneously proposed that a three-dimensionally periodic dielectric structure could completely prohibit light propagation within a certain range of frequencies known as the photonic band gap. By analogy with the band gap in electronic systems, such a structure could provide a "photonic semiconductor," enabling a new means for directing the flow of light. Predicting what sort of 3D geometry would have this property, however, was not simple. In 1990, Ho *et al* identified the first structure with a complete photonic gap: a periodic arrangement of dielectric spheres in a diamond-like lattice [3]. While the diamond structure did not prove amenable to fabrication, Yablonovitch and coworkers soon achieved the first experimental demonstration of a photonic band gap using a modified geometry. Drilling a precise pattern of millimeter-sized holes in a dielectric block yielded a photonic band gap in the microwave frequency range [4].

Since that time, the field of photonic-crystal research has rapidly expanded. New classes of photonic-crystal structures (also known as photonic band-gap materials, or PBG's) have been discovered and fabricated at much smaller, micron length scales, enabling control over light in the infrared to optical range. The deliberate creation of "defects" in the periodic structures has been shown to give rise to localized electromagnetic field modes, in which light is trapped in the defect region by the photonic band gap. This new means for controlling the propagation of light has led to a variety

of novel optical phenomena and devices, including ultra-compact, wavelength-scale microcavities and waveguides. Meanwhile, improvements in computational modeling methods and a dramatic increase in computer processing speed have allowed the detailed study and accurate prediction of PBG properties. These developments are part of a general trend toward the development of microstructured materials: by engineering the microscopic geometry of a structure, novel properties not achievable with naturally-occurring materials can be obtained.

In Section 1.1, we begin by reviewing the basic concepts relevant to the study of photonic crystals, including the physical origin of the band gap and the creation of localized defect modes in photonic-crystal structures. Section 1.2 surveys the range of optical phenomena unique to photonic crystals and their possible applications. To establish a context for the theoretical work in this thesis, Section 1.3 summarizes the current development of photonic-crystal fabrication methods and experimental progress in observing photonic band gap effects. Section 1.4 describes computational methods for PBG simulation. Lastly, Section 1.5 provides an overview of the main themes and results of the thesis: characteristics of 3D defect modes, slow light, and disorder in photonic crystals.

1.1 Basic Concepts

A comprehensive introduction to the subject of photonic crystals is provided in Refs. [5, 6]. Here we summarize several basic concepts necessary for understanding the remainder of this thesis: the origin of the band gap and the creation of localized defect modes in 1-, 2-, and 3-dimensional structures.

The simplest way to understand the origin of the photonic band gap is to consider the familiar multilayer film [7], which can be regarded as a "one-dimensional photonic crystal" [5, Chap. 4]. From standard optics, we know that a sequence of dielectric layers with alternating indices of refraction n_1 and n_2 can be designed to strongly reflect light at particular wavelengths. Strong reflection arises from coherent scattering of light from each of the interlayer interfaces: when the optical thickness of each layer

is a quarter wavelength, the reflections add in phase to yield a large total value. The transmission through the film is correspondingly low, and the so-called "quarter-wave stack" forms the basis for commonly-used dielectric mirrors and thin-film filters.

Now let us consider the same phenomenon in the language of band structures, adopted from solid-state physics [8]. Any general solution of Maxwell's equations can be Fourier decomposed into a sum of modes with harmonic time dependence $e^{i\omega t}$. For any periodic structure, including the quarter-wave stack, Bloch's theorem (known as Floquet's theorem in optics) guarantees that each propagating mode can be characterized by a wave vector $\vec{k}$ within a restricted range known as the first Brillouin zone. Plotting all allowable real values of k for each ω gives the dispersion diagram, or band structure, of the multilayer film. For light propagation perpendicular to the film surface, any finite difference in index between n_1 and n_2 results in a range of frequencies for which *no* solutions exist: this is the photonic band gap. As a result, light incident from air onto the stack cannot propagate through it and is instead reflected, provided the frequency is in the band gap range. As the index contrast $\Delta n = n_1 - n_2$ increases, the frequency range for reflection gets larger. In fact, it is not necessary that the layer thicknesses satisfy the quarter-wave condition to obtain a photonic band gap, but this choice yields the largest gap and correspondingly the strongest reflection for any finite number of layers.

Now imagine selectively altering the thickness of one of the layers in the structure, leaving all the other layers unchanged. This creates a new solution of Maxwell's equations: a so-called *defect mode*. The defect mode is a localized state with a frequency within the photonic band gap. Light is trapped near the defect region due to "band-gap guidance;" on either side of the perturbed layer, the multilayer film blocks propagation. As a result, the intensity of the localized mode decays exponentially with distance away from the defect. A finite stack with a defect layer acts as a filter: for most frequencies within the band gap, transmission is low. However, a transmission peak appears at the defect mode frequency, at which light incident from air can tunnel through the film to the defect mode and out the other side.

The basic concepts of the photonic band gap and the creation of defect modes can

be extended to higher dimensions. 2D photonic crystals, two-dimensionally periodic structures that are infinite in the third direction, can block all propagation within the 2D plane. For example, lattices of dielectric rods in air tend to have a large gap for one of two possible light polarizations (labelled "TM"), while lattices of air holes in dielectric have large gaps for so-called "TE" modes. Perturbing a single rod (or hole), for example by increasing or decreasing its size, creates a "point-defect mode," which is localized to the defect region and resembles an optical microcavity. Perturbing a line of rods (or holes) creates a "linear defect," which acts like a waveguide. Unlike traditional dielectric waveguides, which confine light via total internal reflection (or index-guiding), photonic-crystal waveguides confine light via band-gap guiding. As a result, it is possible to guide light in regions with either higher *or* lower refractive index than their surroundings. This unique feature has a number of practical applications, which will be further discussed in Section 1.2.

Fortunately, as infinitely tall structures are impractical, the behavior of pure 2D photonic crystals can be approximated by "photonic-crystal slabs," 2D periodic structures with finite height [9]. Photonic-crystal slabs confine light by a combination of in-plane band-gap guiding and vertical index-guiding, allowing the creation of linear and point-defect modes (though the latter are intrinsically lossy) [10].

Three-dimensionally periodic structures have the unique property of being able to forbid propagation in *all* directions. Though these geometries are more difficult to visualize, many of the known 3D structures are variants of the originally-proposed diamond structure. The diamond structure, based on the face-centered-cubic (fcc) lattice with two "atoms" per unit cell [8], has a nearly-spherical Brillouin zone. As a result, light traveling in any direction within the crystal reflects after nearly the same propagation distance. The partial band gaps for propagation in specific directions thus tend to coincide, yielding a complete gap. Specific 3D photonic crystals geometries are further discussed below in Sects. 1.3, 1.5 and Chapter 2. The most important characteristic of defect modes in 3D photonic crystals is that they *cannot radiate*; light is completely prevented from escaping the defect modes in all three dimensions. This "radiation-free infrastructure" is attractive for a number of appli-

cations, as we discuss in the next section.

1.2 Applications

The ability to design materials to exhibit a photonic band gap, the unusual dispersion features that result, and the flexibility to design photonic-crystal defect modes with different characteristics have led to the discovery of a wide range of optical phenomena. Nonlinear photonic crystals and photonic-crystal fibers further extend the possibilities for novel behavior. In this section, we survey some of the many proposed applications of photonic crystals.

The control of light provided by a photonic band gap has a number of applications. On a fundamental level, the absence of propagating states within the photonic band gap inhibits spontaneous emission [1]. The resulting modification of atomic radiation [6, 11–14] results in applications such as low- [15] or even zero-threshold lasers. In photonic-crystal slabs, the partial (in-plane) band gap provides a useful property for the design of LED's [16] and lasers [17]: emitted light is preferentially coupled into vertical radiation. In 1D photonic crystals, the band gap can be designed such that the crystal acts as a perfect mirror: by using sufficiently high index contrasts, light is completely reflected from the surface of the mirror at *any* incident angle [18]. Such structures are known as "omnidirectional reflectors."

Photonic crystals also have very different dispersion properties than do uniform media. At the edge of the photonic band gap, the slope of the dispersion relationship goes to zero, enabling propagation at very low group velocities. Slow light enhances a variety of optical phenomena, discussed in detail in Section 1.5. Photonic crystals also have unusually-shaped, nonspherical "dispersion surfaces," or constant-frequency surfaces in wave vector space. As a result, light behaves quite differently than in a uniform medium when it refracts from an interface, leading to negative refraction [19–21], superprism phenomena [22], subwavelength imaging [23, 24], and compact spot-size conversion [25]. Backward-pointing Cerenkov radiation [26] is also a consequence of the shape of the dispersion surface.

Defect modes in photonic crystals can be designed to have various desired properties, including modal profile, symmetry, polarization, and frequency. As a result of this flexibility, a number of applications can be envisioned, using the building blocks of point- and linear-defect modes. Applications of single point-defect modes include high-Q cavities [27,28], filters [29,30], ultra-small modal volume laser cavities [31], and strong atom-field coupling for cavity QED [32]. Linear-defects, or waveguides, can be used to route light through the crystal without radiation loss. Unlike in traditional waveguides, perfect (100%) transmission can be achieved through sharp, 90-degree bends [33]. Cavities and waveguides can be combined to create a number of useful devices, such as wide-angle splitters [34], waveguide crossings with zero crosstalk [35], and channel-drop filters [29,30]. The vision of "superdense" integration is to combine many such tiny, wavelength-scale devices on a single semiconductor chip, creating complex "optical circuits" [36, 37]. Optical circuits could, for example, eventually eliminate the need for optical-to-electronic conversion in fiber optic networks, increasing available bandwidths and replacing bulky systems with compact, integrated chips.

Nonlinear photonic crystals exhibit a range of rich physical behavior, reviewed in Refs. [38, 39]. An intensity-dependent refractive index, or Kerr nonlinearity, can for example allow the creation of *self-induced* point-defect modes, stable, localized states in completely defect-free structures [40]. In general, photonic crystals can be designed to either maximize or minimize the effects of optical nonlinearities. By using defect modes to confine light in high-index regions, material nonlinearities can be enhanced, increasing the efficiency of nonlinear operations such as switching [41] and wavelength conversion [42,43], and leading to low-power nonlinear devices [41,44]. Confining light in air regions of the crystal conversely minimizes (unwanted) nonlinear effects, as well as material absorption.

Similar considerations apply to microstructured fibers, which are among the most promising technological applications of photonic band gap research. *Hollow-core fibers,* including omnidirectionally-reflecting mirrored (OmniGuide) fibers [45,46] and photonic-crystal fibers (PCF) [47, 48] confine light within hollow air regions in the

fiber, reducing material absorption loss, nonlinearities, and birefringence [49–51]. *Solid-core holey fibers* [52] alternatively confine light in high-index regions, enhancing nonlinearities. At the same time, the engineered microstructure provides flexibility in designing modal dispersion, leading to highly-efficient devices for, e.g. supercontinuum generation [53] and femtosecond four-wave mixing [54]. Solid-core holey fibers can also be designed to be single mode over a very broad wavelength range (337–1550nm or more) [55], to maintain polarization more efficiently than standard fibers [56], and to support guided modes with very large areas, useful for high-power applications [57]. While solid-core holey fibers technically employ index- rather than band-gap guiding, they are similar to photonic-crystal fibers in that engineering of the fiber microstructure is used to obtain useful nonlinear and dispersive properties.

1.3 Fabrication methods

Thanks to the absence of a fundamental length scale in Maxwell's equations, photonic band gap effects can be observed in nearly any wavelength range– given a crystal of the appropriate dimensions [5, Chap. 2]. More precisely, the wavelength of the band gap scales directly with the lattice constant for any particular photonic-crystal structure [58]. For microwave wavelengths (on the order of millimeters to centimeters), lattice constants are macroscopic and crystals can be fabricated by standard machining techniques [59]. In addition to the first experimental demonstration of a complete, 3D band gap, many photonic-crystal effects have first been demonstrated in this range. For optical wavelengths, the lattice constant is much smaller, on the order of a micron or less, making fabrication more difficult. With an eye to setting a context for the theoretical work in the remainder of this thesis, this section summarizes experimental progress in fabricating photonic crystals in the optical to infrared regime. (See also Ref. [58] for a recent review.) While 1- and 2-D periodic photonic crystals can be made relatively straightforwardly using developed techniques, the fabrication of 3-D crystals is more challenging and remains an area of active research.

1-D periodic crystals

1-D periodic photonic crystals, or multilayer films, are relatively easy to fabricate using the technology of thin-film deposition. However, the unconventionally high index contrasts necessary for the demonstration of omnidirectional reflection, for example, required innovation in materials selection and processing. The first demonstration of omnidirectional reflection was done at infrared wavelengths ($\lambda \sim 10$–15μm) using alternating tellurium ($n \sim 4.6$) and polystyrene ($n \sim 1.6$) layers with a period of 2.45μm [18]. Later work demonstrated omnidirectional reflection at optical wavelengths ($\lambda \sim$ 600–800nm) using much thinner tin sulfide/silica ($n = 2.6/1.46$) layers with a period of 170nm [60].

Planar 2-D periodic structures

Planar 2-D periodic photonic crystals, or photonic-crystal slabs, can also be fabricated fairly straightforwardly, leveraging techniques originally developed for the semiconductor electronic circuits. Fabrication methods are reviewed in [37]. Patterns are lithographically defined on the surface of a semiconductor slab, which is covered with a sensitive resist layer. In photonic crystal research, e-beam lithography is commonly used and can achieve feature sizes of 10–20nm. Following pattern definition, the semiconductor is etched away to yield the final structure. Optimizing the etching process to obtain straight vertical walls can be a challenge for photonic-crystal researchers, as typical aspect ratios are often higher than for electronic circuits.

Two major types of photonic-crystal slabs have been developed. In "membrane-type" slabs, a high-index semiconductor material is either suspended in air (e.g. GaAs air bridges) or rests on a lower-index substrate (e.g. Si on silica). In "heterostructure-type" slabs, a higher-index layer is sandwiched by upper and lower substrates with slightly lower indices (e.g. AlGaAs/GaAs/AlGaAs). In heterostructure-type slabs, waveguide modes are usually intrinsically lossy due to low vertical index contrast. Guiding of light in bulk planar slabs [61] and through line defects in planar slabs [62] have been achieved at 1.5μm, an important wavelength for applications in

telecommunications systems, leading to the realization of a number of devices including microcavities [63, 64] and bends [65].

Much taller 2-D periodic structures, which approximate pure 2-D crystals, have been fabricated by electrochemical etching of silicon, which is capable of yielding very high-aspect-ratio (10:1) holes [66].

3D layer-by-layer methods

Lithographic methods can be extended to fabricate 3-D periodic structures that are composed of vertically-stacked, planar layers. Such methods can give fine control over structural design and defect placement, but are currently at the stage of basic research: fabricating multiple layers is challenging and time-consuming, and most published structures have only a few vertical periods. Most research has focussed on the "woodpile" structure [67], which has a large gap of 17% of the midgap frequency for Si/air index contrasts. Each layer consists of parallel rods with square cross sections, and adjacent layers have perpendicular orientations. In significant early work, Lin *et al* used a repetitive deposition and etching process to fabricate five layers (1.25 vertical periods) of the woodpile structure with a band gap in the infrared range (10–14.5μm) [68]. Noda *et al* combined planar lithography with wafer-fusion techniques to further shrink the size of the woodpile structure, yielding a 12-layer structure with a band gap near 1.3μm [69] that incorporated a waveguide with a 90-degree bend. The first experimental optical characterization of designed defects in a 3D structure in the 1.3–1.5μm wavelength range has very recently been achieved by Qi *et al* in 2004 [70], using the 3D structure described in Chapter 2.

Robotic micromanipulation techniques provide another route to layer-by-layer fabrication of 3D photonic crystals. Ref. [71] used an SEM tip to pick up and position individual silica spheres of 0.9μm diameter, yielding a five-layer diamond structure. Although silica spheres in air do not have a high enough index contrast to result in a complete band gap, backfilling with a high-index material results in a crystal with a predicted complete gap of 13% for Si/air contrasts [72]. SEM-tip micromanipulation has also been used to assemble woodpile structures from premade, lithographically-

fabricated layers [73]. Resonant transmission through a designed planar defect has been demonstrated in the infrared ($\sim 4\mu$m) using this method [74].

3D "large-scale" microfabrication methods

A variety of techniques offer the potential for faster, "large-scale" fabrication of bulk 3D crystals. These include photoinduced solidification, self assembly in colloids and block copolymers, layer deposition techniques such as glancing angle deposition and autocloning, and "hole-drilling" methods.

Photo-induced solidification methods have the flexibility to make a wide variety of 3D structures. Laser light is shone on a transparent photosensitive material, which chemically solidifies in regions of high intensity. Extra material is dissolved away to yield a template structure, which must be backfilled with a higher-index medium to obtain a photonic crystal. In two-photon photopolymerization [75,76], the probability of polymerization is proportional to the intensity squared, allowing subwavelength definition of features. By moving the laser focus through the structure, arbitrary complex structures can be defined [75]. A woodpile template with log spacing of about 3μm is shown in [76]. For bulk periodic structures, the pattern can be written more quickly by using interference techniques [77–79]. Polymer cross-linking, proportional to intensity, is induced at the bright spots of an interference pattern produced by crossed laser beams. Using four beams, any 3D reciprocal lattice structure can be written, while adjusting beam polarizations and amplitudes changes the shape of the unit cell.

Colloidal self-assembly capitalizes on the natural tendency of microspheres to sediment into close-packed, face-centered-cubic lattices. Using controlled, fluid-flow assisted deposition, Ref. [80] demonstrated that very high-quality structures free of unintentional defects can be obtained using silica spheres up to 1μm in diameter. Backfilling with high-index material can give the "inverse opal" structure, which has a complete gap of 10% between the eighth and ninth bands for Si/air contrasts. Although colloidal self-assembly is restricted to this one particular 3D structure, it does produce thick (up to 20 layer) structures with huge, centimeter-scale areas composed

of single crystalline domains. Moreover, defects can potentially be defined within the bulk crystal template using photo-induced polymerization, as demonstrated in Ref. [81]. (Backfilling of the silica/polymer template has not yet been reported.)

The use of self-assembled block copolymers as photonic crystals is reviewed in Refs. [82,83]. Block copolymers self-assemble into a variety of one-, two-, and three-dimensional structures with a periodicity on the order of 10-100nm. Although the index contrast in these structures is too low to form a complete photonic band gap (e.g. $n \sim 1.59/1.51$ for a polystyrene/polyisoprene system [84]), reflectivity can be achieved in the visible range (350–500nm) [84,85]. The addition of nanoparticles that are preferentially attracted to one of the copolymer domains may result in higher index contrasts [86]. One attractive feature of such materials is their mechanical flexibility, which could be useful for certain applications.

Glancing angle deposition (GLAD) and autocloning are both modified layer-deposition methods capable of producing particular 3D structures with complete band gaps. In GLAD, silicon is deposited at an angle onto a pre-patterned substrate [87,88]. Because of "shadowing" effects, the silicon preferentially builds up on substrate protrusions. By carefully rotating the substrate, arrays of square spirals can be grown [88]. Process optimization should yield structures with complete band gaps of 15% in the optical to mid-IR range [87]. In autocloning, alternating layers of high- and low-index materials are deposited on a pre-patterned, grooved substrate, resulting in a corrugated-layer structure. Etching an array of vertical holes through the entire structure yields a photonic crystal with a predicted complete gap of about 12% [89–92]. Planar waveguides have been fabricated in Ref. [91].

Yablonovite, the first 3D photonic-crystal structure to be fabricated experimentally, is formed by drilling three sets of hole arrays into a high-index substrate. As a result, a large number of vertical layers can (at least in theory) be fabricated at once. At optical wavelengths, the "drilling" of micron-sized holes can be achieved by focused-ion-beam etching. Ref. [93] reports the fabrication of five vertical periods of a Yablonovite-like structure with a partial band gap in the mid-infrared. An alternative method uses x-ray sensitive lithography [94,95]. Here, the "holes" are made by

exposing x-ray beams through a patterned mask onto an x-ray sensitive resist. After dissolving away the exposed regions, the resulting template is backfilled and inverted. Ref. [95] used a combination of x-ray and e-beam lithography to pattern linear defects within a nickel Yablonovite structure. Such techniques should also be useful for fabricating the broader class of slanted pore structures proposed in Ref. [96].

Fibers

A variety of microstructured fibers have successfully been fabricated, and both OmniGuides and holey fibers are starting to enter the commercial market. OmniGuides have been fabricated with high transmission for a scalable wavelength between 0.75 and 10.6μm [50] and external reflection near 1.55μm [97]. A multilayer film with layer thicknesses on the order of 10's of microns is first rolled into a tube and then processed in a fiber draw tower, resulting in a fiber with submicron layer thickness. Holey photonic-crystal fibers are also made by drawing down larger preforms, made of stacked silica capillaries [47, 51–53].

1.4 Computational methods

Because Maxwell's equations are linear, the governing equations for photonic crystals can be very accurately solved, leading to nearly exact predictions of physical behavior. A variety of methods have been developed for the efficient computational modeling of photonic crystals; here we summarize several of the most common. Of these, the plane-wave expansion and FDTD methods were used for the majority of calculations in this thesis.

Eigenmode decomposition techniques, also known as "frequency-domain methods," express possible solutions of Maxwell's equations in terms of a set of time-harmonic modes at definite frequencies. In *plane-wave expansion*, the electromagnetic field at a given frequency is expanded in terms of a plane-wave basis with finite cutoff, yielding a finite, generalized eigenproblem. Direct diagonalization or more efficient iterative methods can then be used to solve for the desired eigenmodes of the

system [98]. Frequency-domain methods are particularly useful for the calculation of photonic-crystal band structures and eigenmodes. Although the use of plane waves restricts the boundary conditions to be periodic, defect modes of photonic crystals can also be calculated by using a "supercell," a computational cell large enough that the localized field at the defect decays nearly to zero at the cell boundary.

The *finite-difference time-domain* (FDTD) method is a general numerical method for the solution of electromagnetic problems [99, 100]. Maxwell's equations are written in approximate form by discretizing all spatial- and time- derivatives, yielding update equations in time for the values of the electric and magnetic fields on a spatial grid. For photonic crystal applications, the FDTD method is particularly useful for calculating transmission through structures, estimating cavity Q-factors, and other problems in which it is useful to visualize time-varying fields, such as the simulation of propagating pulses. FDTD may also be used to calculate eigenfrequencies/band structures by exciting the structure with a wide-band current source and Fourier transforming the fields in time after source turn-off. FDTD is adaptable to problems including lossy or anisotropic dielectrics, metals, nonlinear materials [101], and frequency-dependent dielectric functions [99, Chap. 8], [102]. A variety of boundary conditions can be implemented, such as periodic boundary conditions (e.g. for band structure calculations) and perfectly-matched-layers (PML) [103–105]. PML is useful for transmission problems, as it eliminates spurious reflections from the computational cell boundaries by adding adjacent impedance-matched conductive layers.

Transfer-matrix methods solve for the electromagnetic fields at fixed frequency. Structures are first divided into slices for which the refractive index profile does not change in the propagation direction [106 111]. The eigenmodes of each slice are obtained by analytical or numerical methods, and the modal expansion coefficients are found by matching boundary conditions at each interface. (In the simplest case of multilayer films [112, Chap. 5], for example, the eigenmodes are two oppositely-traveling plane waves.) The transfer matrix relates fields at either end of the computational cell, yielding transmission and reflection. Real and imaginary wavevectors can be obtained from the eigenvalues of the transfer matrix. This class of methods is con-

venient for problems with frequency dependent dielectric functions and for dielectric functions that are piecewise constant in the propagation direction.

The *multiple scattering method* [113–115] also finds solutions to Maxwell's equations at fixed frequency. The entire structure is regarded as a collection of individual dielectric or metal scatterers, e.g. rods. For each rod, an individual scattering matrix is found to relate the local incoming and scattered fields in a truncated multipole basis. The local incoming field is then alternatively written as a sum of incident fields and unknown scattering contributions from all other rods. The resulting linear matrix equation is solved self-consistently to obtain the field as a function of position throughout the structure. Transmission, power flux, cavity Q's, and resonance modes of the structure (via poles of the scattering matrix) may also be found. The multiple scattering method is most advantageous for structures composed of a number of identical scattering elements, as the individual scattering matrix must only be calculated once. Once calculated, it may also be reused for problems with different incident fields. Closely related to the multiple scattering method is the *source-current technique* [116].

1.5 Overview of thesis

From the discussion of photonic-crystal fabrication methods in Section 1.3, it is apparent that the discovery and characterization of new 3D structures can have a significant impact on both the ease of experimental realization of photonic band gap effects and the practical feasibility of proposed applications. Chapter 2 contributes to this effort by providing a bridge between a large body of theoretical work done in idealized, 2D systems and the real, three-dimensional world. We identify point-defect modes of 3D crystals that resemble those of pure, 2D crystals, allowing for the straightforward adaptation of 2D optical functionalities in realistic systems.

The variety of proposed applications for photonic crystals points to the wide range of unique physical phenomena arising from bulk, dispersive, and defect-mode properties of photonic crystals. In Chapter 3, we identify an interesting physical property

of point-defect modes introduced in Chapter 2, their resemblance to fluctuating magnetic dipoles. This resemblance is quantified by analysis of emission properties of the defect modes. The results suggest possibilities for the design of a new class of "synthetic" magnetic materials at optical frequencies. Chapters 4 and 5 identify two previously unstudied effects of the extremely low group velocities achievable in photonic crystals: slow-light enhancement of both radiation pressure and tunable time delays. Results on slow-light enhancement of radiation pressure suggest new methods for optical manipulation and positioning of objects on the microscale, with possible application to the search for quantum effects in micromechanical systems. Results on enhanced time-delay sensitivities have direct application to integrated device design, with applications for optical signal processing and logic.

Lastly, Chapter 6 addresses the both theoretically and practically important problem of disorder-induced scattering in photonic-crystal waveguides. We provide the first explicit, analytical treatment of disorder-induced scattering in strongly periodic, high-index-contrast media. The results not only provide physical insight into the effect of a photonic band gap on scattering, but also suggest a new mechanism for the design of low-loss waveguides. In addition, the theoretical formulation provides a basis for the development of new, efficient, semianalytical methods for the accurate numerical simulation of realistic disorder in 3D photonic-crystal waveguides, which has been prohibitively difficult using previous techniques.

In the remainder of this Chapter, we introduce the motivations, results, and implications of this work in greater detail, providing an overview of the thesis.

2D-like defect modes in a 3D photonic crystal

A great deal of previous theoretical work on the design of useful devices in photonic crystals has been carried out in idealized, purely 2D systems. For example, work in 2D has demonstrated 100% transmission through 90-degree bends in photonic-crystal waveguides [33], channel-drop tunneling through localized states [29,30], elimination of cross-talk in waveguides [35], and high transmission in wide-angle splitters [34]. 2D problems not only require less computational time than 3D problems; they also tend

to be much easier to visualize. In 2D, all electromagnetic modes can be characterized as either TE-polarized (magnetic field perpendicular to the plane) or TM-polarized (electric field perpendicular to the plane), reducing the general, full-vectorial problem to a scalar one. In a 3D crystal the situation is more complex, as the modes can no longer be divided into TM and TE polarizations [5, Chap. 5].

All of the 2D designs mentioned above rely on symmetry properties of the photonic crystal in combination with the existence of a complete band gap. As a result, they can in principle be realized in the real (3D) world as well— given a three-dimensional crystal with an appropriate geometry. In other words, what is needed to implement the 2D designs is a 3D crystal which closely resembles 2D photonic crystals in terms of symmetry and mode polarizations.

Photonic-crystal slab structures [9,10,37,61,62,117–122], discussed earlier in this chapter, are two-dimensionally periodic structures of finite height that approximate the behavior of an ideal 2D crystal. However, due to the lack of a complete gap, radiation losses are introduced by any device element that breaks periodic translational symmetry, such as waveguide bends [65, 123] and optical cavities [63, 64, 124, 125]. Only *three-dimensional* crystals with complete gaps can eliminate intrinsic radiation loss.

However, none of the 3D photonic crystal structures known prior to 2000 had both a large, complete gap and cross sections resembling common 2D crystal geometries (arrays of air holes in dielectric, or dielectric rods in air). "Nonplanar" structures, including diamond [3], A7 [126], inverse opal [127–129], and Yablonovite [4], all have fairly complicated cross sections that vary continuously with height, complicating the visualization and design of defect modes. Although several "planar" (or layer-by-layer) structures were known, they lacked in-plane symmetry. For example, because the woodpile structure [67,130] consists of layers composed of parallel "logs," making a symmetric waveguide bend requires jumping up or down one layer in the structure [69,131]. Similar arguments apply to the structures proposed in [132] and [133]; the lack of in-plane symmetries prohibit identical waveguides along different directions.

In 2000, Johnson *et al* proposed a 3D-periodic, planar structure with a large,

complete band gap that had cross sections resembling 2D photonic crystals [134]. In Chapter 2, we establish that the defect modes of this structure strongly resemble those of the corresponding 2D photonic crystals in terms of the dispersion relations, field profiles, and polarizations. By working alternately within "hole" and "rod" layers of the 3D crystal, modes with TE-like and TM-like polarizations can be designed, similar to the TE and TM modes of 2D photonic crystals of holes and rods. In particular, it is shown that calculated linear- and point-defect modes of the 3D crystal have nearly identical mode profiles to 2D crystals on the midplane of the defect. This resemblance is quantified by numerical calculation of appropriately defined overlap integrals.

Our results were the first demonstration of 2D-like modal patterns in a full, 3D photonic crystal. As a result, a number of 2D structures can now be straightforwardly implemented in realistic, 3D systems without intrinsic loss. Already Ref. [135], for example, has theoretically demonstrated high, polarization-independent transmission around sharp bends in the 3D crystal. Moreover, the very recent fabrication of the bulk crystal with designed point-defect modes in the near infrared by Qi *et al* [70] marks exciting progress towards the experimental realization of such structures.

The design of 2D-like defect modes in 3D structures has been extended by Roundy *et al* in Ref. [136], which demonstrated a planar, 3D structure with an omnidirectional band gap and square (rather than triangular) symmetry within each layer. This structure allows, for example, the design of identical waveguides at 90 degrees (rather than at 60 and 120 degrees). Chutinan *et al* [137] have further suggested the use of hybrid structures to achieve 2D-in-3D properties: a photonic crystal slab is capped above and below by a 3D photonic crystal with a complete gap. Because the geometry of the 3D crystal may be quite different from the slab layer, this approach could offer advantages for fabrication, e.g. using combined lithographic and layer-deposition (GLAD) processes.

Using defect modes to construct metamaterials

Chapter 3 examines in detail an unusual property of a point defect mode introduced in Chapter 2: its magnetic dipole-like character. Focusing on a defect made by en-

larging a single hole of the 3D crystal, it is seen that the electromagnetic field pattern resembles that of a magnetic dipole in polarization and profile. Unlike the static magnetic dipoles found in bar magnets, however, this "synthetic" dipole oscillates with the harmonic time-dependence of the field, suggesting comparison to a magnetic dipole *source*.

A quantitative assessment of the magnetic character of the mode is obtained by decomposing the radiated field into a series of multipole radiation terms, both magnetic and electric. The dominant terms are found to be low-order magnetic moments: l=1 (dipole), 3 and 5 terms. Overall, nearly all (up to 98%) of the radiated power has magnetic (rather than electric) character. This property stems from the 2D-like polarization of the defect mode, as characterized in Chapter 2. In two dimensions, the emission from a TE mode would be purely magnetic. In the 3D crystal, the approximate TE-like character of the mode leads to predominantly magnetic multipole emission.

Intuitively, magnetic multipole emission arises from the displacement currents in the crystal, which circulate the hole defect to create a current loop. A simple wire current loop emits magnetic dipole radiation; due to its more complicated geometry, the photonic crystal emits a combination of magnetic multipole terms. Unlike in a wire loop, however, the displacement currents can oscillate at optical frequencies, at which AC currents in metals would be swamped by dissipation.

An optical-frequency "current loop" could be useful for the design of metamaterials [138–140], composite materials designed to have unique emergent properties of interest such as negative refraction [19,20,24,141–147]. Negative refraction "reverses" Snell's law such that light beams are bent backwards by the interface, allowing for an entirely new class of optical devices [138,148] and the possibility of subwavelength imaging [23,24,149,150]. It has been shown that for metallic [138], dielectric [140], and polaritonic [151] materials, the excitation of localized modes resembling displacement-current loops leads to an effective negative magnetic permeability (μ_{eff}) in arrays of *nonmagnetic* elements. The results of Chapter 3 thus suggest that magnetic point defects in photonic crystals might provide building blocks for the design of future

optical-frequency metamaterials.

Slow light

The next section of the thesis (Chapters 4 and 5) concerns slow-light phenomena in photonic crystals. Low group velocities are a consequence of the complex dispersion characteristics of photonic crystals, which result from coherent scattering in the periodic medium. In a multilayer film, for example, the group velocity goes to zero for frequencies near the band edge, corresponding to wave vectors near the edge of the Brillouin zone. Zero group velocities are also found at zero wave vector for second and higher bands. These features follow from the analyticity of the dispersion relation, and occur quite generally in 2D- and 3D-periodic bulk structures and linear-defect waveguides [5]. Coupled-cavity waveguides (CCW's) [152] further exhibit low (nonzero) group velocities at a point of zero dispersion in the center of the Brillouin zone.

Experimentally, extremely slow group velocities have been observed in photonic crystals. Group velocities of less than $0.01c$ [153] have been demonstrated in the microwave range. At optical frequencies, propagation speeds 5–90 times slower than that in air have been measured for line defects in photonic-crystal slabs [154]. In CCW's, group velocity reduction by a factor of four has been observed, as compared to a standard reference waveguide [155].

Low group velocities are known to enhance a variety of optical phenomena including nonlinearities, phase-shift sensitivity [156], lasing [157, 158], and band-edge absorption in metallic photonic crystals [159]. Here we propose that slow light can magnify radiation pressure and time-delay sensitivity, leading on the one hand to the prediction of new physical phenomena and on the other to useful device designs.

Slow-light enhancement of radiation pressure

Radiation pressure refers to the pressure exerted on a mechanical object by light impinging on its surface. Radiation pressure effects in Fabry-Perot cavities, optical

cavities formed by parallel mirrors [160, Section 9.1], have been extensively studied. Because the field intensity inside the cavity can be much higher than that of the input field, the radiation pressure is relatively large. A number of interesting optical effects result, from classical optical bistability [161] to proposed quantum effects such as ponderomotive squeezing [162], generation of nonclassical states of light [163], and the entanglement of macroscopic objects through optomechanical cooling [164].

Using high-index-contrast materials such as Si/SiO_2, it is possible to shrink the cavity size to dimensions comparable to the wavelength of light, on the order of a micron [18]. The tight modal confinement and small mass of such tiny structures suggest the exploration of radiation pressure as a means of moving, manipulating, and positioning objects on the microscale, for example within integrated optical devices.

In Chapter 4, we consider a generalization of the Fabry-Perot cavity well-suited to implementation on the microscale. We consider radiation pressure on the walls of a waveguide formed by planar, omnidirectionally-reflecting mirrors [18] separated by an air gap. As the width of the air gap is varied, the propagating modes localized in the air gap are changed. In particular, the modal group velocity can be reduced to zero by bringing the mirrors closer together. For constant input power, the electromagnetic field energy builds up, exerting a radiation pressure force on the mirrors and pushing them apart. In the absence of losses, the force diverges to infinity. Our structure provides an alternative system to study the variety of classical and quantum effects associated with Fabry-Perot cavities. Slow-light enhancement of quantum effects in particular could prove useful in the ongoing search for quantum effects in micromechanical systems [165, 166].

Slow-light enhancement of tunable time delays

We turn next to slow-light enhancement of tunable time delays, analyzed in Chapter 5. Introducing a delay on an optical signal is useful for a number of applications, including optical signal processing and optical logic; a standard method is the use of fiber-optic delay lines [167]. The use of optical resonances in atomic gases [168–172] has received much attention due to interest in the fundamental physics, but is

currently far from practical device application. The ability to engineer the dispersion of photonic crystals suggests another route to optical delays, one that could result in compact, "on-chip" time-delay devices.

Previous work has examined devices based either on switched waveguides or all-pass filters [173, 174], which allow only discrete delay increments. Devices based on coupled-cavity waveguides [152] in photonic crystals [155,175 177] allow continuously tunable time delays, but are intrinsically lossy unless implemented in a 3D photonic crystal. In Chapter 5, we propose a continuously tunable, integrated-optical time delay scheme that can be implemented in a planar geometry without intrinsic losses, using slow light at the photonic band edge.

Changing the refractive index of a waveguide, for example by thermal tuning, modifies the group velocity, an effect that can be used for tunable time delays. We show that for frequencies near the band edge of a photonic-crystal waveguide, low group velocities lead to enhancement of time-delay *sensitivity*: the change in delay for a given change in index. An increased sensitivity shrinks the required device length, resulting in lower operating powers. While signal dispersion also increases near the band edge, we show that strong gratings (corresponding to large band gaps) optimize the device length for a given dispersion. By direct numerical simulations of a realistic structure, we show that appropriate figures of merit for this class of devices are well approximated by a simple, quadratic-band model. The results should thus greatly simplify design optimization.

Disorder in photonic-crystal waveguides

Disorder is an inevitable feature of real photonic crystals. In lithographic methods, for example, roughness on vertical surfaces results from the etching process. Inaccuracies in position, layer thickness, and so on provide additional disorder. The effect on the properties of bulk photonic crystals is well known [178–180], and fortunately not severe; disorder results in a slight reduction in the size of the band gap. Less well understood is the effect of disorder on propagation through photonic-crystal waveguides. The problem is of both theoretical and practical importance, for disorder-

induced losses ultimately limit the achievement of slow-light propagation speeds, the achievable integration density in optical circuits, and other applications of photonic crystals.

Experimentally, photonic-crystal waveguides appear to suffer relatively high losses. The lowest reported loss measurements for single-line-defect, photonic-crystal slab waveguides, for example, is in the range of 1–3dB/mm for optical wavelengths [181 183]. Heterostructure-type slabs, which operate above the light line and are thus intrinsically lossy even in the absence of disorder [184–188], have loss values several orders of magnitude higher. (Measurements of disorder-limited losses for waveguides in 3D-periodic crystals have not yet been reported.) For conventional, index-guided waveguides, much lower losses of 0.8dB/mm have been achieved for single-mode, silicon-on-insulator strip waveguides [189]. Will improvements in fabrication methods allow photonic-crystal waveguides to catch up, or are low losses somehow fundamentally unachievable?

Attempts to answer this question have been frustrated by the lack of a general understanding of the effect of disorder on reflection and transmission in photonic-crystal waveguides. It is not even clear how to compare photonic-crystal waveguides to standard, index-guided ones; even if we can imagine that both have the "same amount" of disorder, important characteristics such as mode profile, polarization, and effective index can differ greatly, obscuring meaningful comparison.

Previous work on the effect of disorder on photonic-crystal waveguides has provided only limited study of specific cases, including theoretical analysis of coupled-cavity waveguides [190], and numerical study of photonic-crystal slabs [191] and pure 2D crystals [192,193]. Although a variety of techniques have been developed to model roughness losses in conventional index-guide waveguides [194–197], none is valid in the limit of high-index-contrast and strong periodicity applicable to photonic crystals.

To fill this gap, Chapter 6 develops a general, analytical theory for modeling the effects of disorder in strongly-periodic, high-index-contrast waveguides, with or without a complete band gap. In brief, by working with a basis of Bloch modes of the unperturbed crystal and recasting Maxwell's equations in operator form, it is possible

to derive a set of differential equations for the mode coefficients as a function of length along the propagation direction. The result is a modification of standard coupled-mode theory [194] valid for photonic crystals. We obtain an explicit expression for the reflection coefficient as a function of the relevant parameters, allowing "apples-to-apples" comparison of photonic-crystal and index-guided waveguides and insight into the physical effect of a band gap on disorder-induced loss.

In an ordinary, index-guided waveguide, light traveling along the waveguide scatters from a disorder site and is directed into radiation and reflection losses (as well as in the forward direction, changing the phase of propagation). In a photonic-crystal waveguide, scattered light cannot escape into radiation modes, for the existence of such modes is prohibited by the band gap. The theory shows that the effect of the band gap is to suppress scattering from disorder: the total amount of radiated power is in fact lower for a photonic-crystal waveguide than in the comparable, index-guided case. All other things being equal, the amount of power reflected from disorder is the same in the two cases, while the total transmission is higher for the photonic-crystal waveguide.

Practically, our results offer a new mechanism for the design of low-loss waveguides. By surrounding an index-guided waveguide with a photonic crystal with either full or partial band gap, radiation loss can be reduced without increasing reflections, decreasing the total loss. The coupled-mode theory should also allow the development of improved, semi-analytical methods for the modeling of realistic amounts of disorder, which are actually too *small* to be treated by "brute-force" methods such as FDTD, for which required computational resources drastically increase with decreasing feature sizes. Such methods should shed light on the design of optimal, low-loss waveguides for applications such as slow-light devices and integrated optical circuits.

Parts of this thesis have previously been published in article format. See Refs. [198-202].

Chapter 2

2D-like Defect Modes in a 3D Photonic Crystal

This chapter has previously been published as Ref. [198].

Introduction

Photonic crystals, periodic dielectric structures that can prohibit light propagation in a range of wavelengths [1, 2, 5], have been the subject of intense research in the last decade [203]. One particularly interesting aspect of these systems is the possibility of creating crystal defects that confine light in localized modes. Advances in understanding of these defect modes have stimulated the design of photonic-crystal waveguides, resonant cavities, filters, and other practical optical components, leading towards the possibility of integrated optical circuits [36].

Much of the theoretical investigation of photonic crystals has been carried out in two-dimensional systems, due to the inherent simplicity of calculation, visualization, and understanding in 2D. Many interesting and potentially useful physical phenomena have been discovered in 2D, including high transmission through sharp bends in photonic-crystal waveguides [33], channel-drop tunneling through localized states [29, 30], high localization in microcavities [204], elimination of cross-talk in

waveguides [35], and high transmission in wide-angle splitters [34]. Fortunately these phenomena are based on general principles that are not restricted to two dimensions, for experimental realization requires the use of three-dimensional structures.

In order to achieve three-dimensional confinement, two general types of three-dimensional photonic-crystal systems have been proposed. One type is photonic-crystal slabs, two-dimensionally periodic structures of finite height. In these structures, light is confined by a combination of an in-plane photonic band gap and out-of-plane index guiding [9, 27]. While it is possible to create localized linear- [10, 62, 65, 120–123] and point- [125, 205, 206] defect modes in slab systems, the lack of a complete band gap is an inherent limitation that results in radiation losses in all cases where the translational symmetry of the crystal is destroyed, for example in waveguide bends [10]. A second type of system, three-dimensionally periodic photonic crystals with a complete band gap, has no such theoretical limitation. The complex geometry of most three-dimensional crystals, however, makes the study and understanding of defects in these systems more difficult; the modes typically cannot be approximated by their simpler, well understood, two-dimensional analogues.

Recently, a structure and method of fabrication were proposed for a new 3D photonic crystal with a large, complete band gap [134]. This structure is composed of alternating layers of triangular lattices of air rods in dielectric and dielectric rods in air; cross sections thus correspond to 2D photonic-crystal geometries. In this chapter, we discuss how this feature, in combination with the large band gap, greatly simplifies the understanding of defect modes. We show that line- and point-defect modes of the full, 3D photonic crystal have a close correspondence in band structure, field profile, and polarization to the modes of the respective 2D photonic-crystal geometries.

Moreover, the 3D photonic crystal structure that we study here allows the combination of line- and point-defect modes in a similar manner to that which is possible in 2D photonic crystals [207, 208]. Thus, these results promise that two-dimensional analyses and phenomena, even in complex integrated optical devices, may be directly applicable to a three-dimensional crystal with an omnidirectional band gap, with only slight changes in parameters and the resulting mode characters.

Crystal structure

The 3D photonic-crystal structure of interest is shown in Fig. 2-1(a). The arrows indicate the two different types of layer which make up the structure. Fig. 2-1(b) shows horizontal cross sections through these layers. Layer I has the form of a triangular lattice of dielectric rods in air; we refer to it as a *rod layer*. Layer II has the form of a triangular lattice of air holes in dielectric; we refer to it as a *hole layer*. (The shape of the rods is a result of a proposed fabrication method, and is not essential for the properties of the crystal [134].) The underlying lattice of the photonic crystal is face-centered cubic (fcc). Centers of the holes are placed at fcc lattice sites, and hole and rod layers are stacked along the 111 direction.

It was shown in Ref. [134] that this structure has a large, complete band gap of around 20% of the midgap frequency for Si/air structures with suitable choices for the structural parameters. Lengths may be specified in terms of $\bar{a}$, the nearest neighbor spacing within either a hole or rod layer. The nearest neighbor spacing is related to the fcc lattice constant, a, by $\bar{a} = a/\sqrt{2}$. For the calculations presented here, the hole radius is taken to be $r_{\mathrm{h}} = 0.414\bar{a}$. The radius of a cylindrical rod with the same area as a rod in the structure is $r_{\mathrm{r}} = 0.175\bar{a}$. The thickness of a hole layer is $0.318\bar{a}$, and the thickness of a rod layer is $0.500\bar{a}$. These values correspond to an optimal parameter set which maximizes the gap size [134], where the dielectric constant of the high-index material is taken to be $\epsilon = 12$.

It is particularly significant for the present work that cross-sections of hole and rod layers have the same geometry as the two widely-studied, canonical 2D photonic-crystal structures: an array of air holes in dielectric, which supports a TE gap and TE defect modes, and an array of dielectric cylinders in air, which supports a TM gap and TM defect modes. We will show here that this geometrical feature, in combination with the presence of a 3D photonic band gap, allows us to construct 2D-like defect modes in the 3D structure.

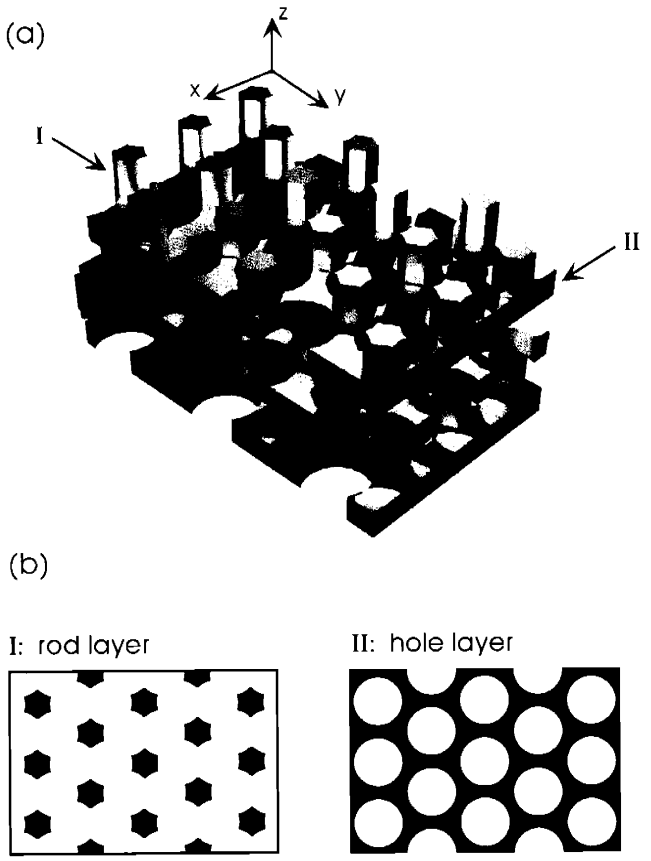

Figure 2-1: (a) Computer rendering of the 3D photonic crystal structure studied in this work. The structure consists of two alternating types of layers, indicated by the arrows. We refer to the type of layer labelled I as a *rod layer*, and that labelled II as a *hole layer*. (b) Cross sections of rod and hole layers. These cross sections have the same geometry as the two types of widely-studied 2D photonic crystals: arrays of dielectric rods in air and arrays of air holes in dielectric.

Computational methods

The computational methods used to calculate photonic band structures and electromagnetic field modes employ preconditioned conjugate-gradient minimization of the Rayleigh quotient in a plane-wave basis and are described in detail elsewhere [98,209]. A supercell method was used for defect calculations: the defect was surrounded by several periods of the unperturbed crystal within a "supercell," and periodic boundary conditions were applied. The supercell dimensions were chosen to be large enough for adjacent waveguides/cavities to have minimal effect on mode frequencies and fields. Projected bands corresponding to bulk modes were computed using a defect-free supercell.

Linear-defect modes

It is well known that linear defects in photonic crystals can act as waveguides [5]. These defects can be created by either adding or removing high-index material, altering the effective index of the waveguide in comparison to its surroundings. However, it is the reduced-index case that is unique to photonic crystals. Traditional dielectric waveguides, which operate on the principle of index-guiding, necessarily confine light to regions of higher index. In contrast, photonic-crystal waveguides can guide light in regions of lower index, even primarily in air. We focus here on reduced-index linear-defect modes.

We first consider the case where a *single hole layer* of the 3D photonic crystal is modified to create a linear defect. As we will show, this has the effect of introducing a TE-like mode into the hole layer. To create a reduced-index linear defect, we increased the radii of a line of nearest-neighbor holes from $r_h = 0.414\bar{a}$ to $r'_h = 0.500\bar{a}$. At this value, the holes just touch. A horizontal cross section of the structure, through the center of the defect, is shown in the inset to Fig. 2-2(a). Notice that the geometry of this cross section is identical to that of a 2D line-defect in a 2D structure of air holes in dielectric, as shown in the inset to Fig. 2-2(b).

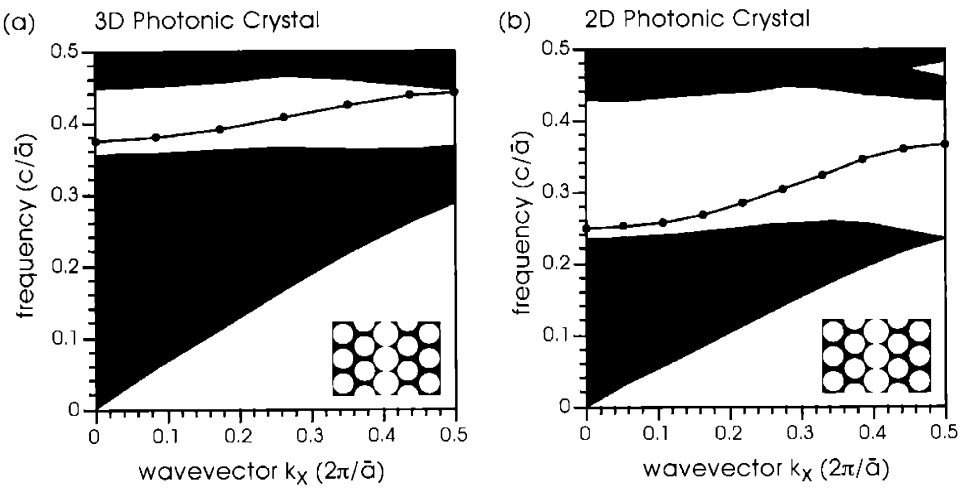

Figure 2-2: (a) Projected band structure for the 3D crystal with a linear defect created by altering a single hole layer. Shown in the inset is a horizontal cross section through the mid-plane of the defect (parallel to the x-y plane). The radius of the defect holes is $r_h' = 0.500\bar{a}$, as compared to $r_h = 0.414\bar{a}$ in the bulk, where $\bar{a}$ is the in-plane distance between nearest-neighbor holes. (b) Projected band structure for the TE modes of the 2D crystal with identical geometry to the cross section of the 3D crystal shown in Fig. 2-2(a).

The projected band structure, or dispersion diagram, for the 3D line-defect structure is shown in Fig. 2-2(a) and compared with that for the 2D line-defect structure in Fig. 2-2(b). Shaded regions indicate extended states in the perfect crystal. The frequencies of these states are plotted as a function of k_x, the component of the wavevector along the the direction of the linear defect, which takes on values between 0 and $\pi/\bar{a}$. For the 3D structure, *all* modes are projected onto the band diagram and the structure has a large, complete band gap. For the 2D structure, only TE modes are shown, since it is for the TE polarization that a large gap is present. Moreover, only modes with wavevectors corresponding to in-plane propagation are considered in calculating the 2D dispersion relation. In both Figs. 2-2(a) and 2-2(b), the line within the gap region shows the dispersion relation of the single-mode defect band. The states within this band are confined to the region of the defect. For the 3D case, the band extends from a lower frequency of $0.37\,c/\bar{a}$ to an upper frequency of $0.44\,c/\bar{a}$. In the 2D case, the band extends from $0.25\,c/\bar{a}$ to $0.37\,c/\bar{a}$. The similarities between the 3D and 2D projected band structures are notable. In both cases, a *single* defect

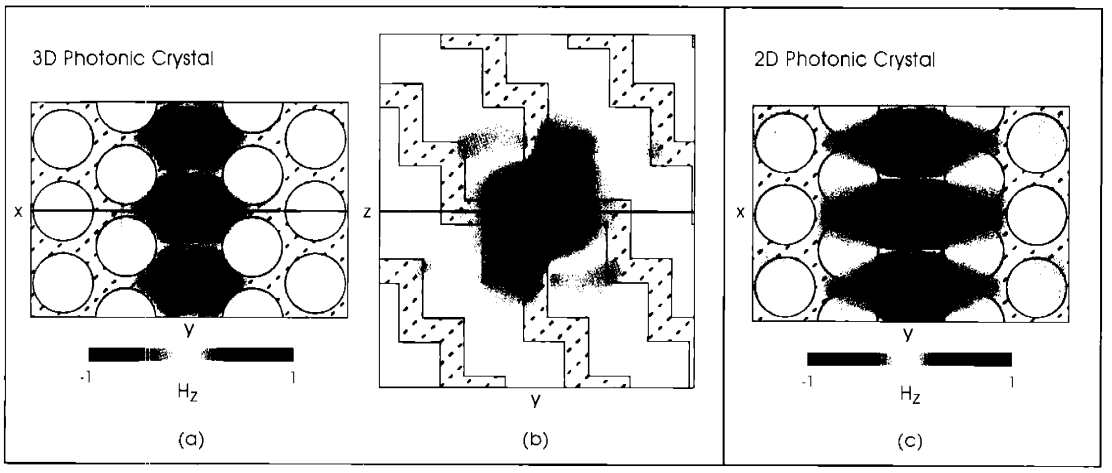

Figure 2-3: Mode profiles for the increased-hole linear-defect states from Fig. 2-2 at the Brillouin zone edge. Overlaid cross hatches indicate regions of high dielectric material. (a–b) The field for the 3D linear-defect structure corresponding to Fig. 2-2(a). H_z is plotted for horizontal and vertical cross sections of the 3D crystal. The cross sections intersect along the green lines on the figures. (c) H_z for the 2D linear-defect structure shown in the inset to Fig. 2-2(b).

band extends across the entire Brillouin zone, inside the band gap. The shapes of the defect bands are also similar, since both bands must exhibit vanishing group velocity at both the center and edge of the Brillouin zone.

In addition to the resemblance between the projected band structures, there is a strong, quantifiable similarity between the defect modes in the 3D and 2D crystals. Figs. 2-3(a) and 2-3(b) show the field profiles for the 3D defect state at the edge of the Brillouin zone for horizontal and vertical cross sections through the center of the linear defect. (The horizontal cross section is parallel to the x-y plane, and the vertical is cross section is parallel to the y-z plane.) In both cases, the z-component of the H-field is shown. The green lines on the figures indicate the intersection of these cross sections. The 3D defect mode is, clearly, strongly localized near the defect in all three dimensions. Fig. 2-3(c) shows the magnetic field for the 2D defect state at the same k point.

Comparing the horizontal cross section of the 3D defect mode to the 2D defect mode, we see that the two are nearly identical in polarization and profile; we quantify this observation in the following. In the 2D crystal, the continuous translational

invariance of the crystal in the z direction allows a separation of the electromagnetic-field modes into TE and TM polarizations. The defect mode in Fig. 2-3(c) is purely TE-polarized; the H-field is entirely in the z direction. In the 3D crystal, the horizontal plane through the center of the defect is not a mirror plane of the 3D structure. Thus symmetry considerations do not require the defect mode to be purely TE or TM-polarized there. However, we observe that the 3D mode is nearly TE-polarized in this plane;

$$R_H \equiv \frac{\int \mathrm{d}^2 r \, |H_z^{3\mathrm{D}}(\omega; \mathbf{r})|^2}{\sum_j \int \mathrm{d}^2 r \, |H_j^{3\mathrm{D}}(\omega; \mathbf{r})|^2} \approx 0.98, \tag{2.1}$$

where the integral is taken over the horizontal plane. The similarity of the mode profiles may also be quantified, by computing an overlap between the horizontal cross section of the 3D state and the 2D state. For the states shown in Fig. 2-3,

$$O_H \equiv \left| \frac{\int \mathrm{d}^2 r \, \vec{H}^{3\mathrm{D}}(\omega, \mathbf{r})^* \cdot \vec{H}^{2\mathrm{D}}(\omega, \mathbf{r})}{\sqrt{\int \mathrm{d}^2 r \, |\vec{H}^{3\mathrm{D}}(\omega, \mathbf{r})|^2 \int \mathrm{d}^2 r \, |\vec{H}^{2\mathrm{D}}(\omega, \mathbf{r})|^2}} \right|^2 \approx 0.94. \tag{2.2}$$

The similarity between the mode profiles is a consequence of the localization of the 3D defect mode to a 2D-like environment, and relies on the presence of a large, complete band gap in a 3D structure with 2D-like cross sections.

Previous work has studied linear defect modes in photonic-crystal slabs [10], which can also have a strong resemblance to the defect modes of two-dimensional photonic crystals. However, it is important to stress that the projected band structures of photonic-crystal slabs and two-dimensional photonic crystals are very different. Fig. 2-4 shows the projected band structure for a slab with the same cross section as the 3D and 2D structures considered above. The thickness of the slab was taken to be $0.71\bar{a}$, which approximately optimizes the gap size [9]. The light-grey region indicates the light cone, a continuum of all possible frequencies of the bulk background, in this case air. The dark-grey regions indicate the even-symmetry bulk modes of the slab. The region of k space covered by neither the bulk modes nor the light cone is only a fraction of the Brillouin zone, sharply limiting the bandwidth of the guided mode. This is in sharp contrast to the projected band structures for the 3D and 2D photonic

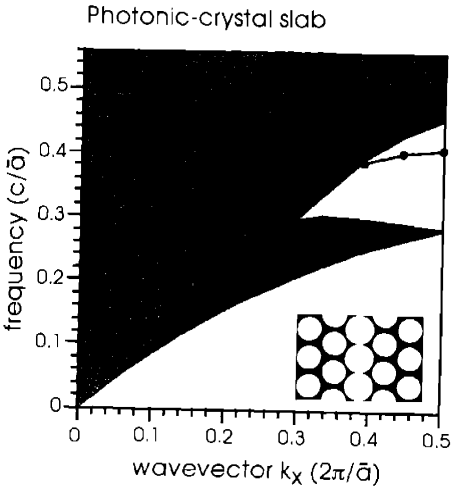

Figure 2-4: Projected band structure for a photonic-crystal slab, with a linear defect as in Fig. 2-2. A cross section of the slab is shown in the inset; the thickness of the slab is $0.71\bar{a}$. The light-grey region indicates the light cone; dark-grey regions indicate even-symmetry modes of the bulk structure.

crystals shown in Fig. 2-2, where the gap extends across the entire Brillouin zone.

We have shown that a TE-like defect mode can be introduced into the 3D photonic crystal by altering a hole layer. A TM-like defect mode can similarly be created by modifying a rod layer of the structure. This was done by replacing a row of nearest-neighbor rods with smaller, cylindrical rods of radius $r_r' = 0.071\bar{a}$. The projected band structure for the 3D photonic crystal is shown in Fig. 2-5(a), and a cross section through the linear defect is shown in the inset. Fig. 2-5(b) shows the projected band structure for the TM modes of the 2D photonic crystal with the corresponding geometry. Again the band structures are quite similar, with a single-mode defect band extending across the entire Brillouin zone.

Mode profiles for 3D and 2D defect states at the Brillouin zone edge are shown in Fig. 2-6. Figs. 2-6(a) and 2-6(b) show the z component of the E-field for the 3D defect mode. The 2D defect mode is shown in Fig. 2-6(c) and is TM-polarized (the E-field is entirely in the z-direction). The 3D defect mode is nearly TM polarized, with:

$$R_E \equiv \frac{\int \mathrm{d}^2 r \, |E_z(\omega;\mathbf{r})|^2}{\sum_j \int \mathrm{d}^2 r \, |E_j(\omega;\mathbf{r})|^2} \approx 0.99. \tag{2.3}$$

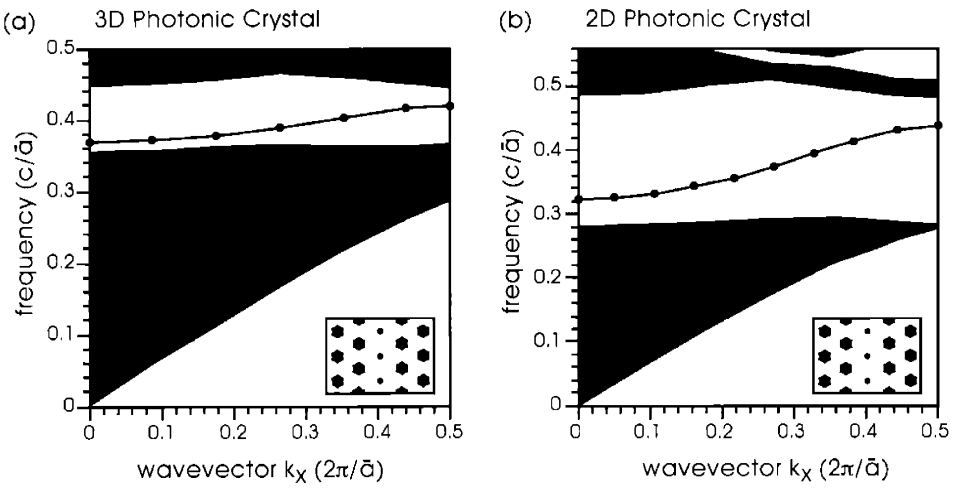

Figure 2-5: (a) Projected band structure for the 3D crystal with a linear defect created by altering a single rod layer. A row of nearest-neighbor rods has been replaced with cylindrical rods of radius $r_r' = 0.07\bar{a}$. Shown in the inset is a horizontal cross section through the mid-plane of the defect. (b) Projected band structure for the TM modes of the corresponding 2D photonic crystal.

The mode profiles are again very similar; in order to define a suitable overlap function, it is necessary to consider the orthonormality properties of the E-field. Suppose that $\vec{E}_1(\omega, \mathbf{r})$ and $\vec{E}_2(\omega, \mathbf{r})$ are the electric fields corresponding to two eigenmodes of a fixed 2D dielectric structure specified by $\epsilon(\mathbf{r})$. It follows from Maxwell's equations that although E_1 and E_2 are not orthonormal under the usual metric, it is true that:

$$\int \mathrm{d}^2 r\, \epsilon(\mathbf{r})\, \vec{E}_1(\omega, \mathbf{r})^* \cdot \vec{E}_2(\omega, \mathbf{r}) = 0 \tag{2.4}$$

It is thus sensible to compute an overlap of the 3D and 2D defect modes by

$$O_E \equiv \left| \frac{\int \mathrm{d}^2 r\, \epsilon(\mathbf{r})\, \vec{E}^{3\mathrm{D}}(\omega, \mathbf{r})^* \cdot \vec{E}^{2\mathrm{D}}(\omega, \mathbf{r})}{\sqrt{\int \mathrm{d}^2 r\, \epsilon(\mathbf{r})\, |\vec{E}^{3\mathrm{D}}(\omega, \mathbf{r})|^2 \int \mathrm{d}^2 r\, \epsilon(\mathbf{r})\, |\vec{E}^{2\mathrm{D}}(\omega, \mathbf{r})|^2}} \right|^2 ; \tag{2.5}$$

the value was found to be approximately 0.95.

A reduced-index linear defect can also be created by completely removing a line of rods. The resulting 3D and 2D band structures are shown in Fig. 2-7. The single-mode defect band in the 3D structure approaches the bulk states at the edge of the Brillouin

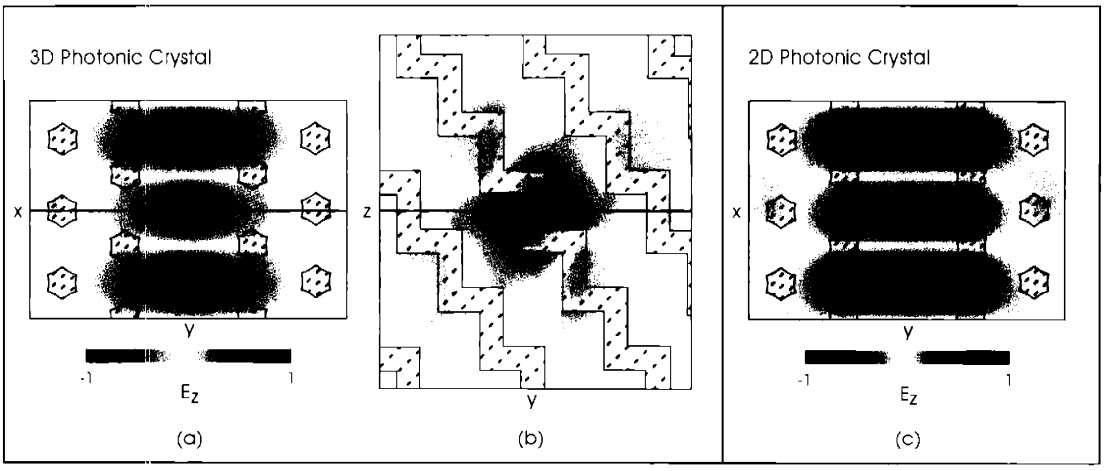

Figure 2-6: Mode profiles for the reduced-rod linear-defect states from Fig. 2-5 at the Brillouin zone edge. (a- b) The field for the 3D linear-defect structure corresponding to Fig. 2-5(a). E_z is plotted for horizontal and vertical cross sections of the 3D structure. (c) The field for the 2D structure shown in Fig. 2-5(b).

zone. The perpendicular E-field for $k_x = 0.265(2\pi/\bar{a})$ is shown in Fig. 2-8. As in the case of the reduced-radius rods, the 2D mode is completely TM-polarized and the 3D defect mode is nearly-TM polarized, with $R_E \approx 0.99$; the overlap $O_E \approx 0.98$. We note that the possibility of creating a guided mode by completely removing rods in a photonic-crystal *slab* is much more limited, since the necessity of vertical index-guiding does not allow truly guided modes that reside mainly in air [10]. This is illustrated in Fig. 2-9, which shows the projected band structure for a rod slab of thickness $2\bar{a}$. There is at most a very weakly confined defect mode very close to the edge of the band gap.

For all three cases of reduced-index waveguides in the 3D crystal, a single-mode, defect-state band is obtained within the complete, three-dimensional band gap. The waveguide modes are strongly localized within the altered layer, and both the projected band structures and mid-plane field profiles of the three-dimensional structures are very similar to those of the corresponding two-dimensional photonic crystals.

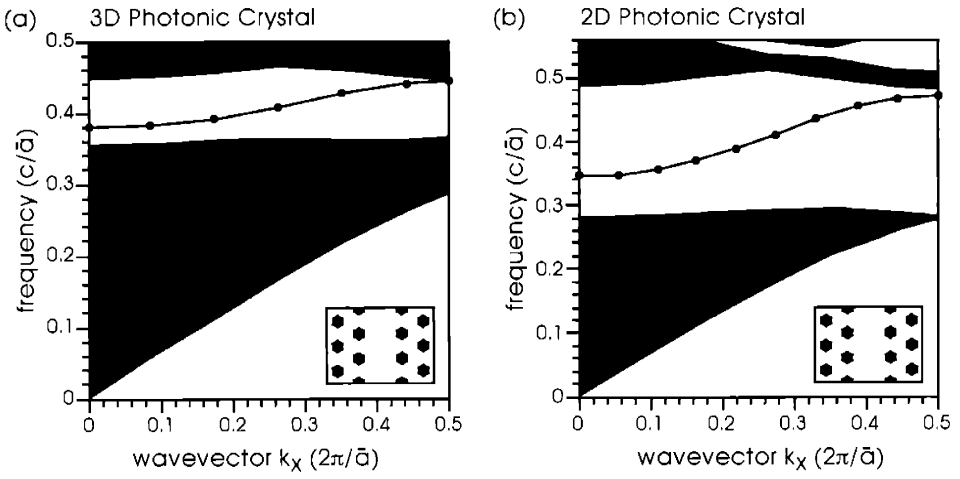

Figure 2-7: (a) Projected band structure for the 3D crystal with a linear defect created by removing a row of nearest-neighbor rods in a single rod layer. Shown in the inset is a cross section through the mid-plane of the defect. (b) Projected band structure for the TM modes of the corresponding 2D photonic crystal.

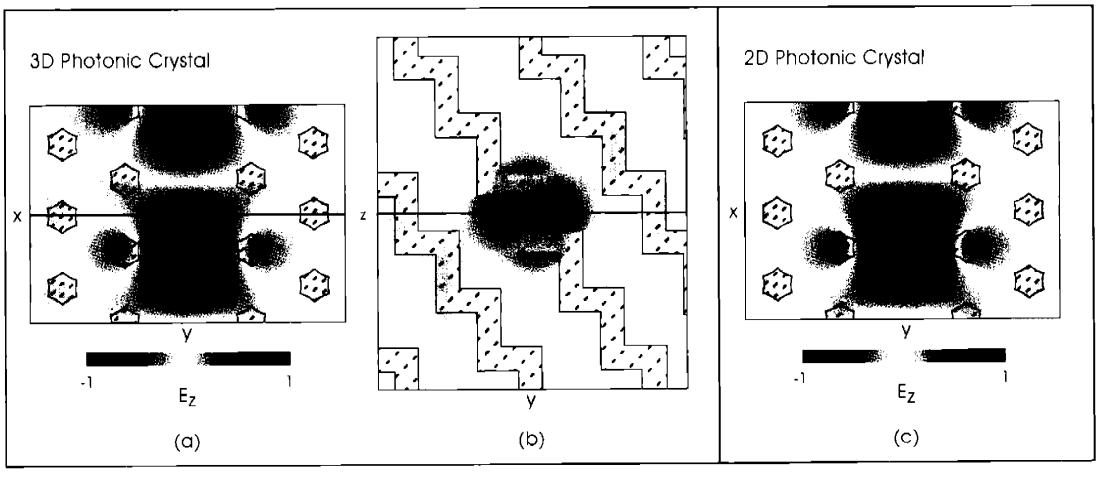

Figure 2-8: Mode profiles for the removed-rod linear-defect state at $k_x = 0.265\,(2\pi/\bar{a})$. (a-b) The field for the 3D linear-defect structure corresponding to Fig. 2-7(a). E_z is plotted for horizontal and vertical cross sections of the 3D structure. (c) The field for the 2D structure shown in Fig. 2-7(b).

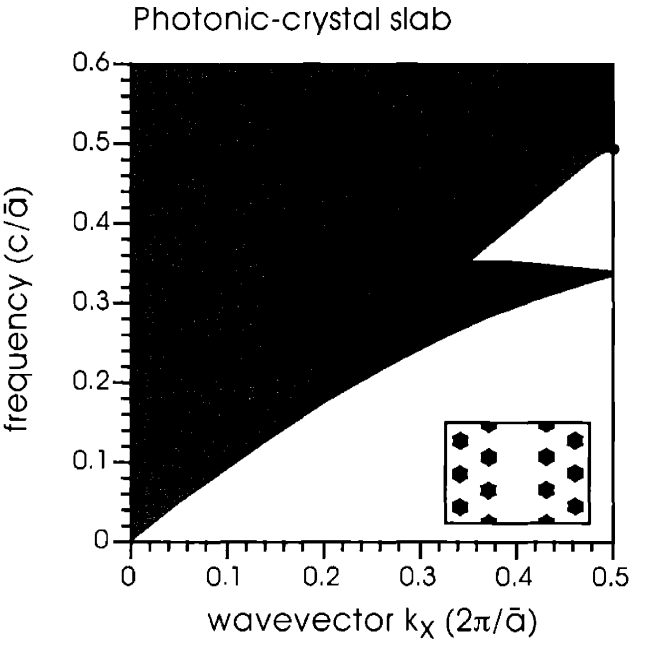

Figure 2-9: Projected band structure for a photonic-crystal slab, with a linear defect as in Fig. 2-8. A cross section of the slab is shown in the inset; the thickness of the slab is $2\bar{a}$. The light-grey region indicates the light cone; dark-grey regions indicate odd-symmetry modes of the bulk structure. In contrast to Fig. 2-4, there is at most a very weakly guided defect mode very near the edge of the band gap.

Point-defect modes

In the previous section, reduced-index *linear* defects were created in the 3D photonic crystal structure by altering either the hole or rod layer. Reduced-index *point* defects can be created in a similar manner. In Figs. 2-10, 2-11, and 2-12, we compare the point-defect modes in the 3D structure with those in the corresponding 2D structure. As for linear defects, the mode profile and polarization are very similar in the two structures.

Fig. 2-10 shows the perpendicular H-field for a hole defect, where the defect radius was taken to be $r'_h = 0.500\bar{a}$. The 3D mode has a frequency of $0.40c/\bar{a}$, which falls near the middle of the band gap, $(0.36 - 0.44)c/\bar{a}$. It is strongly localized in all three dimensions to the vicinity of the point defect. Moreover, it is nearly TE-polarized in the mid-plane, with $R_H \approx 0.98$. The 2D mode has a frequency of $0.28c/\bar{a}$, where the band gap runs over the frequency range $(0.26 - 0.43)c/\bar{a}$. The overlap of the 3D and 2D point-defect modes is $O_H \approx 0.92$.

Rod defects are shown in Figs. 2-11 and 2-12. In Fig. 2-11, a single rod is replaced with a reduced-radius rod with $r'_r = .071\bar{a}$. The 3D defect mode, which has a frequency of $0.40c/\bar{a}$, falls in the middle of the band gap $(0.36 - 0.44)c/\bar{a}$. The 2D defect mode a frequency of $0.37c/\bar{a}$, with a band gap range of $(0.30 - 0.48)c/\bar{a}$. In Fig. 2-12, a rod is completely removed. The defect mode frequencies are $0.41c/\bar{a}$ as compared to a gap range of $(0.36 - 0.44)c/\bar{a}$ for the 3D structure and $0.41c/\bar{a}$ as compared to a gap range of $(0.30 - 0.48)c/\bar{a}$ for the 2D structure. In both cases, the 3D defect modes are nearly TM polarized ($R_E \approx 0.99$) while the 2D defect modes are completely TM polarized. The overlaps between the 3D and corresponding 2D modes are again high, with $O_E \approx 0.97$ for both cases.

Conclusion

We have studied linear- and point-defect modes in a recently proposed 3D photonic crystal with a complete band gap. The cross sections of the 3D crystal have the

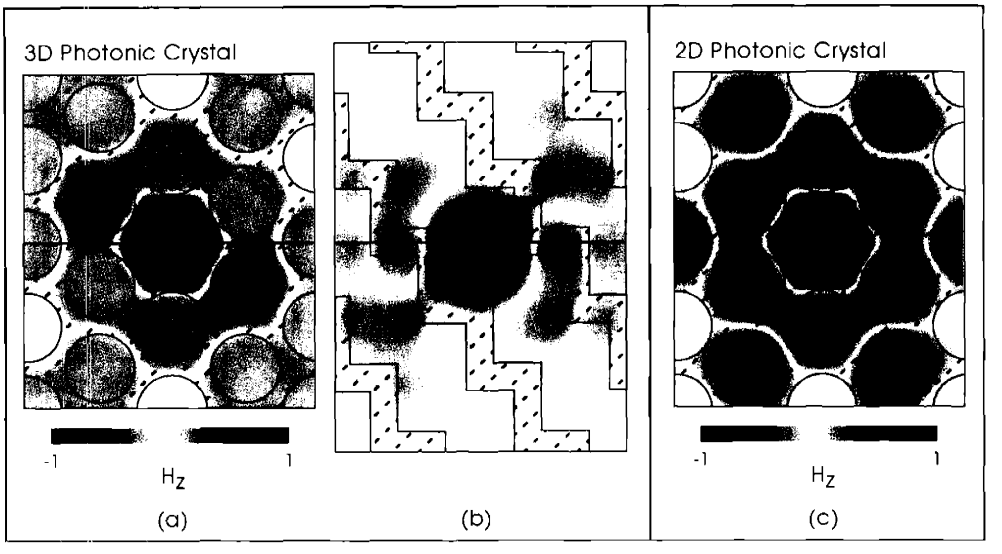

Figure 2-10: (a–b) Defect-mode profile for a point-defect in the 3D crystal created by increasing the radius of a hole in a single hole layer to $r'_h = 0.500\bar{a}$. H_z is plotted for horizontal and vertical cross sections of the 3D crystal. (c) Defect-mode profile for the corresponding 2D crystal.

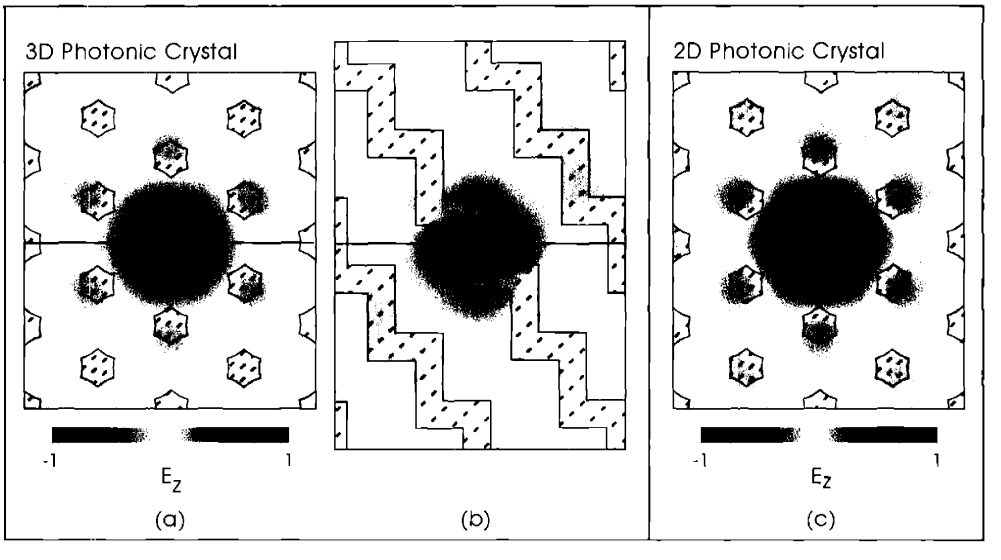

Figure 2-11: (a–b) Defect-mode profile for a point-defect in the 3D crystal created by reducing the radius of a rod in a single rod layer to $r'_r = 0.071\bar{a}$. E_z is plotted for horizontal and vertical cross sections of the 3D crystal. (c) Defect-mode profile for the corresponding 2D crystal.

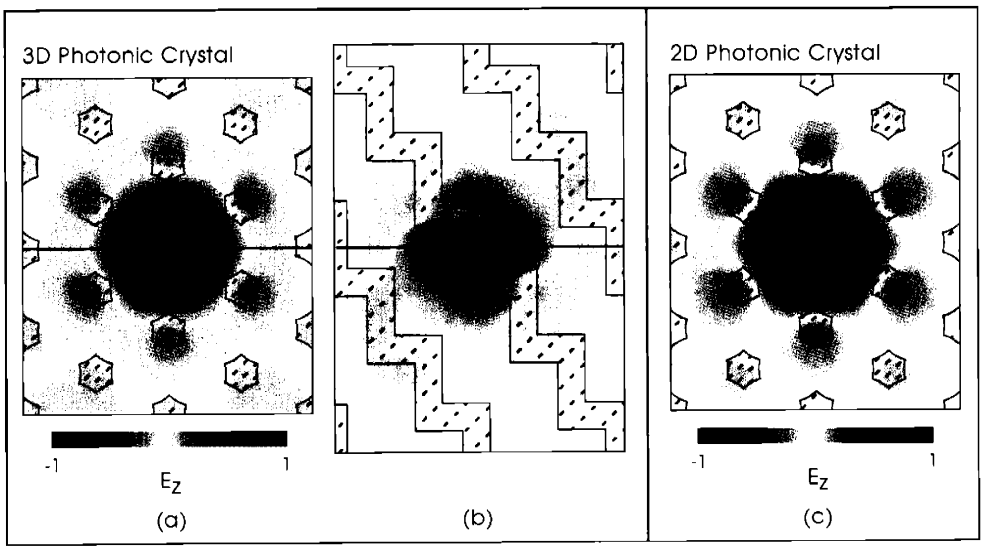

Figure 2-12: (a–b) Defect-mode profile for a point-defect in the 3D crystal created by removing a rod in a single rod layer. E_z is plotted for horizontal and vertical cross sections of the 3D crystal. (c) Defect-mode profile for the corresponding 2D crystal.

geometry of a 2D photonic crystal, allowing comparison between the two systems. The mode polarization, mode profile, and projected band structures of defect modes in the 3D crystal are very similar to those for the corresponding 2D crystal.

Promising directions for future work include the study of physical phenomena previously observed only in two-dimensional photonic crystals, and the design of components for integrated optical circuits within this realistic, three-dimensional system. Building upon the work in this chapter, it has recently been shown that polarization-independent waveguides can be designed in the 3D crystal, and that high (~95%) polarization-independent transmission around waveguide bends can be achieved in a certain frequency range [135]. The ability to emulate modes of a 2D photonic crystal in a 3D crystal with an omnidirectional band gap should also be useful in such applications as designing lossless coupled-cavity waveguides for optical time delays [174, 177] and nonlinear optical devices that exhibit optical bistability [41].

Subsequent to the work in this chapter in Ref. [198], a similar 3D layer-by-layer structure has been identified with square (rather than triangular) symmetry in the plane [136]. The square-symmetric crystal should also be useful for adapting 2D

designs and functionalities to realistic, 3D systems; square symmetry is particularly advantageous for the design of 90° bends and waveguide splitters. It has further been suggested in Ref. [137] that inserting a 2D-periodic slab structure in the middle of a 3D-periodic photonic crystal provides an alternate method of working with 2D-like modes in a system with a full, omnidirectional band gap, providing a radiation-free infrastructure for integrated optical circuit design. This approach has practical advantages for fabrication if the bulk 3D crystal can be made by relatively "easy" methods, such as controlled deposition or self-assembly, and later aligned to and bonded with the 2D slab.

Chapter 3

Toward Photonic-Crystal Metamaterials: Creating Magnetic Emitters in Photonic Crystals

This chapter has previously been published as Ref. [199].

The concept of designing electromagnetic "metamaterials," synthetic structures that exhibit effective properties different from those of their constituent materials, has sparked interest as a means of achieving physical behaviors not found in naturally occurring materials or composites. The realization of negative refraction, for example, may allow for a new class of optical effects and devices [138,139,141]. Here we consider how metamaterials can be constructed within a photonic-crystal system. Previous work in 2D systems has developed an effective medium theory to show that magnetic resonances can lead to a negative effective magnetic permeability, or μ [140]. Here, we use point-defect modes to create magnetic resonances in a 3D photonic crystal. Photonic crystals are periodic dielectric structures with a forbidden frequency range, the band gap, in which light cannot propagate. For frequencies in the gap, light is confined near defects in the structure, which can be designed to have desired frequency and polarization characteristics. We suggest that these defects might be used as building blocks for a new type of metamaterial: photonic crystals with combinations

of point defects chosen to give rise to various, desired properties. In this chapter, we identify building blocks for obtaining magnetic behavior in a non-magnetic dielectric system, quantitatively demonstrating that point-defect modes can be designed to have a magnetic character.

We use the three-dimensional photonic-crystal structure of Chapter 2, which is composed of a stack of alternating layers that mimic 2D TE- and TM-polarized photonic crystals. By creating defects in these layers, the local field pattern and symmetry of the state can be made to resemble either an oscillating magnetic or electric moment, corresponding to the TM and TE polarizations, respectively. In this chapter, we focus on a TE-like point defect that resembles a magnetic moment. We show that such a defect can be incorporated into a finite crystal so that the structure becomes a magnetic emitter: nearly all of the radiated power goes into magnetic, rather than electric, multipole terms, as determined by a multipole decomposition of the far field. This magnetic emitter, unlike an oscillating current loop (a familiar magnetic dipole source), can be designed to operate even at optical frequencies, where naturally-occurring materials have an insignificant or very lossy magnetic response. We believe that such defects are promising building blocks for constructing a new type of metamaterial that exhibits magnetic behavior in a previously inaccessible frequency range. Moreover, because the 3D crystal that we study also supports defect states that resemble electric moments, it could provide a useful infrastructure for designing metamaterials with ferroelectric-like properties.

The crystal structure that we study, described in detail in Ref. [134] and in the previous chapter, has a large, complete, band gap of around 20% of the mid-gap frequency for Si/air structures, and is comprised of two types of alternating layers, rod layers and hole layers. Rod layers are formed by triangular lattices of dielectric rods in air, while hole layers are formed by triangular lattices of air holes in dielectric. It has been shown in Chapter 2 that defects can be designed to be almost completely TM- or TE-polarized in the mid-plane of the layer by working within a single rod or hole layer, respectively. In order to create a defect with magnetic character, we select the TE-polarization (magnetic field perpendicular to the mid-plane of the layer)

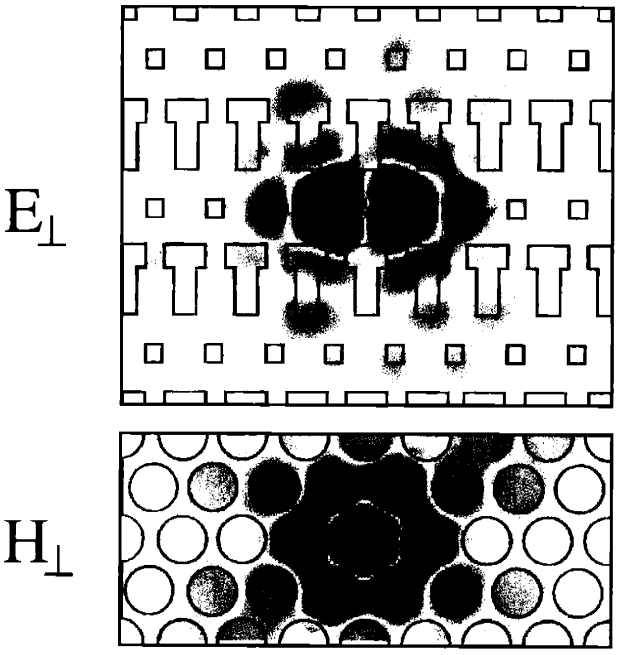

Figure 3-1: Electromagnetic mode profiles for a magnetic-moment-like point defect in a 3D photonic crystal structure. The top and bottom pictures show, respectively, the electric and magnetic field components perpendicular to the plane. Red represents negative values and blue represents positive values; white corresponds to zero. The color map has been exaggerated. Yellow shading indicates dielectric material.

and increase the radius of a single hole from its bulk value of $0.414\bar{a}$ to $0.5\bar{a}$, where $\bar{a}$ is the nearest-neighbor spacing in either a hole or rod layer. Cross sections of the electromagnetic field mode for this defect in the bulk crystal, computed in the standard manner [98], are shown in Figure 3-1. The defect mode resembles the field of an oscillating magnetic moment in several respects. The magnetic field in the midplane is almost completely (99%) polarized perpendicular to the plane 2, and the parity of the state is odd under inversion (the electric field is odd, while the pseudo-vector magnetic field is even). Moreover, the local field pattern of the mode resembles that of an ideal dipole, with some additional structure induced by the photonic crystal.

To determine the degree of magnetic character of the mode, we studied the properties of radiation from such a defect in a finite crystal. The coupling of light into radiation modes will depend on the mode profile at the crystal boundary. In order

to preserve the dominant TE-like polarization of the mode, the crystal was cleaved close to the defect layer, resulting in a crystal that was three hole layers and two rod layers high, with the defect contained in the central hole layer. The radiation fields were calculated using 3D, full-vectorial, finite-difference time-domain (FDTD) simulations of Maxwell's equations [99] with perfectly-matched-layer (PML) boundary regions at the edges of the computational cell [104]. The defect mode was excited using a magnetic-dipole source at the center of the defect. The frequency, amplitude, and quality factor (Q) of the mode were extracted from the field decay after source turn-off, using a low-storage filter-diagonalization method [210]. Figure 3-2 shows snapshots of the radiated fields for three different crystal radii: $r = 3.5\bar{a}, 4.5\bar{a}$, and $5.5\bar{a}$; the corresponding Q values are shown in Table 3.1. Notice that while the mode in the vicinity of the defect looks very similar for all three cases, the structure of the radiated fields changes, with the field amplitudes decreasing in the plane of the crystal for increasing crystal radius.

The magnetic character of the radiation mode was quantitatively determined by performing a multipole decomposition of the far field. For a generalized localized source distribution, the magnetic field in the radiation zone ($r \gg \lambda$) can be written [211, Chap. 9]:

$$\vec{H}(r \gg \lambda) \cong \frac{e^{ikr-i\omega t}}{kr} \sum_{l,m} (-i)^{l+1} [a_E(l,m)\vec{X}_{lm} + a_M(l,m)\hat{r} \times \vec{X}_{lm}]$$

where the $\vec{X}_{lm}$'s are the vector spherical harmonics, given by

$$\vec{X}_{lm}(\theta,\phi) = \frac{1}{\sqrt{l(l+1)}} \vec{L} Y_{lm}(\theta,\phi),$$

and $\vec{L}$ is the angular-momentum operator, $\frac{1}{i}(\vec{r} \times \vec{\nabla})$. a_M and a_E are the magnetic and electric multipole moments, respectively, and each multipole radiates a time-averaged power of $\frac{\sqrt{\mu_o/\epsilon_o}}{2k^2}|a(l,m)|^2$. Using the orthogonality relations for the vector spherical harmonics,

$$\int \vec{X}^*_{l'm'} \cdot \vec{X}_{lm} \, \mathrm{d}\Omega = \delta_{ll'}\delta_{mm'}$$

	$r = 3.5\bar{a}$	$r = 4.5\bar{a}$	$r = 5.5\bar{a}$
Q	174	299	320
$\|a_M(1,0)\|^2$	5%	30%	37%
$\|a_M(3,0)\|^2$	50%	50%	50%
$\|a_M(5,0)\|^2$	8%	10%	8%
any other $\|a_M(l,m)\|^2$	$\leq 3\%$	$< 1\%$	$< 0.5\%$
any $\|a_E(l,m)\|^2$	$\leq 4\%$	$< 0.5\%$	$< 0.5\%$
M_{pwr}	79%	96%	98%

Table 3.1: Quality factor Q and dominant multipole coefficients for the radiating point-defect states shown in Figure 3-2. The radius of the photonic crystal is given by r; $\bar{a}$ is the in-plane lattice constant of the crystal. M_{pwr} denotes the percentage of the total radiated power due to magnetic multipole terms.

and

$$\int \vec{X}^*_{l'm'} \cdot (\hat{r} \times \vec{X}_{lm})\, \mathrm{d}\Omega = 0,$$

we obtained the multipole coefficients a_M and a_E by numerical integration over a sphere near the boundary of the computational cell.

The results are shown in Table 3.1. The absolute value of the multipole moments squared, $|a(l,m)|^2$, is expressed as a percentage of the total power radiated. For all three crystal structures, the largest multipole moments were magnetic with m=0 and l=1,3 or 5. As the crystal diameter increases, the strength of the $(1,0)$ magnetic dipole term increases, while the strength of the $(3,0)$ and $(5,0)$ terms remain approximately fixed. This trend can be understood from the fact that the crystal must block radiation in the lateral direction, as seen in Figure 3-2. As the $l = 1$ component increases, it cancels the $l = 3$ component to reduce the amplitude of the fields in the plane of the crystal. The percentage of the power that is emitted in magnetic multipole terms, M_{pwr}, is also given in the table. The power is mostly magnetic for all three crystals, with M_{pwr} increasing to a maximum of 98% for the largest crystal radius studied. Moreover, the crystal height was found to be an important parameter in determining the percentage of power that goes into magnetic radiation; increasing the height of the $r = 4.5\bar{a}$ crystal so that it included nine hole layers significantly reduced M_{pwr}, from 96% to 60%.

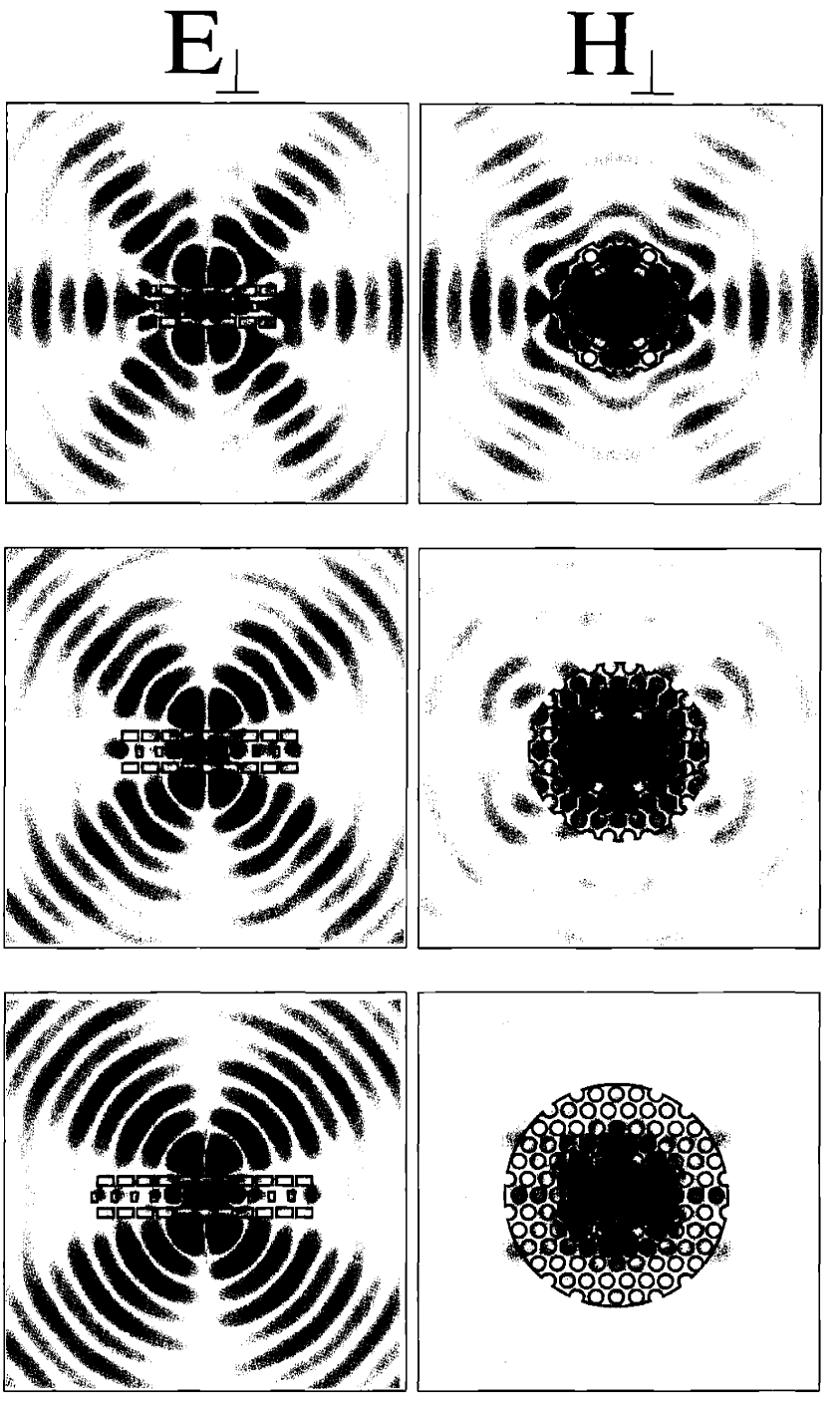

Figure 3-2: Radiating point defect modes for three different cuts of the photonic crystal. The left- and right-hand columns show the electric and magnetic field components perpendicular to the plane, respectively. The colormap has been exaggerated to make the far-field radiation more visible. Yellow shading indicates dielectric material.

The key to the magnetic nature of the radiation, we believe, is the primarily TE character of the mode in the mid-plane– in two dimensions, this would lead to purely magnetic radiation, and the only electric multipole components in 3D are due to the deviations from this TE character. Away from the mid-plane, the deviations take the form of $\hat{z}$ components of $\vec{E}$; these components can induce electric radiation, but that radiation is primarily in the lateral directions. Therefore, by increasing the lateral crystal size, we can substantially eliminate this radiation and increase the magnetic character, as observed in Table 3.1. Conversely, as the vertical size is increased, deviations from TE character become more pronounced and consequently, the percentage of magnetic radiation is decreased.

Starting with a point defect in a bulk photonic crystal whose local field pattern resembles an oscillating magnetic moment, we have shown that the crystal boundary can be cut so that the radiation from the defect mode is almost completely magnetic. Unlike traditional magnetic sources, this magnetic emitter can be designed to operate even at optical frequencies. (In a practical implementation, the defect mode would be excited by shining light onto the crystal from an optical source. This process could be enhanced by incorporating a fluorescent dye within the crystal to absorb outside the band gap and emit at the frequency of the point-defect mode.) Using the point-defect mode that we study here as a building block, it may now be possible to design arrays of defects that yield magnetic bulk properties in photonic crystals; "Ferromagnetic" and "anti-ferromagnetic" arrays, for example, can be created by operating at frequencies corresponding to wave vectors at the edge of the Brillouin zone, where adjacent defect states will have phase shifts of ~ 0 or $\sim \pi$. Creating defects within the rod layer of the 3D photonic crystal, which behave like electric multipoles, could similarly allow the design of ferroelectric and antiferroelectric arrays. Investigation of the properties of these defect complexes is a promising direction for future work.

Chapter 4

Slow-light Enhancement of Radiation Pressure in an Omnidirectional-Reflector Waveguide

This chapter has been submitted for publication; see Ref. [201].

The group velocity of light can be dramatically slowed in photonic crystals. Slow light enhances a variety of optical phenomena, including nonlinear effects, phase-shift sensitivity [156], and low-threshold laser action due to DFB gain enhancement [157, 158]. Here we demonstrate that slow light can also enhance radiation pressure. Using numerical calculations, we show how a slow-light, photonic-crystal structure incorporating omnidirectionally-reflecting mirrors can be used to maximize the radiation pressure between two surfaces.

For Fabry-Perot cavities, the effect of radiation pressure on the motion of the mirror surfaces has been extensively studied. The magnification of field intensity inside the cavity results in strong optomechanical coupling, leading to interesting classical effects such as optical bistability [161] and quantum optical effects such as ponderomotive squeezing [162], the generation of nonclassical states of light [163], and the

potential entanglement of macroscopic objects through optomechanical cooling [164]. In the Fabry-Perot system, the direction of light propagation is fixed perpendicular to the mirror surfaces, and the reflectivity of at least one mirror is necessarily less than one to allow light to couple into the cavity. We introduce a generalized system that lifts both restrictions and is particularly well-suited for embodiment in microscale devices.

The *omnidirectional-reflector waveguide* structure we consider is formed by two omnidirectional mirrors [18] separated by a distance comparable to the wavelength. Light traveling in the waveguide gives rise to a radiation pressure between the mirror surfaces that depends on the intensity and the mode characteristics. We first optimize the mirror structure to maximize the radiation pressure for fixed electromagnetic energy in the field. We then calculate the radiation pressure as a function of distance as the mirrors are pushed together. As the distance decreases, intensity buildup results from the reduction of the group velocity of the waveguide mode. We show that in the absence of losses, the force *diverges* at waveguide cutoff for constant input power.

The system is shown in Figure 4-1(a). Two semi-infinite multilayer films are separated by an air region of thickness d. Each of the films consists of a stack of alternating high- and low-dielectric layers with period a. For definiteness, we take the refractive indices to be $n_{\rm hi} = 3.45$ and $n_{\rm lo} = 1.45$, corresponding to Si and SiO_2 at 1.55μm. The relative layer thicknesses are determined by the quarter-wave condition $n_{\rm hi}d_{\rm hi} = n_{\rm lo}d_{\rm lo}$, which we later show to be an optimal case, along with the constraint that $d_{\rm hi} + d_{\rm lo} = a$, yielding $d_{\rm hi} = 0.296a$ and $d_{\rm lo} = 0.704a$. Waveguide modes can be supported in the air region between the films. Superimposed on Figure 4-1 is the fundamental guided mode, propagating in the direction shown.

It is sufficient to consider solutions of Maxwell's equations that are uniform in the y direction. The electric field can then be written in the form $\vec{E}(x,y,z,t) = \mathrm{Re}\left[\vec{E}_{k,\omega}(z)e^{ikx-i\omega t}\right]$, where we have made use of the translational symmetry in the x direction. The solutions can be divided into TE modes ($\vec{E} \parallel \hat{y}$ and $\vec{H} \perp \hat{y}$), and TM modes ($\vec{H} \parallel \hat{y}$ and $\vec{E} \perp \hat{y}$). The TE dispersion relation is shown in Figure 4-

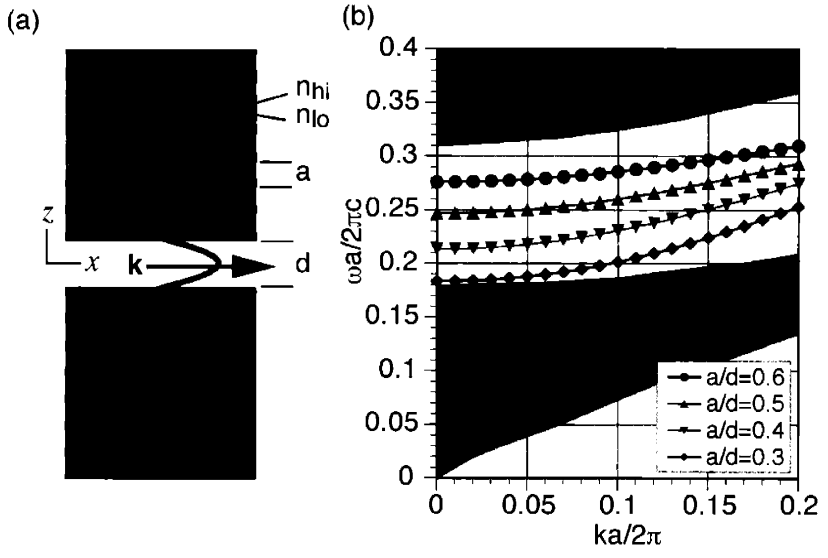

Figure 4-1: (a) Omnidirectional-reflector waveguide structure: two multilayer films of period a are separated by a distance d; each film is composed of alternating layers with refractive indices n_{hi} and n_{lo}. Guided modes propagate in the air region between the films in the direction indicated by the wave vector $\vec{k}$. The field profile of the fundamental mode is superimposed on the figure. (b) Dispersion relation for the structure shown in (a) for modes with $\vec{E} \parallel \hat{y}$. The high- and low-index layer thicknesses were taken to satisfy the quarter-wave condition for $n_{\text{hi}} = 3.45$ and $n_{\text{lo}} = 1.45$. Shaded grey regions indicate bulk modes of the multilayer film, and colored symbols indicate the dispersion relation for the fundamental mode of the waveguide for several different values of a/d.

1(b), where the dimensionless quantity $\omega a/2\pi c$ is plotted as a function of $ka/2\pi$. Modes were computed by planewave expansion [98]. Shown in grey are the modes of an infinite multilayer film system, or bulk modes. Colored symbols indicate the dispersion relation for the fundamental waveguide mode for several values of d/a. A frequency and wave vector within the band gap of the bulk system indicates the mode is guided in the air region between the films. For each value of d/a, the group velocity of the guided mode goes to zero at $ka/2\pi = 0$. As a/d decreases, the mode shifts down in frequency, and higher-order modes will enter the band gap. We focus on the force on the multilayer films produced by light traveling in the fundamental guided mode.

The force was calculated using a Maxwell stress-tensor formalism [212, Sect. 6.8], [213]. The time-averaged force is given by

$$F_\alpha = \oint_S da \sum_\beta \frac{1}{8\pi} \mathrm{Re}\left[\epsilon E_\alpha^* E_\beta - \frac{1}{2}\delta_{\alpha\beta}\epsilon\,|E|^2 + \mu H_\alpha^* H_\beta - \frac{1}{2}\delta_{\alpha\beta}\mu\,|H|^2\right] n_\beta. \qquad (4.1)$$

where the integral is taken over a surface S enclosing a volume V, which we take to be a box with parallel faces of area A at $z = 0$ and $z = Z$; $\hat{n}$ is the outward surface normal. For guided modes, the contribution from the face at Z goes to zero as $Z \to \infty$. The contribution from the sides of the box is also zero, since terms from parallel faces cancel, and the total force is given by the midplane integral. It can easily be seen that F_x and F_y are identically zero; as a result of the mirror symmetry of the structure with respect to the $z = 0$ plane, modes can always be chosen such that either $\{E_z, H_x, H_y\}$ or $\{H_z, E_x, E_y\}$ is zero there. The time-averaged force per area A in the z direction on the upper film reduces to

$$F/A = -\frac{1}{16\pi}\mathrm{Re}\left(E_z^* E_z - E_x^* E_x - E_y^* E_y + H_z^* H_z - H_x^* H_x - H_y^* H_y\right).$$

To determine the optimal multilayer structure, we first consider the maximum achievable optical force for a fixed separation between the multilayer films and a *fixed amount of energy in the electromagnetic field* (as contrasted to fixed input power).

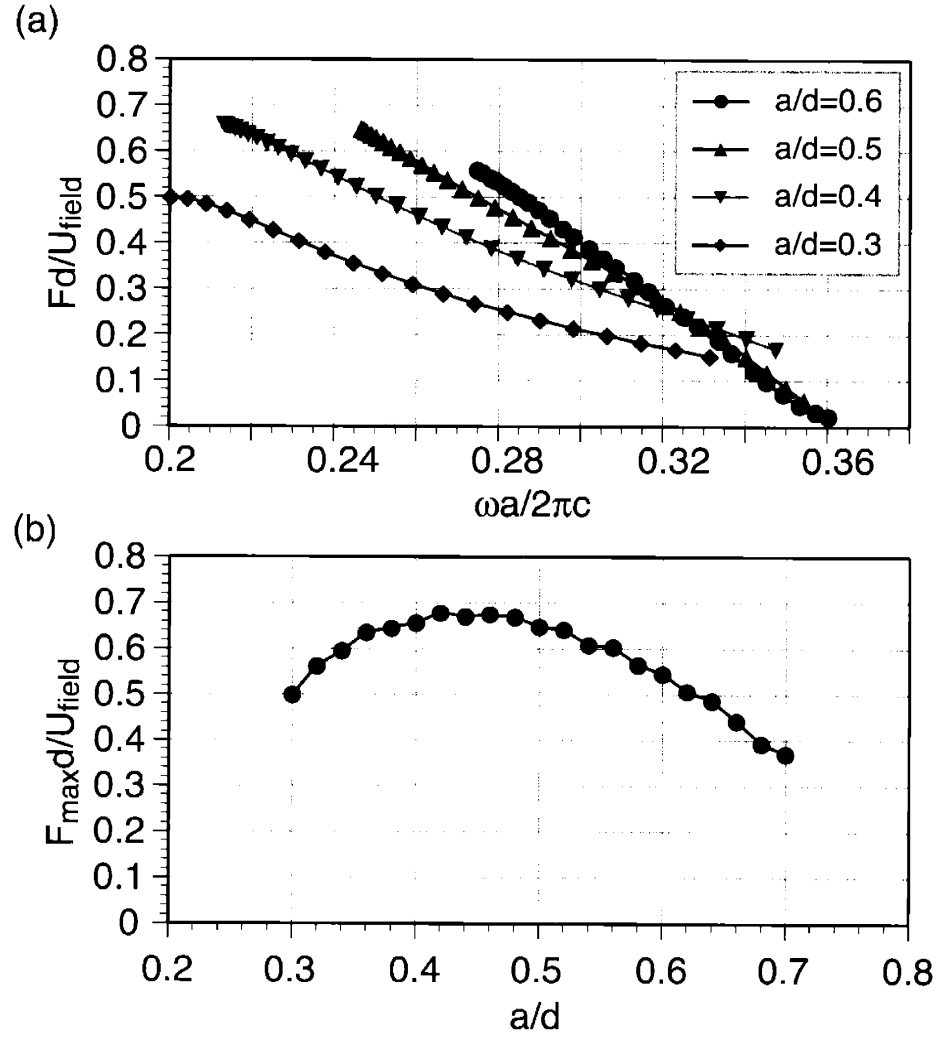

Figure 4-2: (a) Force between the multilayer films resulting from light traveling through the waveguide. Plotted is the dimensionless quantity Fd/U_{field} as a function of the dimensionless quantity $\omega a/2\pi c$, where F is the force due to area A, U_{field} is the electromagnetic field energy contained in a slice of the waveguide that intersects the z axis in area A, and ω is the waveguide mode frequency. (b) Maximum force from (a) as a function of a/d. The peak in the curve gives the maximum attainable force for fixed separation of the films d and energy in the fields U_{field}, where the maximization is over the period of the films a and the frequency ω.

The electromagnetic fields at a given frequency were calculated using planewave expansion [98]. Figure 4-2(a) illustrates the dependence of the force on the frequency ω and the period a. We plot the dimensionless quantity Fd/U_{field} as a function of $\omega a/2\pi c$ for several values of a/d, where F is the force due to area A, and U_{field} is equal to the integral of the electromagnetic energy density over A and z. The value of Fd/U_{field} is always positive: the effect of the light in the guided mode is to push the two films apart. For each value of a/d, the force increases with decreasing frequency until it reaches the cutoff frequency of the mode, $\omega(k = 0)$ (see also Fig. 4-1(a)). We note that the maximum value of the force F_{max} is independent of polarization, since TE and TM modes are degenerate at $k = 0$.

It can be shown by either quantum mechanical or classical arguments [214] that, for a dielectric or metallic structure characterized by parameter shift ξ, supporting a single mode at frequency ω and wave vector $\vec{k}$, the time-averaged force on the dielectric is given by

$$F = -\frac{1}{\omega}\frac{\partial\omega}{\partial\xi}\bigg|_{\vec{k}} U_{\text{field}}, \tag{4.2}$$

where it is assumed that the modal field decays to zero perpendicular to the propagation direction. It can be seen from Fig. 4-1(b) that for a given pair of multilayer films (fixed a), the frequency of the guided mode at fixed wave vector changes most quickly with displacement d at $k = 0$ (i.e. the lines labelled by a/d are furthest apart at $k = 0$), consistent with Fig. 4-2(a).

In Fig. 4-2(b), we plot $F_{\text{max}}d/U_{\text{field}}$ as a function of a/d. The value increases and then decreases with a/d, peaking near $a/d = 0.45$. Referring to Fig. 4-1(b), we see that the largest force is obtained for values of a/d for which the frequency of the waveguide mode at $k = 0$ is near the center of the band gap. In this range, the confinement of the electromagnetic field to the air region between the films is highest, and the values of the electromagnetic fields on the midplane are maximized, leading to the largest force; $F \approx 0.68U_{\text{field}}/d$. For similar reasons, the quarter-wave stack is an optimal structure: choosing the relative layer thicknesses to satisfy the quarter-wave condition maximizes the $k = 0$ band gap, allowing the greatest modal

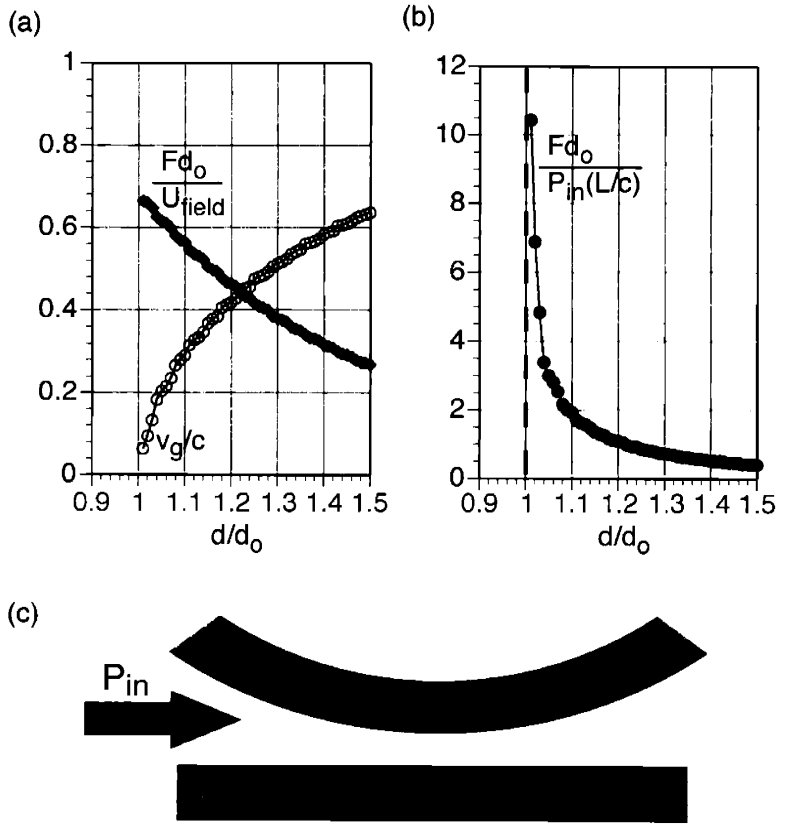

Figure 4-3: (a) Force as a function of separation between the films, for fixed operating frequency and electromagnetic field energy. As d is decreased to d_o, the group velocity of the waveguide mode decreases to zero, shown as the dimensionless quantity v_g/c. (b) Force as a function of separation between the plates, for fixed operating frequency and waveguide input power. As d is decreased to d_o, the force goes to infinity. (c) A possible geometry for achieving constant input power over a range of separations.

confinement and hence the largest force. We have verified this statement explicitly by fixing $a/d = 0.45$ and varying $d_{\rm hi}$ and $d_{\rm lo}$.

We next consider the distance dependence of the force. Suppose we choose the operating frequency ω and the period a so as to maximize the force at distance d_o for fixed electromagnetic field energy $U_{\rm field}$. That is, we choose $a = 0.45 d_o$ and $\omega = \omega(k = 0, a/d_o = 0.45)$. As the separation is decreased from some initial value to d_o, the force increases, as shown in Fig. 4-3(a). The group velocity of the waveguide mode at ω simultaneously decreases to zero.

Now consider what happens at *fixed input power*, a more relevant constraint for

any experimental realization of such a device. The energy in the field can be written as as $U_{\text{field}} = P_{\text{in}} L/v_g$, where L is the length in the propagation direction of the volume V with cross-sectional area A. In Fig. 4-3(b), we plot the dimensionless quantity $f(d/d_o) \equiv \frac{F d_o}{P_{\text{in}}(L/c)}$. As can be seen from the graph, $f \to \infty$ as $d/d_o \to 1$. At fixed frequency and input power, the force between the films is given by

$$F(d) = f(d/d_o)\frac{P_{\text{in}}(L/c)}{d_o} \tag{4.3}$$

and *the force becomes infinite as the separation between the plates approaches* d_o. Physically, as the distance between the plates decreases, the group velocity of the waveguide mode decreases to zero. For a fixed power input, the light takes longer and longer to travel down the waveguide, and the magnitude of the field builds up, leading to a *divergence* in the force. For separations smaller than d_o, the operating frequency is below the cutoff frequency of the mode, and the fields will decay evanescently along the waveguide, reducing the force.

In practice, the divergence at d_o will be removed by loss mechanisms, including losses due to finite mirror thickness, material absorption, input coupling, and scattering from disorder. An accurate numerical estimate of the achievable force will thus depend on a detailed analysis of these mechanisms.

Figure 4-3(c) shows one means of achieving a nearly constant power input for a range of separations. Here, a cylinder coated with a multilayer film forms the top surface of the waveguide. This geometry not only eases the alignment requirements between the two surfaces, but also forms an adiabatic input taper for coupling, e.g. a tightly-focussed laser mode, to the guided mode of the waveguide. Due to the taper, a change in the minimum film separation will correspond to a much smaller fractional change in the film separation at the input, yielding a nearly constant input power. Moreover, any reflections from the output taper back into the waveguide will in fact increase the total force, as they increase the total amount of power in the waveguide.

For larger separations between the multilayer films, the central air waveguide will be multimode. The total force between the films is given by the sum over the force

contributions due to the individual modes. As a result, the force as a function of distance will exhibit peaks at the cutoff distances of each of the higher-order modes. Unlike the case of radiation pressure in mirrored Fabry-Perot cavities [161], these peaks are assymetric around the cutoff length.

Since the key condition for a force divergence is a zero group-velocity mode at non-zero frequency, a divergence is also expected for metallic waveguides. In the absence of loss, the time-averaged force on the metallic waveguide walls is calculated to be

$$\frac{Fd}{P_{\text{in}}(L/c)} = \frac{\pi nc}{2\omega} \frac{1}{\sqrt{d^2 - \left(\frac{\pi nc}{\omega}\right)^2}}$$

for either TE or TM modes. ($F = 0$ for the TEM mode, since its frequency is independent of waveguide width.) The force at constant input power thus diverges as $d \rightarrow \pi nc/\omega$ and the mode reaches cut off. However, to maximize the force, the distance between the plates (and consequently the operating wavelength) should be made as small as possible. Due to the high losses in metals at optical wavelengths, the force divergence should be far easier to observe in dielectric systems.

A number of applications of this work should follow from the ability to modify the mechanical oscillation of the structure by optical means, such as sensitive control and positioning on the microscale. Operating the structure in *reverse*, by using an applied force to modify the waveguide group velocity, results in a tunable time-delay device. Moreover, since our omnidirectional-reflector waveguide may be viewed as a Fabry-Perot cavity operated via a novel sidewise-coupling scheme, it should provide an interesting alternate system in which to explore the rich collection of classical and quantum effects resulting from strong optomechanical coupling in Fabry-Perot systems.

Chapter 5

Slow-Light, Band-Edge Waveguides for Tunable Time Delays

This chapter has been submitted for publication; see Ref. [202].

Delaying an optical signal is useful for a number of applications, including signal processing, logic, radio-frequency (RF) photonics, and enhanced nonlinearities [173]. Several recent research efforts have focussed on replacing relatively bulky fiber-optic delay-line systems [167] with compact integrated devices. Approaches have included the use of all-pass filters, which can be implemented either in microring resonators [173] or in photonic crystal microcavities [174], and coupled-cavity waveguides [152] in photonic crystals [155, 175–177]. However, both types of time-delay devices are intrinsically lossy (even in the absence of fabrication disorder) unless implemented in 3D photonic crystals [5], which remain difficult to fabricate at optical length scales.

Here, we examine another approach to integrated optical time delays: slow-light, band-edge photonic-crystal waveguides. Work on multilayer films has previously suggested that, near a photonic band edge, a large delay tunability can be achieved for a small change in refractive index [215]. While realistic three-dimensional implementations of such structures tend to suffer radiative input-coupling loss, it has recently been shown [216] that apodization can in principle reduce that loss to zero. This result makes slow-light structures attractive candidates for *highly-tunable, low-loss*

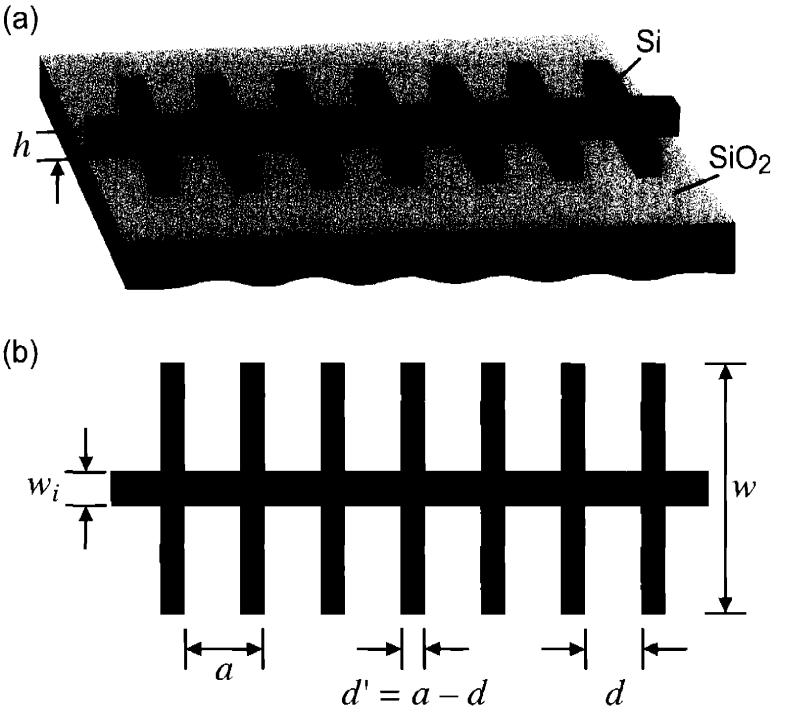

Figure 5-1: (a) 3-D perspective view of a slow-light grating structure. (b) Top view.

optical time delays. We first define appropriate figures of merit for the comparison of tunable time-delay structures. We then show that values for a realistic sample structure are well approximated by a simple quadratic-band model, greatly simplifying design and optimization of such devices.

A sample slow-light structure is shown in Figure 5-1. The structure is formed by a silicon strip waveguide with grated sidewalls (allowing ease of apodization [217]) resting on a silicon dioxide substrate. Silicon has low absorption near 1.55μm, high refractive index, and large change in index with temperature; the index varies by >1% from 100 to 300 ℃ [218].

A small shift in a refractive index of the structure will slightly shift the dispersion relation. For a given operating frequency, the group velocity of light traveling through the the structure will change from v_g to v_g' (see Fig. 5-2). At the edge of the Brillouin zone, the group velocity goes to zero (as is typical of a variety of 1-, 2-, and 3-D periodic, dielectric structures [5]). As a result, a small shift in index can result in a

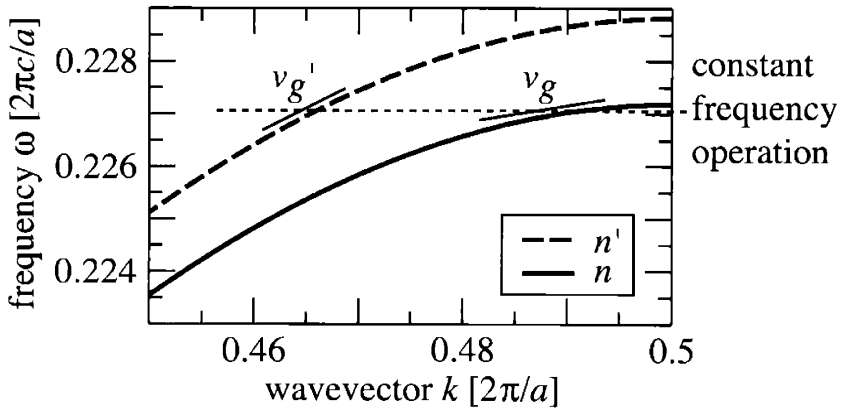

Figure 5-2: Illustration showing how a small shift in refractive index can lead to a large shift in group velocity for operating frequencies near a photonic band edge.

large change in group velocity, and consequently in time delay.

To quantify the effect, we define the *sensitivity*, a dimensionless figure of merit given by the fractional change in time delay over the fractional change in index:

$$s \equiv \frac{\Delta\tau/\tau}{\Delta n/n} = \frac{\Delta\left(1/v_g\right)_{\Delta n}}{1/v_g}\frac{1}{\Delta n/n}, \tag{5.1}$$

where τ is the time delay, v_g is the waveguide group velocity, and $\Delta\left(1/v_g\right)_{\Delta n} = 1/v_g' - 1/v_g$ is the change in group velocity due to a shift from n to $n' = n + \Delta n$. s indicates the advantage of the slow-light waveguide structure as compared to a bulk material, for which $\omega = ck/n$ and s=1.

For a fixed fractional index shift $\Delta n/n$ and a desired tunable delay $\Delta\tau$, the required length is given by

$$L = \left|\frac{\Delta\tau}{\Delta(1/v_g)_{\Delta n}}\right| = \left|\frac{\Delta\tau}{\Delta n/n}\frac{v_g}{s}\right|. \tag{5.2}$$

Waveguides with low group velocity and high sensitivity allow a shorter tuning region, leading to lower power and easier integration.

Sensitivity is high near the band edge because of group-velocity dispersion ($d^2\omega/dk^2 \neq 0$), but dispersion can also limit the performance of the device. It is useful to define a *dispersion figure of merit* to measure the amount of pulse spreading relative to the

typical size $1/\Delta\omega$ of temporal features (e.g. pulses or chirp autocorrelations [219]), where $\Delta\omega$ is the bandwidth.

$$d \equiv \frac{\tau|_{\omega} - \tau|_{\omega-\Delta\omega}}{1/\Delta\omega} = \frac{L\Delta(1/v_g)_{\Delta\omega}}{1/\Delta\omega} \tag{5.3}$$

where $\Delta\left(1/v_g\right)_{\Delta\omega} \equiv \frac{1}{v_g}\Big|_{\omega} - \frac{1}{v_g}\Big|_{\omega-\Delta\omega}$ is the change in inverse group velocity across the bandwidth. Making use of Eq. 5.2, d may alternatively be written as

$$d = |\Delta\tau|\Delta\omega\frac{\Delta\left(1/v_g\right)_{\Delta\omega}}{\left|\Delta\left(1/v_g\right)_{\Delta n}\right|}. \tag{5.4}$$

We first analyze the figures of merit within an approximate quadratic model, and then perform exact calculations for the structure of Fig. 5-1. Near the band edge ω_{be}, $\omega(k)$ can be approximated by a quadratic curve,

$$\omega(k) = \omega_{\mathrm{be}} - \alpha(\pi/a - k)^2,$$

where $\alpha = -\frac{1}{2}\, d^2\omega/dk^2|_{\pi/a}$. Similarly, the shifted band can be written as

$$\omega'(k) = \omega_{\mathrm{be}} + \delta\omega - (\alpha + \delta\alpha)(\pi/a - k)^2.$$

Let $\Delta\omega_{\mathrm{be}} \equiv \omega_{\mathrm{bc}} - \omega$. Then

$$s \approx -\frac{1}{\Delta n/n}\left(1 - \frac{1}{\sqrt{(1+\delta\omega/\Delta\omega_{\mathrm{be}})(1+\delta\alpha/\alpha)}}\right). \tag{5.5}$$

As the operating frequency approaches the band edge, $|s|$ increases until it reaches a limiting value of $|n/\Delta n|$; unlike in a bulk medium, s diverges as $\Delta n/n \to 0$. The length is given by

$$L \approx \left|\frac{2\Delta\tau\sqrt{\alpha\Delta\omega_{\mathrm{be}}}}{1 - [(1+\delta\omega/\Delta\omega_{\mathrm{be}})(1+\delta\alpha/\alpha)]^{-1/2}}\right|. \tag{5.6}$$

L decreases to zero near the band edge, scaling as $L = 2|\Delta\tau(\alpha\Delta\omega_{\mathrm{be}})^{1/2}|$ for $|\Delta\omega_{\mathrm{be}}| \ll$

$|\delta\omega|$. The dispersion figure of merit is approximated by

$$d \approx \frac{L\Delta\omega}{2\sqrt{\alpha}}\left[\frac{1}{\sqrt{\Delta\omega_{\mathrm{be}}}} - \frac{1}{\sqrt{\Delta\omega_{\mathrm{be}}+\Delta\omega}}\right]. \tag{5.7}$$

Because L scales as $\sqrt{\alpha}$ (up to small corrections that are first order in $\delta\alpha/\alpha \propto \Delta n/n$), d is nearly independent of α within the quadratic band model. Approaching the band edge, dispersion increases to a limiting value of $|\Delta\tau|\Delta\omega$. Strong gratings/large band gaps (corresponding to small curvature α) thus tend to decrease the required length for fixed dispersion.

Sensitivity, length, and dispersion figures of merit were calculated from the dispersion relation of the structure, which was obtained from fully-vectorial solutions of Maxwell's equations in a plane-wave basis [98]. The structural parameters were taken to be h=0.26μm, w_i=0.15μm, a=0.35μm, d'=0.15μm, d=0.20μm, and w=1.0224μm, such that the minimum feature size was not below 0.15μm. For n_{Si}=3.4845 and $n_{\mathrm{SiO_2}}$=1.45, the first band gap was 23.5% of the mid-gap frequency for odd modes with respect to the mirror plane of the structure ($\vec{E}$ mostly parallel to the substrate). For n_{Si}=3.4845, the band edge frequency was calculated to be $\omega_{\mathrm{be}} = 0.22718\,2\pi c/a$ for the lowest band, or $\omega_{\mathrm{be}}/2\pi$=190THz ($\lambda$=1.54$\mu$m). For n'_{Si}=3.45 ($\Delta n/n$=$-$0.01), the band edge shifted to $\omega_{\mathrm{be}} = 0.22880\,2\pi c/a$, or $\omega_{\mathrm{be}}/2\pi$=200THz ($\lambda$=1.53$\mu$m). Figure 5-2 shows the lowest band near the band edge.

Figs. 5-3 and 5-4 show the results of the exact numerical calculation (symbols) overlayed on the expressions for s, L, and d obtained from the quadratic band model of Equations 5.5, 5.6, and 5.7 (solid lines). As can be seen from the figure, the quadratic band model is an excellent predictor of the results within at least 1% from the band edge. Values of $\delta\omega$ ($0.00162\,2\pi c/a$) and α ($1.550\,ca/2\pi$), and $\delta\alpha$ ($0.025\,ca/2\pi$) were obtained from a fit to the data of Fig. 5-2 at $k = \pi/a$. In general, we expect the range of validity of the quadratic band model to decrease as the band gap is decreased.

Optimization, fabrication, and optical characterization of slow-light structures are ongoing [220]. Analogous to fiber-optic systems [167], gratings with alternating dispersion signs (e.g. designed to operate below or above the first band gap) may be

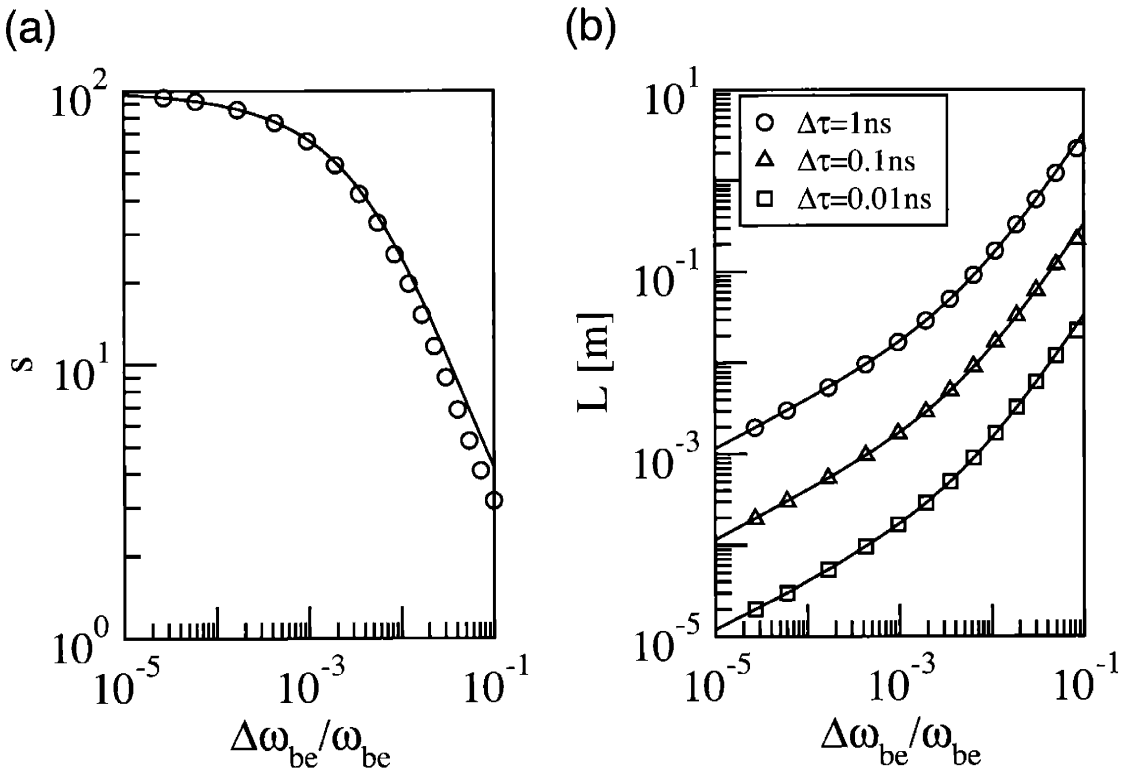

Figure 5-3: (a) Sensitivity figure of merit for the structure of Fig. 5-1 as a function of fractional frequency from the band edge. (b) Required length for different amounts of tunable time delay. Symbols/solid lines are exact/quadratic-approximation calculations.

used for dispersion control, allowing larger delays. A crucial question to be answered by experiment is how close to the band edge a grating device can be operated in practice. While it has been suggested that band-edge devices should be extraordinarily sensitive to disorder [155], disorder is a problem for *any* slow-light device, including those based on coupled-cavity waveguides [190]. It can be shown from the coupled-mode theory of Chapter 6 that reflection loss typically scales as $1/v_g^2$, while other loss scales as $1/v_g$. Further understanding of disorder effects and detailed comparisons of implementation schemes will be important for a variety of slow-wave devices and phenomena, e.g. magnification of nonlinear phase shifts [156], gain [158], and radiation pressure (as studied in Chapter 4) in addition to the class of optical time-delay structures introduced here.

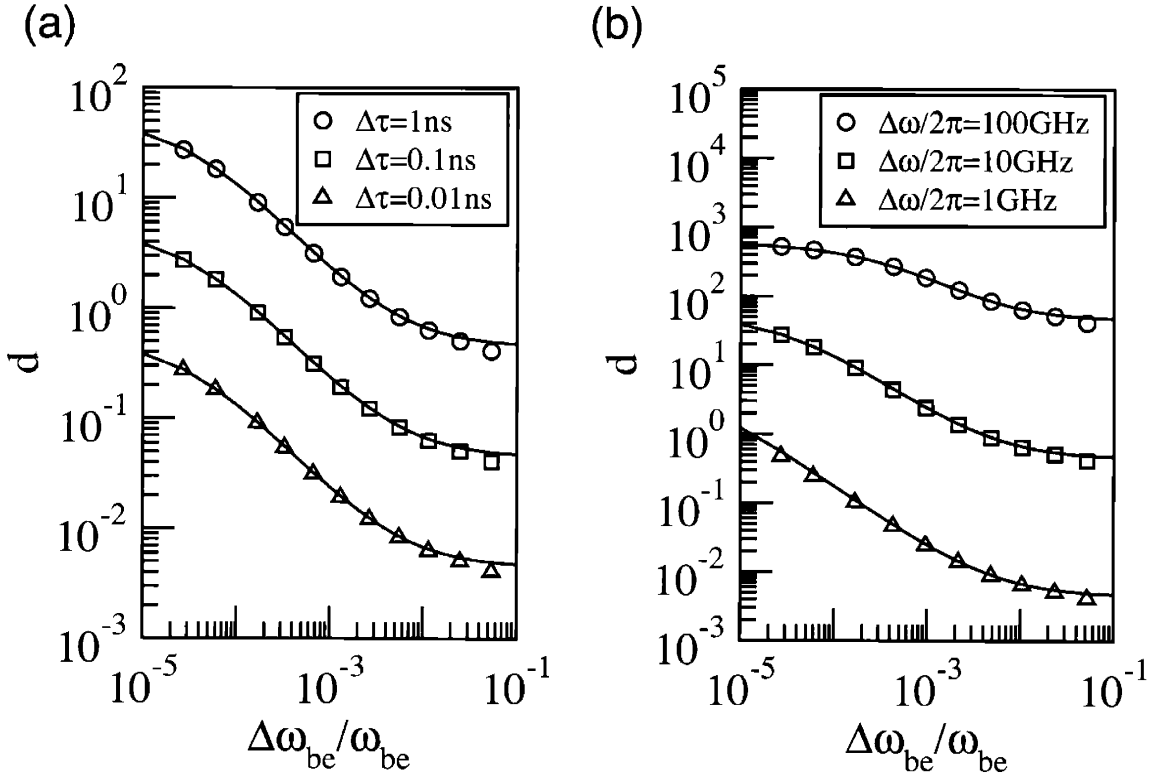

Figure 5-4: Dispersion figures of merit for the structure of Fig. 5-1 as a function of fractional frequency from the band edge for (a) fixed bandwidth $\Delta\omega/2\pi$=10GHz and (b) fixed time delay $\Delta\tau$=1ns. Symbols/solid lines are exact/quadratic-approximation calculations.

Chapter 6

Effect of a Photonic-band Gap on Scattering from Waveguide Disorder

This chapter will also be published as Ref. [200].

A photonic crystal blocks the propagation of fields within a certain frequency range, or photonic band gap, thereby confining light to the vicinity of defects in its periodic structure [5]. Linear defects, which act as waveguides, are promising building blocks for the design of optical integrated circuits in the infrastructure provided by the photonic crystal [37]. Understanding the effects of disorder in these systems (arising, for example, from imperfect fabrication) is thus a topic of both fundamental and practical importance. However, while the effect of disorder on the bulk band gap of the crystal is well understood [179,180], the effect of disorder on transport through photonic-crystal waveguides has seen only limited study for specific cases [190–193].

In this chapter, we derive the general principles that govern reflection and scattering due to arbitrary disorder in photonic-crystal waveguides. By working with a basis of Bloch states, we develop an extension of traditional coupled-mode theory [194] that is valid even for strongly-periodic, high-index-contrast systems. Unlike previous work, our approach is not limited to slowly-varying perturbations [221], it

develops the coupled-mode equations in space rather than in time [222], and it uses a fixed basis [216]. From our theory, an explicit formula for the reflection is obtained, yielding physical insight into the effect of the band gap on scattering. We find that, in the experimentally-relevant limit of weak disorder,[1] the photonic band gap suppresses radiation loss *without* redirecting light into reflection. As a result, reflection losses are the same as in a comparable index-guided waveguide, and the overall transmission is higher. These general results are verified by direct numerical simulations of Maxwell's equations in an example system.

We begin by writing the dielectric constant of the waveguide as $\varepsilon(x,y,z)+\Delta\varepsilon(x,y,z)$, corresponding to a z-periodic, unperturbed waveguide ε of period a plus a perturbation $\Delta\varepsilon$ due to disorder, where z is the propagation direction. For a definite frequency ω, the fully-vectorial source-free Maxwell's equations can be rewritten [216]:

$$(\hat{A}+\Delta\hat{A})|\psi\rangle = -i\frac{\partial}{\partial z}\hat{B}|\psi\rangle,$$

where $|\psi\rangle$ is a four-component column vector containing the transverse (xy) fields $\mathbf{E}_t$ and $\mathbf{H}_t$,

$$|\psi\rangle \equiv \begin{pmatrix} \mathbf{E}_t(x,y,z) \\ \mathbf{H}_t(x,y,z) \end{pmatrix} e^{-i\omega t},$$

and the operators are defined by

$$\hat{A} \equiv \begin{pmatrix} \frac{\omega\varepsilon}{c} - \frac{c}{\omega}\nabla_t \times \frac{1}{\mu}\nabla_t \times & 0 \\ 0 & \frac{\omega\mu}{c} - \frac{c}{\omega}\nabla_t \times \frac{1}{\varepsilon}\nabla_t \times \end{pmatrix}, \tag{6.1}$$

$$\Delta\hat{A} = \begin{pmatrix} \omega\Delta\varepsilon/c & 0 \\ 0 & -\frac{c}{\omega}\nabla_t \times \Delta\left(\frac{1}{\varepsilon}\right)\nabla_t \times \end{pmatrix},$$

[1]Typical experimental magnitudes of roughness due to lithography [37, 223] will be even lower than those we study here.

where $\Delta(1/\varepsilon) = -\Delta\varepsilon/[\varepsilon(\varepsilon + \Delta\varepsilon)]$, and

$$\hat{B} \equiv \begin{pmatrix} 0 & -\hat{\mathbf{z}}\times \\ \hat{\mathbf{z}}\times & 0 \end{pmatrix},$$

where ∇_t denotes the transverse (xy) components of ∇. In contrast to quantum mechanics, $\hat{A}$ and $\hat{B}$ are Hermitian (for real/lossless ε and μ) but are not positive definite, permitting complex eigenvalues.

From Bloch's theorem, the eigenstates of the unperturbed system can be written $e^{i\beta z}|\beta\rangle$, where the real part of $\beta \in (-\pi/a, \pi/a]$, and $|\beta\rangle$ is a periodic function of z with period a that satisfies the generalized Hermitian eigenproblem

$$\left(\hat{A} + i\frac{\partial}{\partial z}\hat{B}\right)|\beta\rangle = \beta\hat{B}|\beta\rangle. \tag{6.2}$$

These states satisfy the orthogonality relationship $\langle\beta^*|\hat{B}|\beta'\rangle = 0$ for $\beta \neq \beta'$, where $|\beta^*\rangle$ is the eigenstate with conjugated eigenvalue β^*, and the implicit integral is over one unit cell. (Modes with complex β are evanescent). While a complete basis at constant ω requires the inclusion of a continuum of nonguided states, this continuum can be thought of as the infinite-volume limit of a set of discrete states of a finite volume with conducting boundary conditions. We can thus consider only modes $|n\rangle$ that have discrete eigenvalues β_n and can be normalized such that $\langle m^*|\hat{B}|n\rangle = \delta_{m,n}\eta_n$, with $|\eta_n| = 1$; moreover, $\langle m^*|\hat{B}e^{(-2\pi i/a)\ell z}|n\rangle = 0$ for $\beta_m \neq \beta_n + (2\pi/a)\ell$.

Because the orthonormality condition involves an integral over the unit cell, it is useful to adopt an algebraic trick [216] that introduces a new integration parameter $\tilde{z}$, a shift of the original, unperturbed waveguide. The full problem is then

$$(\hat{A}(z + \tilde{z}) + \Delta\hat{A})|\psi\rangle_{\tilde{z}} = -i\frac{\partial}{\partial z}\hat{B}|\psi\rangle_{\tilde{z}}, \tag{6.3}$$

where $\hat{A}(z + \tilde{z})$ is obtained by sending $\epsilon(x, y, z) \to \epsilon(x, y, z + \tilde{z})$ in equation 6.1. The

solution of Eq. 6.3 can be expanded in terms of the shifted, unperturbed eigenstates:

$$|\psi(z)\rangle_{\tilde{z}} = \sum_n c_n(z,\tilde{z})|n(z+\tilde{z})\rangle e^{i\beta_n z}. \tag{6.4}$$

Since $\hat{A}(z+\tilde{z}+a) = \hat{A}(z+\tilde{z})$, the c_n's can be chosen to be periodic in $\tilde{z}$ and their $\tilde{z}$ dependence expressed as a Fourier series:

$$c_n(z,\tilde{z}) = \sum_\ell c_{n,\ell}(z)e^{-2\pi i\ell\tilde{z}/a}. \tag{6.5}$$

After substituting Eq. 6.4 into Eq. 6.3 and applying a $\tilde{z}$-shifted orthonormality condition, the physical solution is obtained by setting $\tilde{z}$ to zero in Eq. 6.5. After integration by parts and a change of variables, we obtain the final result in terms of the original fields:[2]

$$\left.\frac{dc_m}{dz}\right|_z = i\eta_m^* \sum_{k,n,\ell} c_{n,\ell}(z)e^{i(\beta_n-\beta_m+2\pi(\ell-k)/a)z} \int d\mathbf{x}'\, e^{-2\pi i(\ell-k)z'/a}\frac{\omega}{c}\times \tag{6.6}$$
$$\left[\Delta\varepsilon(\mathbf{x}_t',z)\mathbf{E}_t^{m^*}(\mathbf{x}')^*\cdot\mathbf{E}_t^n(\mathbf{x}') - \Delta\left(\frac{1}{\varepsilon(\mathbf{x}_t',z)}\right)D_z^{m^*}(\mathbf{x}')^* D_z^n(\mathbf{x}')\right],$$

where $\mathbf{E}_t \equiv e^{i\beta_n z}\mathbf{E}_t^n$. Note that the integral is over a primed coordinate $\mathbf{x}' = (\mathbf{x}_t', z')$ that ranges over the unit cell, whereas z is the fixed point along the waveguide axis at which dc_m/dz is evaluated. From Eq. 6.7, it can be seen that the mode coupling depends on the strength of the perturbation at a given z and the weighted average of the squared mode profile over the *entire* unit cell, not just at the disorder location. Assuming for simplicity that the unperturbed waveguide is single-mode, the coupled-mode equations can be integrated to first order to yield the coefficient of the reflected

[2]The result must be modified using techniques discussed in [224] for boundary perturbations with non-TM modes.

mode:

$$c_r(z) \approx i\eta_r^* \sum_k \int dz\, e^{i(2\beta_i - 2\pi k/a)z} \int d\mathbf{x}' e^{2\pi i k z'/a} \frac{\omega}{c} \times \tag{6.7}$$
$$\left(\Delta\varepsilon(\mathbf{x}_t', z)\mathbf{E}_t^r(\mathbf{x}')^* \cdot \mathbf{E}_t^i(\mathbf{x}') - \Delta\left(\frac{1}{\varepsilon(\mathbf{x}_t', z)}\right) D_z^r(\mathbf{x}')^* D_z^i(\mathbf{x}') \right) c_i(0),$$

where i and r label the incident and reflected modes. (Note that a factor of $\sqrt{1/v_g}$ is implicit in the mode normalization [216]).

Eq. 6.8 demonstrates that in the weak-disorder limit, the presence of a photonic band gap in the region surrounding the waveguide has *no effect* on reflection. To first order, only the profile of the guided mode enters the formula for the reflection coefficient, along with the dispersion relation $\beta(\omega)$, the group velocity v_g, and the perturbation $\Delta\epsilon$. As a result, a photonic-crystal waveguide with weak disorder will have the *same* reflection losses as an index-guided waveguide that shares these characteristics, regardless of the guiding mechanism. Moreover, the total transmission will be higher for the photonic-crystal waveguide, since the index-guided waveguide also suffers radiative losses.[3] It is perhaps natural to suppose that reflection losses should be higher for a photonic-crystal waveguide than for an index-guided waveguide, for one could imagine that the suppression of radiative scattering losses by the photonic crystal would redirect light into reflection (as well as in the forward direction). However, our results show that to first order, such redirection does not occur. Because the photonic crystal modifies the local density of states at the scattering site, the total scattered power is lower, and the total reflected power is in fact the same as in a comparable index-guided waveguide.

As a specific illustration of these general results, consider the waveguides shown in Figure 6-1(a). On the left side of the figure is a 2D photonic-crystal (PC) waveguide made by introducing a high-index strip of width w into the center of a missing row of rods [10, 225]. The bulk crystal is composed of a two-dimensional square array of

[3]The lowest order correction to the power transmission is given by $T(z) = 1 - |c_r(z)|^2 - \sum_{m \neq i,r} |c_m(z)|^2$, where the sum over m includes radiative terms calculated in a similar manner to Eq. 6.8.

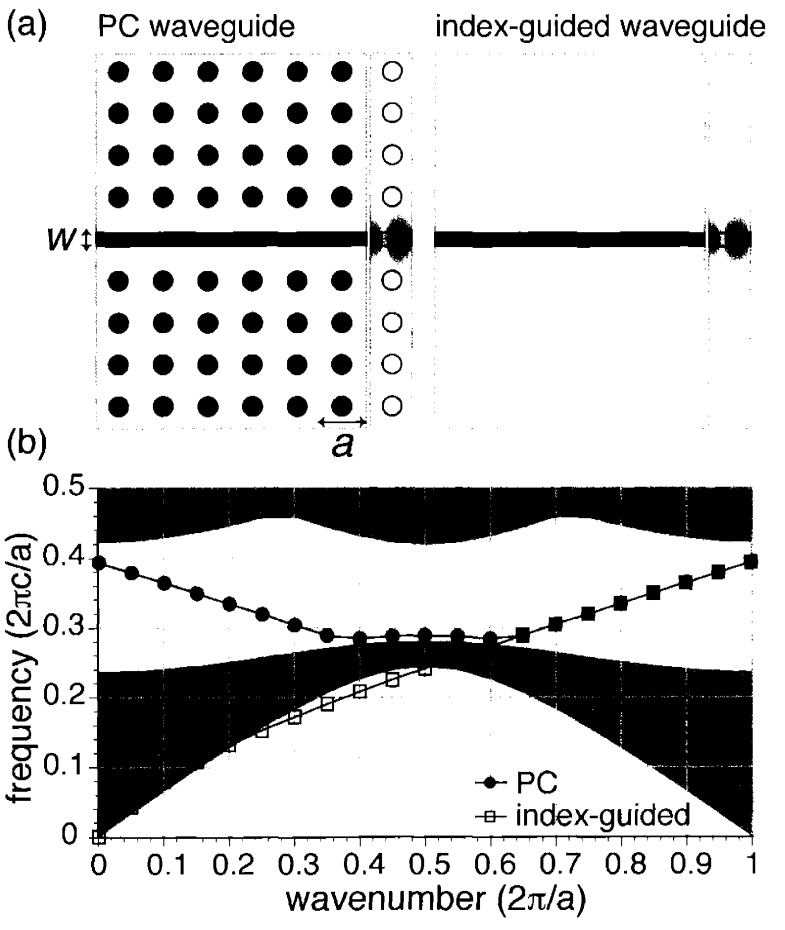

Figure 6-1: (a) Waveguide geometries and corresponding mode profiles for $\omega = 0.31(2\pi c/a)$. Mode profiles show the electric field component perpendicular to the page; red and blue indicate negative and positive values respectively. (b) Band diagram for modes of the two waveguides shown in (a). Shaded regions indicate extended TM states of the bulk 2D photonic crystal.

high-index rods in air. On the right side of the figure is an index-guided waveguide composed of the high-index strip alone. A comparison of these two systems provides a clear demonstration of the effect of a photonic band gap on disorder-induced scattering, because the *only* difference between the two is the presence of the band gap.

Figure 6-1(b) shows the dispersion relations of both structures computed by planewave expansion [98] for rod radius $r = 0.2a$, $w = 0.3a$ and $\varepsilon = 12$. The shaded regions indicate extended TM states of the bulk 2D photonic crystal. Filled,

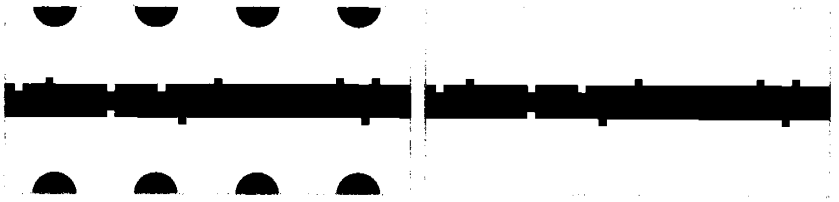

Figure 6-2: Closeup of central waveguide region, showing how identical surface roughness was added to the photonic-crystal and index-guided waveguides.

blue circles show the photonic-crystal waveguide mode (defect mode), which traverses the band gap. Open, red squares show the fundamental mode of the index-guided waveguide. The dispersion relations of both modes coincide for wave vectors greater than $\sim 0.65(2\pi/a)$. In this range, the electric field profile is nearly identical for the two waveguides; Figure 6-1(a) shows the electric field perpendicular to the page for $\omega = 0.31(2\pi c/a)$. Quantitatively, the unit-cell average of $|E_t|^2$ at the waveguide surface is the same to an accuracy of 0.1%. From Eq. 6.8, it is expected that the two waveguides will have nearly identical reflections in the weak-disorder limit.

Surface roughness was added to both the PC and index-guided waveguides, and the resulting reflection and transmission were calculated using 2D, full-vectorial, finite-difference time domain simulations of Maxwell's equations [99]. The computational resolution was 20 grid points/a. Perfectly-matched-layer (PML) boundary regions were used at the edges of the computational cell [104]. Figure 6-2 shows the central waveguide region. For each realization of disorder, the same perturbation was made to both the PC and index-guided waveguides. Along each side of the strip, a random perturbation was made at each grid point, with a probability p of a pixel being added and a probability p of a pixel being removed. No perturbation was made to the rod surfaces. Aside from a slight narrowing of the band gap [179, 180], the effect of such a perturbation should be negligible for weak disorder.[4]

[4]Because the mode is strongly localized in the central strip region, scattering is dominated by roughness along the strip surfaces. The effect of roughness in the bulk can be estimated from the ratio of the average mode intensity at the edge of the nearest rod to that at the side of the strip, which is roughly 0.01. The suppression of the local density of states inside the bulk photonic crystal and the result of averaging over different realizations of bulk disorder should further reduce the strength of the effect.

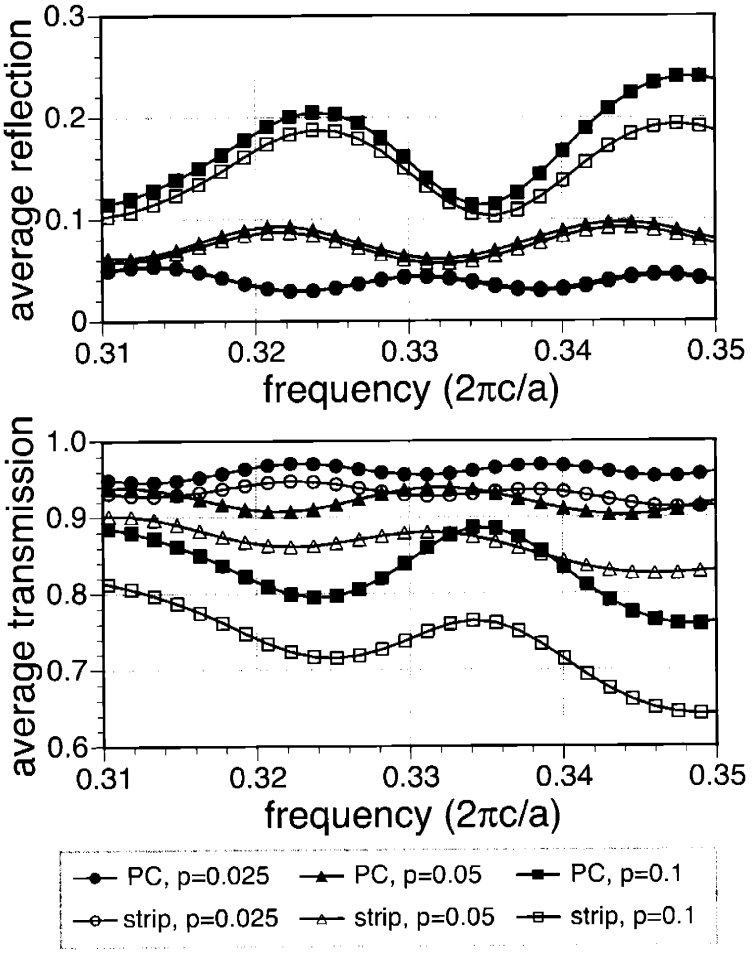

Figure 6-3: Transmission and reflection for a disordered region of length $10a$, averaged over 20 realizations of the disorder.

Figure 6-3 shows reflection and transmission as a function of frequency, where the results are averaged over 20 realizations of the disorder and the length L of the disordered segment of the waveguide is $10a$. For the frequency range shown, the dispersion relations for the PC and index-guided waveguides overlap (see Fig. 6-1). The results are plotted for three values of the disorder probability, p. At the highest value, $p = 0.1$, the reflection in the PC waveguide is higher than that in the strip waveguide by 2-6% due to second-order scattering. As p is decreased, the difference in reflection decreases and is unobservable for $p = 0.025$. For all three values of p, the transmission through the PC waveguide is higher than that through the index-guided waveguide. The oscillations in the frequency spectrum that are visible in both the

average reflection and transmission are due to Fabry-Perot effects arising from the finite length of the disordered region. The period of oscillation corresponds to a length of $\sim 10a$ and was found to scale linearly with L; the magnitude of the oscillations decreases linearly with p.

The average transmission through the PC waveguide decreases more slowly with length than for the index-guided waveguide. For $p = 0.05$, the calculated loss was $\sim 0.04\text{dB}/a$ for the photonic-crystal and $\sim 0.07\text{dB}/a$ for the index-guided waveguide.

While the numerical results we present are for a specific, 2D system, we emphasize that the coupled-mode theory developed here provides a general, semi-analytical framework that can now be used to study the effects of arbitrary disorder in a variety of 3D photonic crystals. Moreover, the physical insight that it provides is applicable for general photonic-crystal waveguides: in the limit of weak disorder, the photonic crystal suppresses radiation loss without redirecting light into reflection. The results should thus be of great interest for the development of low-loss waveguides in high to medium-index contrast systems using photonic crystals with full or partial band gaps. Several avenues present themselves for future study, such as the direct semi-analytical prediction of disorder losses in realistic systems and the development of a generalized coupled-power theory [194] based on Eq. 6.7. The latter can be used to illuminate the effects of long-correlation-length ($\gg a$) disorder, which may cause additional scattering/reflection due to quasi-phase matching, as well as to allow the comparison of photonic-crystal waveguides that do not directly correspond to conventional waveguides.

Chapter 7

Conclusions

Since the initial proposal of photonic band-gap materials in 1987, the field has undergone a rapid expansion, with the prediction and fabrication of 3D crystal structures, the discovery of novel phenomena arising from unique properties of photonic crystals, and the proposal of a number of interesting, practical applications. Experimentally, the area of 2D-periodic, photonic-crystal slab structures is developing rapidly and progress toward functioning, integrated optical devices is well underway. Meanwhile, the fabrication and optical characterization of fully 3D structures continues to challenge existing fabrication techniques and inspire innovations.

Where will the field go next? A number of areas present themselves in which the theorist, in particular, can contribute. The first of these is the continuing identification and prediction of 3D photonic band gap structures and their properties. By working with experimentalists knowledgeable in various fabrication techniques, new structures and methods may be identified to facilitate the design and fabrication of 3D crystals. The work in Chapter 2 on the design of 2D-like defects in 3D crystals fits in with this general theme, for our results simplify the design of optical components in 3D lithographic structures.

Another major theme is the identification of novel phenomena arising in photonic crystals as a result of the high index contrast and strong periodicity of such systems. Photonic crystals provide great flexibility to tailor bulk properties, dispersion relations, and characteristics of defect modes. This flexibility may be exploited to

discover a number of interesting new effects. The work in Chapter 3, which suggests the use of point-defect modes for "meta"-materials properties, the study of slow-light enhancement effects in Chapters 4 and 5, and the reduction of disorder-induced scattering through density-of-states suppression studied in Chapter 6 represent efforts towards this end.

Lastly, the embodiment of practical photonic-crystal devices will require the further development of techniques for design optimization and modeling. We hope that the discussion of figures of merit for tunable time-delay devices in Chapter 5 and the development of a semi-analytical theory for the simulation of arbitrary disorder in photonic crystal waveguides in Chapter 6 will contribute to these goals.

Bibliography

[1] Eli Yablonovitch. Inhibited spontaneous emission in solid-state physics and electronics. *Phys. Rev. Lett.*, 58:2059–2062, May 1987.

[2] Sajeev John. Strong localization of photons in certain disordered dielectric superlattices. *Phys. Rev. Lett.*, 58(23):2486–2489, June 1987.

[3] K. M. Ho, C. T. Chan, and C. M. Soukoulis. Existence of a photonic band gap in periodic dielectric structures. *Phys. Rev. Lett.*, 65(25):3152–3155, December 1990.

[4] E. Yablonovitch, T. J. Gmitter, and K. M. Leung. Photonic band-structure–the face-centered cubic case employing nonspherical atoms. *Phys. Rev. Lett.*, 67(17):2295–2298, October 1991.

[5] John D. Joannopoulos, Robert D. Meade, and Joshua N. Winn. *Photonic Crystals: Molding the Flow of Light.* Princeton Univ. Press, 1995.

[6] Kazuaki Sakoda. *Optical Properties of Photonic Crystals.* Springer, Berlin, 2001.

[7] Eugene Hecht. *Optics.* Addison Wesley, Reading, Mass., fourth edition, 2001.

[8] N. W. Ashcroft and N. D. Mermin. *Solid State Physics.* Holt Saunders, Philadelphia, 1976.

[9] Steven G. Johnson, Shanhui Fan, Pierre R. Villeneuve, J. D. Joannopoulos, and L. A. Kolodziejski. Guided modes in photonic crystal slabs. *Phys. Rev. B*, 60(8):5751–5758, August 1999.

[10] Steven G. Johnson, Pierre R. Villeneuve, Shanhui Fan, and J. D. Joannopoulos. Linear waveguides in photonic-crystal slabs. *Phys. Rev. B*, 62(12):8212–8222, September 2000.

[11] Gershon Kurizki. Two-atom resonant radiative coupling in photonic band structures. *Phys. Rev. A*, 42(4):2915–2924, September 1990.

[12] Sajeev John and Jian Wang. Quantum optics of localized light in a photonic band gap. *Phys. Rev. Lett.*, 43(16):12772–12789, Junc 2000.

[13] Jonathan P. Dowling and Charles M. Bowden. Beat radiation of dipoles near a photonic band edge. *J. Opt. Soc. Am. B*, 10(2):353–355, February 1993.

[14] Shi-Yao Zhu, Yaping Yang, Hong Chen, Hang Zheng, and M. S. Zubairy. Spontaneous radiation and lamb shift in three-dimensional photonic crystals. *Phys. Rev. Lett.*, 84(10):2136–2139, March 2000.

[15] M. Loncar, T. Yoshie, A. Scherer, P. Gogna, and Y. M. Qiu. Low-theshold photonic crystal laser. *Appl. Phys. Lett.*, 81(15):2680–2682, October 2002.

[16] A. A. Erchak, D. J. Ripin, S. Fan, P. Rakich, J. D. Joannopoulos, E. P. Ippen, G. S. Petrich, and L. A. Koldziejski. Enhanced coupling to vertical radiation using a two-dimensional photonic crystal in a semiconductor light-emitting diode. *Appl. Phys. Lett.*, 78(5):563–565, January 2001.

[17] Raffaele Colombelli, Kartik Srinivasan, Mariano Troccoli, Oskar Painter, Clair F. Gmachl, Donald M. Tennant, A. Michael Sergent, Deborah L. Sivco, Alfred Y. Cho, and Federico Capasso. Quantum cascade surface-emitting photonic crystal laser. *Science*, 302:1374–1377, November 2003.

[18] Y. Fink, J. N. Winn, Shanhui Fan, Chiping Chen, J. Michel, J. D. Joannopoulos, and E. L. Thomas. A dielectric omnidirectional reflector. *Science*, 282(5394):1679–1682, November 1998.

[19] M. Notomi. Negative refraction in photonic crystals. *Optical and Quantum Electron.*, 34:133 143, January 2002.

[20] Chiyan Luo, Steven G. Johnson, J. D. Joannopoulos, and J. B. Pendry. All-angle negative refraction without negative effective index. *Phys. Rev. B*, 65:201104(R), May 2002.

[21] C. Y. Luo, S. G. Johnson, and J. D. Joannopoulos. All-angle negative refraction in a three-dimensionally periodic photonic crystal. *Appl. Phys. Lett.*, 81(13):2352–2354, September 2002.

[22] Hideo Kosaka, Takayuki Kawashima, Akihisa Tomita, Masaya Notomi, Toshiaki Tamamura, Takashi Sato, and Shojiro Kawakami. Superprism phenomena in photonic crystals. *Phys. Rev. B*, 58(16):R10096–10099, October 1998.

[23] C. Y. Luo, S. G. Johnson, J. D. Joannopoulos, and J. B. Pendry. Subwavelength imaging in photonic crystals. *Phys. Rev. B*, 68(4):045115, July 2003.

[24] E. Cubukcu, K. Aydin, E. Ozbay, S. Foteinopolou, and C. M. Soukoulis. Subwavelength resolution in a two-dimensional photonic-crystal-based superlens. *Phys. Rev. Lett.*, 91(20):207401, November 2003.

[25] Hideo Kosaka, Takayuki Kawashima, Akihisa Tomita, Takashi Sato, and Shojiro Kawakami. Photonic-crystal spot-size converter. *Appl. Phys. Lett.*, 76(3):268–270, January 2000.

[26] Chiyan Luo, Mihai Ibanescu, Steven G. Johnson, and J. D. Joannopoulos. Cerenkov radiation in photonic crystals. *Science*, 299(5605):368–371, January 2003.

[27] Robert D. Meade, A. Devenyi, J. D. Joannopoulos, O. L. Alerhand, D. A. Smith, and K. Kash. Novel applications of photonic band gap materials: Low-loss bends and high Q cavities. *J. Appl. Phys.*, 75(9):4753 -4755, May 1994.

[28] J. Vuckovic, M. Loncar, H. Mabuchi, and A. Scherer. Optimization of the Q factor in photonic crystal microcavities. *IEEE J. Quantum Electron.*, 38(7):850–856, July 2002.

[29] Shanhui Fan, Pierre R. Villeneuve, J. D. Joannopoulos, and H. A. Haus. Channel drop tunneling through localized states. *Phys. Rev. Lett.*, 80(5):960-963, February 1998.

[30] Shanhui Fan, Pierre R. Villeneuve, J. D. Joannopoulos, M. J. Khan, C. Manolatou, and H. A. Haus. Theoretical analysis of channel drop tunneling processes. *Phys. Rev. B.*, 59(24):15822–15892, June 1999.

[31] O. Painter, R. K. Lee, A. Scherer, A. Yariv, J. D. O'Brien, P. D. Dapkus, and I. Kim. Two-dimensional photonic band-gap defect mode laser. *Science*, 284(5421):1819–1821, June 1999.

[32] Jelena Vučković, Marco Lončar, Hideo Mabuchi, and Axel Scherer. Design of photonic crystal microcavities for cavity qed. *Phys. Rev. E*, 65:016608, 2002.

[33] Attila Mekis, J. C. Chen, I. Kurland, Shanhui Fan, Pierre R. Villeneuve, and J. D. Joannopoulos. High transmission through sharp bends in photonic crystal waveguides. *Phys. Rev. Lett.*, 77(18):3787–3790, October 1996.

[34] Shanhui Fan, Steven G. Johnson, J. D. Joannopoulos, C. Manolatou, and H. A. Haus. Waveguide branches in photonic crystals. *J. Opt. Soc. Am. B*, 18(2):162–165, February 2001.

[35] Steven G. Johnson, C. Manolatau, Shanhui Fan, Pierre R. Villeneuve, and J. D. Joannopoulos. Elimination of cross talk in waveguide intersections. *Opt. Lett.*, 23(23):1855-1857, December 1998.

[36] J. D. Joannopoulos, Pierre R. Villeneuve, and Shanhui Fan. Photonic crystals: putting a new twist on light. *Nature*, 386:143–149, March 1997.

[37] Thomas F. Krauss. Planar photonic crystal waveguide devices for integrated optics. *Physica Status Solidi (a)*, 197(3):688–702, June 2003.

[38] R. E. Slusher and B. J. Eggleton. *Nonlinear Photonic Crystals*. Springer, Berlin, 2003.

[39] C. M. Bowden and A. M. Zheltikov. Nonlinear optics of photonic crystals. *J. Opt. Soc. Am. B*, 19(9), September 2002.

[40] Serge F. Mingaleev and Yuri S. Kivshar. Self-trapping and stable localized modes in nonlinear photonic crystals. *Phys. Rev. Lett.*, 86(24):5474–5477, June 2001.

[41] Marin Soljačić, Chiyan Luo, J. D. Joannopoulos, and Shanhui Fan. Nonlinear photonic crystal microdevices for optical integration. *Opt. Lett.*, 28(8):637–639, April 2003.

[42] Shayan Mookherjea and Amnon Yariv. Second-harmonic generation with pulses in a coupled-resonator optical waveguide. *Phys. Rev. E*, 65:026607, January 2002.

[43] N. G. R. Broderick, G. W. Ross, H. L. Offerhaus, D. J. Richardson, and D. C. Hanna. Hexagonally poled lithium niobate: a two-dimensional nonlinear photonic crystal. *Phys. Rev. Lett.*, 84(19):4345–4348, May 2000.

[44] Marin Soljačić and J. D. Joannopoulos. Enhancement of nonlinear effects using photonic crystals. *Nature Materials*, 3:211–19, April 2004.

[45] M. Ibanescu, Y. Fink, S. Fan, E. L. Thomas, and J. D. Joannopoulos. An all-dielectric coaxial waveguide. *Science*, 289:415–419, 2000.

[46] Mihai Ibanescu, Steven G. Johnson, Marin Soljačić, J. D. Joannopoulos, Yoel Fink, Ori Weisberg, Torkel D. Engeness, Steven A. Jacobs, and M. Skorobogatiy. Analysis of mode structure in OmniGuide fibers. *Phys. Rev. B*, 2002. Submitted for publication.

[47] J. C. Knight, J. Broeng, T. A. Birks, and P. St.-J. Russell. Photonic band gap guidance in optical fibers. *Science*, 282:1476–1478, 1998.

[48] R. F. Cregan, B. J. Mangan, J. C. Knight, T. A. Birks, P. St.-J. Russell, and P. J. Roberts. Single-mode photonic band gap guidance of light in air. *Science*, 285:1537–1539, September 1999.

[49] Steven G. Johnson, Mihai Ibanescu, M. Skorobogatiy, Ori Weisberg, Torkel D. Engeness, Marin Soljačić, Steven A. Jacobs, J. D. Joannopoulos, and Yoel Fink. Low-loss asymptotically single-mode propagation in large-core OmniGuide fibers. *Opt. Express*, 9(13):748–779, 2001.

[50] Burak Temelkuran, Shandon D. Hart, Gilles Benoit, John D. Joannopoulos, and Yoel Fink. Wavelength-scalable hollow optical fibres with large photonic band gaps for co_2 laser transmission. *Nature*, 420:650–653, December 2002.

[51] Charlene M. Smith, Natesan Venkataraman, Michael T. Gallagher, Dirk Müller, James A. West, Nicholas F. Borrelli, Douglas C. Allan, and Karl W. Koch. Low-loss hollow-core silica/air photonic bandgap fibre. *Nature*, 424:657 659, August 2003.

[52] J. C. Knight, T. A. Birks, P. St. J. Russell, and D. M. Atkin. All-silica single-mode optical fiber with photonic crystal cladding. *Opt. Lett.*, 21(19):1547–9, October 1996.

[53] William J. Wadsworth, Arturo Ortigosa-Blanch, Jonathan C. Knight, Tim A. Birks, T.-P. Martin Man, and Phillip St. J. Russell. Supercontinuum generation in photonic crystal fibers and optical fiber tapers: a novel light source. *J. Opt. Soc. Am. B*, 19(9):2148–2155, September 2002.

[54] Kazi S. Abedin, Juliet T. Gopinath, Erich P. Ippen, Charles E. Kerbage, Robert S. Windeler, and Benjamin J. Eggleton. Highly nondegenerate femtosecond four-wave mixing in tapered microstructure fiber. *Appl. Phys. Lett.*, 81(8):1384–1386, August 2002.

[55] T. A. Birks, J. C. Knight, and P. St. J. Russell. Endlessly single-mode photonic crystal fiber. *Opt. Lett.*, 22(13):961 963, July 1997.

[56] Kazunori Suzuki, Hirokazu Kubota, Satoki Kawanishi, Masatoshi Tanaka, and Moriyuki Fujita. Optical prperties of a low-loss polarization-maintaining photnic crystal fiber. *Opt. Express*, 9(13):676–680, December 2001.

[57] J. C. Knight, T. A. Birks, R. F. Cregan, P. St. J. Russel, and P. D. de Sandro. Large mode area photonic crystal fibre. *Elec. Lett.*, 34(13):1347 1348, June 1998.

[58] C. M. Soukoulis. The history and a review of the modelling and fabrication of photonic crystals. *Nanotechnology*, 13:420–423, May 2002.

[59] E. Ozbay, E. Michel, G. Tuttle, R. Biswas, M. Sigalas, and K. M. Ho. Micromachined millimeter-wave photonic band-gap crystals. *Appl. Phys. Lett.*, 64(16):2059–2061, April 1994.

[60] M. Deopura, C. K. Ullal, B. Temelkuran, and Y. Fink. Dielectric omnidirectional visible reflector. *Opt. Lett.*, 26(15):1197–1199, August 2001.

[61] E. Chow, S. Y. Lin, S. G. Johnson, P. B. Villenueve, J. D. Joannopoulos, J. R. Wendt, G. A. Vawter, W. Zubrzycki, H. Hou, and A. Alleman. Three-dimensional control of light in a two-dimensional photonic crystal slab. *Nature*, 407(6807):983–986, October 2000.

[62] S. Y. Lin, E. Chow, S. G. Johnson, and J. D. Joannopoulos. Demonstration of highly efficient waveguiding in a photonic crystal slab at the 1.5-μm wavelength. *Opt. Lett.*, 25(17):1297–1299, September 2000.

[63] J. S. Foresi, P. R. Villeneuve, J. Ferrera, E. R. Thoen, G. Steinmeyer, S. Fan, J. D. Joannopoulos, L. C. Kimerling, H. I. Smith, and E. P. Ippen. Photonic-bandgap microcavities in optical waveguides. *Nature*, 390:143–145, November 1997.

[64] T. Yoshie, J. Vuckovic, A. Scherer, Hao Chen, and D. Deppe. High quality two-dimensional photonic crystal slab cavities. *Appl. Phys. Lett.*, 79(26):4289–4291, December 2001.

[65] M. Lončar, T. Doll, J. Vučković, and A. Scherer. Design and fabrication of silicon photonic crystal optical waveguides. *J. Lightwave Technology*, 18(10):1402 1411, October 2000.

[66] P. Bettotti, L. Dal Negro, Z. Gaburro, L. Pavesi, A. Lui, M. Galli, M. Patrini, and F. Marabelli. P-type macroporous silicon for two-dimensional photonic crystals. *J. Appl. Phys.*, 92(12):6966–6972, December 2002.

[67] K. M. Ho, C. T. Chan, C. M. Soukoulis, R. Viswas, and M. Sigalas. Photonic band-gaps in 3-dimensions-new layer-by-layer periodic structures. *Solid State Communications*, 89(5):413 416, February 1994.

[68] S. Y. Lin, J. G. Fleming, D. L. Hetherington, B. K. Smith, R. Biswas, K. M. Ho, M. M. Sigalas, W. Zubrzycki, S. R. Kurtz, and Jim Bur. A three-dimensional photonic crystal operating at infrared wavelengths. *Nature*, 394:251–253, July 1998.

[69] Susumu Noda, Katsuhiro Tomoda, Noritsugu Yamamoto, and Alongkarn Chutinan. Full three-dimensional photonic bandgap crystals at near-infrared wavelengths. *Science*, 289:604–606, July 2000.

[70] Minghao Qi, Elefterios Lidorikis, Peter T. Rakich, Steven G. Johnson, J. D. Joannopoulos, Erich P. Ippen, and Henry I. Smith. A three-dimensional optical photonic crystal with designed point defects. *Nature*, 2004. In press.

[71] Florencio García-Santamaria, Hideki T. Miyazaki, Alfonso Urquía, Marta Ibisate, Manuel Belmonte, Norio Shinya, Francisco Meseguer, and Cefe López. Nanorobotic manipulation of microspheres for on-chip diamond architectures. *Adv. Mater.*, 14(16):1144–1147, August 2002.

[72] F. García-Santamaría, C. López, F. Meseguer, F. López-Tejeira, J. Sánchez-Dehesa, and H. T. Miyazaki. Opal-like photonic crystal with diamond lattice. *Appl. Phys. Lett.*, 79(15):2309–2311, October 2001.

[73] Kanna Aoki, Hideki T. Miyazaki, Hideki Hirayama, Kyoji Inoshita, Toshihiko Baba, Norio Shinya, and Yoshinobu Aoyagi. Three-dimensional photonic crystals for optical wavelengths assembled by micromanipulation. *Appl. Phys. Lett.*, 81(17):3122 3124, October 2002.

[74] Kanna Aoki, Hideki Hirayama, Kyoji Inoshita, Toshihiko Baba, Kazuaki Sakoda, Norio Shinya, and Yoshinobu Aoyagi. Microassembly of semiconductor three-dimensional photonic crystals. *Nature Materials*, 2:117–121, February 2003.

[75] Satoshi Kawata, Hong-Bo Sun, Tomokazu Tanaka, and Kenji Takada. Finer features for functional microdevices. *Nature*, 412:697–698, August 2001.

[76] Brian H. Cumpston, Sundaravel P. Ananthavel, Stephen Barlow, Daniel L. Dyer, Jeffrey E. Ehrlich, Lael L. Erskine, Ahmed A. Heikal, Stephen M. Kuebler, I.-Y. Sandy Lee, Dianne McCord-Maughon, Jinqui Qin, Harald Röckel, Mariacristina Rumi, Xiang-Li Wu, Seth R. Marder, and Joseph W. Perry. Two-photon polymerization initiators for three-dimensional optical data storage and microfabrication. *Nature*, 398:51–54, March 1999.

[77] M. Campbell, D. N. Sharp, M. T. Harrison, R. G. Denning, and A. J. Turberfield. Fabrication of photonic crystals for the visible spectrum by holographic lithography. *Nature*, 404:53–56, March 2000.

[78] D. N. Sharp, M. Campbell, E. R. Dedman, M. T. Harrison, R. G. Denning, and A. J. Turberfield. Photonic crystals for the visible spectrum by holographic lithography. *Optical and Quantum Electron.*, 34:3–12, 2002.

[79] D. N. Sharp, A. J. Turberfield, and R. G. Denning. Holographic photonic crystals with diamond symmetry. *Phys. Rev. B*, 68:205102, November 2003.

[80] Yurii A. Vlasov, Xiang-Zheng Bo, James C. Sturm, and David J. Norris. On-chip natural assembly of silicon photonic band gap crystals. *Nature*, 414:289–293, November 2001.

[81] Wonmok Lee, Stephanie A. Pruzinsky, and Paul V. Braun. Multi-photon polymerization of waveguide structures within three-dimensional photonic crystals. *Advanced Materials*, 14(4):271–274, February 2002.

[82] Yoel Fink, Augustine M. Urbas, Moungi G. Bawendi, John D. Joannopoulos, and Edwin L. Thomas. Block copolymers as photonic bandgap materials. *J. Lightwave Tech.*, 17(11):1963 1969, November 1999.

[83] Alexander C. Edrington, Augustine M. Urbas, Peter DeRege, Cinti X. Chen, Timothy M. Swager, Nikos Hadjichristidis, Maria Xenidou, Lewis J. Fetters, John D. Joannopoulos, Yoel Fink, and Edwin L. Thomas. Polymer-based photonic crystals. *Adv. Mater.*, 13(6):421–425, March 2001.

[84] Augustine Urbas, Yoel Fink, and Edwin L. Thomas. One-dimensionally periodic dielectric reflectors from self-assembled block copolymer-homopolymer blends. *Macromolecules*, 32(14):4748–4750, 1999.

[85] A. Urbas, R. Sharp, Y. Fink, E. L. Thomas, M. Xenidou, and L. J. Fetters. Tunable block copolymer/homopolymer photonic crystals. *Adv. Mater.*, 12(11):812–814, June 2000.

[86] Y. Fink, D. J. Ripin, S. Fan, C. Chen, J. D. Joannopoulos, and E. L. Thomas. Guiding optical light in air using an all-dielectric structure. *J. Lightwave Tech.*, 17:2039–2041, 1999.

[87] Ovidiu Toader and Sajeev John. Proposed square spiral microfabrication architecture for large three-dimensional photonic band gap crystals. *Science*, 292:1133–1135, May 2001.

[88] Scott R. Kennedy, Michael J. Brett, Ovidiu Toader, and Sajeev John. Fabrication of tetragonal square spiral photonic crystals. *Nano Letters*, 2(1):59–62, 2002.

[89] Shojiro Kawakami, Takayuki Kawashima, and Sato Takashi. Mechanism of shape formation of three-dimensional nanostructures by bias sputtering. *Appl. Phys. Lett.*, 74(3):463–465, January 1999.

[90] Eiichi Kuramochi, Masaya Notomi, Toshiaki Tamamura, Takayuki Kawashima, Shojiro Kawakami, Jun-ichi Takahashi, and Chiharu Takahashi. Drilled alternating-layer structure for three-dimensional photonic crystals with a full band gap. *J. Vac. Sci. Technol. B*, 18(6):3510–3513, Nov/Dec 2000.

[91] Y. Ohtera, T. Kawashima, Y. Sakai, T. Sato, I. Yokohama, A. Ozawa, and S. Kawakami. Photonic crystal waveguides utilizing a modulated lattice structure. *Opt. Lett.*, 27(24):2158–2160, December 2002.

[92] Eiichi Kuramochi, Masaya Notomi, Itaru Yokohama, Jun-ichi Takahashi, Chiharu Takahashi, Takayuki Kawashima, and Shojiro Kawakami. Transmission characterization of drilled alternating-layer three-dimensional photonic crystals. *J. Appl. Phys.*, 93(11):8848–8851, June 2003.

[93] A. Chelnokov, K. Wang, S. Rowson, P. Garoche, and J.-M. Lourtioz. Near-infrared Yablonovite-like photonic crystals by focused-ion-beam etching of macroporous silicon. *Appl. Phys. Lett.*, 77(19):2943–2945, November 2000.

[94] C. Cuisin, A. Chelnokov, D. Decanini, D. Peyrade, Y. Chen, and J. M. Lourioz. Sub-micrometre dielectric and metallic yablonovite strucutres fabricated from resist templates. *Optical and Quantum Electron.*, 34:13–26, 2002.

[95] F. Romanato, D. Cojoc, and E. Di Fabrizio. X-ray and electron-beam lithography of three-dimensional array structures for photonics. *J. Vac. Sci. Technol. B*, 21(6):2912 2916, Nov/Dec 2003.

[96] Ovidiu Toader, Mona Verciu, and Sajeev John. Photonic band gaps based on tetragonal lattices of slanted pores. *Phys. Rev. Lett.*, 90(23):233901, June 2003.

[97] Shandon D. Hart, Garry R. Maskaly, Burak Temelkuran, Peter H. Prideaux, John D. Joannopoulos, and Yoel Fink. External reflection from omnidirectional dielectric mirror fibers. *Science*, 296:510–513, April 2002.

[98] Steven G. Johnson and J. D. Joannopoulos. Block-iterative frequency-domain methods for Maxwell's equations in a planewave basis. *Opt. Express*, 8(3):173 190, January 2001.

[99] Karl S. Kunz and Raymond J. Luebbers. *The Finite-Difference Time-Domain Method for Electromagnetics.* CRC Press, Boca Raton, 1993.

[100] R. Scarmozzino, A. Gopinath, R. Pregla, and S. Helfert. Numerical techniques for modeling guided-wave photonic devices. *IEEE J. Sel. Top. Quant. Elect.*, 6(1):150 -162, January/February 2000.

[101] Rose M. Joseph and Allen Taflove. FDTD Maxwell's equations models for nonlinear electrodynamics and optics. *IEEE Transactions on Antennas and Propagation*, 45(3):364 -374, March 1997.

[102] Jeffrey L. Young and Ronald O. Nelson. A summary and systematic analysis of fdtd algorithms for linearly dispersive media. *IEEE Antennas and Propagation Magazine*, 43(1):61–77, February 2001.

[103] Jean-Paul Bérenger. A perfectly matched layer for the absorption of electromagnetic waves. *J. Comput. Phys.*, 114(1):185–200, 1994.

[104] J. C. Chen and K. Li. Quartic perfectly matched layers for dielectric waveguides and gratings. *Microwave and Optical Technology Letters*, 10(6):319–323, December 1995.

[105] Masanori Koshiba, Yasuhide Tsuji, and Satoru Sasaki. High-performance absorbing boundary conditions for photonic crystal waveguide simulations. *IEEE Microwave and Wireless Components Letters*, 11(4):152–154, April 2001.

[106] G. Sztefka and H. P. Nolting. Bidirectional eigenmode propagation for large refractive index steps. *IEEE Photon. Technol. Lett.*, 5(5):554–557, May 1993.

[107] P. M. Bell, J. B. Pendry, L. M. Moreno, and A. J. Ward. A program for calculating photonic band structures and transmission coefficients of complex structures. *Comput. Phys. Commun.*, 85:306 322, 1995.

[108] J. B. Pendry. Photonic band structures. *J. Mod. Opt.*, 41(2):209–229, February 1994.

[109] J. Willems, J. Haes, and R. Baets. The bidirectional mode expansion method for two dimensional waveguides. *Optical and Quantum Electron.*, 27(10):995–1007, 1995.

[110] Peter Bienstman and R. Baets. Optical modelling of photonic crystals and VCSELs using eigenmode expansion and perfectly matched layers. *Optical and Quantum Electron.*, 33(4–5):327–341, 2001.

[111] Zhi-Yuan Li and Lan-Lan Lin. Photonic band structures solved by a plane-wave-based transfer-matrix method. *Phys. Rev. E*, 67:046607, April 2003.

[112] Pochi Yeh. *Optical Waves in Layered Media.* Wiley, New York, 1988.

[113] G. Tayeb and D. Maystre. Rigorous theoretical study of finite-size two-dimensional photonic crystals doped by microcavities. *J. Opt. Soc. Am. A*, 14(12):3323–3332, December 1997.

[114] F. J. García de Abajo. Multiple scattering of radiation in clusters of dielectrics. *Phys. Rev. B*, 60(8):6086–6102, August 1999.

[115] T. Ochiai and J. Sánchez-Dehesa. Localized defect modes in finite metallic two-dimensional photonic crystals. *Phys. Rev. B*, 65:245111, June 2002.

[116] Alon Ludwig and Yehuda Leviatan. Analysis of bandgap characteristics of two-dimensional periodic structures by using the source-model technique. *J. Opt. Soc. Am. A*, 20(8):1553–1562, August 2003.

[117] D. N. Atkin, P. St. J. Russell, T. A. Birks, and P. J. Roberts. Photonic band structure of guided Bloch modes in high index films fully etched through with periodic microstructure. *Journal of Modern Optics*, 43(5):1035–1054, May 1996.

[118] T. F. Krauss, R. M. De La Rue, and S. Brand. Two-dimensional photonic-bandgap structures operating at near-infrared wavelengths. *Nature*, 383:6999 - 6702, October 1996.

[119] D. Labilloy, H. Benisty, C. Weisbuch, T. F. Krauss, R. M. De La Rue, R. Bardinal, V. a nd Houdré, U. Oesterle, D. Cassagne, and C. Jouanin. Quantitative measurement of transmission, reflection, and diffraction of two-dimensional photonic band gap structures at near-infrared wavelengths. *Phys. Rev. Lett.*, 79(21):4147–4150, November 1997.

[120] S. Kuchinsky, D. C. Allan, N. F. Borrelli, and J.-C. Cotteverte. 3D localization in a channel waveguide in a photonic crystal with 2D periodicity. *Opt. Commun.*, 175(1–3):147–152, February 2000.

[121] Han-Youl Ryu, Jeong-Ki Hwang, and Yong-Hee Lee. Conditions of single guided mode in two-dimensional triangular photonic crystal slab waveguides. *J. Appl. Phys.*, 88(9):4941 4946, November 2000.

[122] T. Søndergaard, A. Bjarklev, M. Kristensen, J. Erland, and J. Broeng. Designing finite-height two-dimensional photonic crystal waveguides. *Appl. Phys. Lett.*, 77(6):785–787, August 2000.

[123] Alongkarn Chutinan and Susumu Noda. Waveguides and waveguide bends in two-dimensional photonic crystal slabs. *Phys. Rev. B*, 62(7):4488 4492, August 2000.

[124] O. Painter, J. Vučković, and A. Scherer. Defect modes of a two-dimensional photonic crystal in an optically thin dielectric slab. *J. Opt. Soc. Am. B*, 16(2):275–285, 1999.

[125] R. K. Lee, O. Painter, B. Kitzke, A. Scherer, and A. Yariv. Emission properties of a defect cavity in a two-dimensional photonic bandgap crystal slab. *J. Opt. Soc. Am. B*, 17(4):629--633, April 2000.

[126] C. T. Chan, S. Datta, K. M. Ho, and C. M. Soukoulis. A7 structure– a family of photonic crystals. *Phys. Rev. B*, 50(3):1988–1991, July 1994.

[127] B. T. Holland, C. F. Blanford, and A. Stein. Synthesis of macroporous minerals with highly ordered three-dimensional arrays of spheroidal voids. *Science*, 281:538-540, July 1998.

[128] J. E. G. J. Wijnhoven and W. L. Vos. Preparation of photonic crystals made of air spheres in titania. *Science*, 281:802–804, July 1998.

[129] K. Busch and S. John. Photonic band gap formation in certain self-organizing systems. *Phys. Rev. E*, 58(3):3896–3908, September 1998.

[130] E. Ozbay, A. Abeyta, G. Tuttle, M. Tringides, R. Biswas, C. T. Chan, C. M. Soukoulis, and K. M. Ho. Measurement of a 3-dimensional photonic band-gap in a crystal-structure made of dielectric rods. *Phys. Rev. B*, 50(3):1945–1948, July 1994.

[131] Alongkarn Chutinan and Susumu Noda. Highly confined waveguides and waveguide bends in three-dimensional crystal. *Appl. Phys. Lett.*, 75(24):3739–3741, December 1999.

[132] K. M. Leung. Diamondlike photonic band-gap crystal with a sizable band gap. *Phys. Rev. B*, 56:3517 3519, August 1997.

[133] S. Fan, P. R. Villeneuve, R. Meade, and J. D. Joannopoulos. Design of three-dimensional photonic crystals at submicron lengthscales. *Appl. Phys. Lett.*, 65(11):1466–1468, September 1994.

[134] Steven G. Johnson and J. D. Joannopoulos. Three-dimensionally periodic dielectric layered structure with omnidirectional photonic band gap. *Appl. Phys. Lett.*, 77(22):3490 3492, November 2000.

[135] E. Lidorikis, M. L. Povinelli, S. G. Johnson, and J. D. Joannopoulos. Polarization-independent linear waveguides in 3D photonic crystals. *Phys. Rev. Lett.*, 91(2):023092, July 2003.

[136] David Roundy and John Joannopoulos. Photonic crystal structure with square symmetry within each layer and a three-dimensional band gap. *Appl. Phys. Lett.*, 82(22):3835- 3837, June 2003.

[137] Alongkarn Chutinan, Sajeev John, and Ovidiu Toader. Diffractionless flow of light in all-optical microchips. *Phys. Rev. Lett.*, 90:123901, March 2003.

[138] J. B. Pendry. Negative refraction makes a perfect lens. *Phys. Rev. Lett.*, 85(18):3966–3969, October 2000.

[139] R. A. Shelby, D. R. Smith, and S. Schultz. Experimental verification of a negative index of refraction. *Science*, 292(5514):77 79, April 2001.

[140] Stephen O'Brien and John B. Pendry. Photonic band-gap effects and magnetic activity in dielectric composites. *J. Phys.: Condens. Matter*, 14(15):4035, April 2002.

[141] V. G. Veselago. The electrodynamics of substances with simultaneously negative values of ϵ and μ. *Soviet Physics USPEKHI*, 10:509, 1968.

[142] D. R. Smith, Wille J. Padilla, D. C. Vier, S. C. Nemat-Nasser, and S. Schultz. Composite medium with simultaneously negative permeability and permittivity. *Phys. Rev. Lett.*, 84(18):4184–4187, May 2000.

[143] D. R. Smith, D. C. Vier, N. Kroll, and S. Schultz. Direct calculation of permeability and permittivity for a left-handed material. *Appl. Phys. Lett.*, 77(14):2246–2248, October 2000.

[144] R. A. Shelby, D. R. Smith, and S. Schultz. Experimental verification of a negative index of refraction. *Science*, 292:77–79, April 2001.

[145] M. Notomi. Theory of light propagation in strongly modulated photonic crystals: Refractionlike behavior in the vicinity of the photonic band gap. *Phys. Rev. B*, 62(16):10696–10705, October 2000.

[146] E. Cubukcu, K. Aydin, E. Ozbay, S. Foteinopoulou, and C. M. Soukoulis. Negative refraction by photonic crystals. *Nature*, 423(6940):604–605, June 2003.

[147] Gennady Shvets. Photonic approach to making a material with a negative index of refraction. *Phys. Rev. B*, 67:035109, January 2003.

[148] D. R. Smith and D. Schurig. Electromagnetic wave propagation in media with indefinite permittivity and permeability tensors. *Phys. Rev. Lett.*, 90(7):077405, February 2003.

[149] A. Grbic and G. V. Eleftheriades. Negative refraction, growing evanescent waves, and sub-diffraction imaging in loaded transmission-line metamaterials. *IEEE Transactions on Microwave Theory*, 51(12):2297–2305, December 2003.

[150] Nicholas Fang and Xiang Zhang. Imaging properties of a metamaterials superlens. *Appl. Phys. Lett.*, 82(2):161 -163, January 2002.

[151] Kerwyn Casey Huang, M. L. Povinelli, and J.D. Joannopoulos. Negative effective permeability in polaritonic photonic crystals. In review, 2004.

[152] A. Yariv, Y. Xu, R. K. Lee, and A. Scherer. Coupled-resonator optical waveguide: a proposal and analysis. *Opt. Lett.*, 24:711 713, 1999.

[153] M. Bayindir, B. Temelkuran, and E. Ozbay. Tight-binding description of the coupled defect modes in three-dimensional photonic crystals. *Phys. Rev. Lett.*, 84(10):2140 -2143, March 2000.

[154] N. Notomi, K. Yamada, A. Shinya, J. Takahashi, C. Takahashi, and I. Yokohama. Extremely large group-velocity dispersion of line-defect waveguides in photonic crystal slabs. *Phys. Rev. Lett.*, 87(25):253902, December 2001.

[155] Satoshi Nishikawa, Sheng Lan, Naoki Ikeda, Yoshimasa Sugimoto, Hiroshi Ishikawa, and Kiyoshi Asakawa. Optical characterization of photonic crystal delay lines based on one-dimensional coupled defects. *Opt. Lett.*, 27(23):2079–2081, December 2004.

[156] M. Soljačić, S. G. Johnson, Shanhui Fan, Mihai Ibanescu, Erich Ippen, and J. D. Joannopoulos. Photonic-crystal slow-light enhancement of nonlinear phase sensitivity. *J. Opt. Soc. Am. B*, 19(9):2052–2059, September 2002.

[157] J. P. Dowling, M. Scalora, M. J. Bloemer, and C. M. Bowden. The photonic band edge laser: a new approach to gain enhancement. *J. Appl. Phys.*, 75:1896–1899, 1994.

[158] Lucia Florescu, Kurt Busch, and Sajeev John. Semiclassical theory of lasing in photonic crystals. *J. Opt. Soc. Am. B*, 19(9):2215–2223, September 2002. See also references therein.

[159] J. G. Fleming, S. Y. Lin, I. El-Kady, R. Biswas, and K. M. Ho. All-metallic three-dimensional photonic crystals with a large infrared band gap. *Nature*, 417:52–55, May 2002.

[160] B. E. A. Saleh and M. C. Teich. *Fundamentals of Photonics.* Wiley, New York, 1991.

[161] P. Meystre, E. M. Wright, J. D. McCullen, and E. Vignes. Theory of radiation-pressure-driven interferometers. *J. Opt. Soc. Am. B*, 2(11):1830–1840, November 1985.

[162] C. Fabre, M. Pinard, S. Bourzeix, A. Heidmann, E. Giacobino, and S. Reynaud. Quantum-noise reduction using a cavity with a movable mirror. *Phys. Rev. A*, 49(2):1337–1343, February 1994.

[163] S. Mancini, V. I. Man'ko, and P. Tombesi. Ponderomotive control of quantum macroscopic coherence. *Phys. Rev. A*, 55(4):3042–3050, April 1997.

[164] David Vitali, Stefano Mancini, Luciano Ribichini, and Paolo Tombesi. Macroscopic mechanical oscillators at the quantum limit through optomechanical cooling. *J. Opt. Soc. Am. B*, 20(5):1054–1065, May 2003. and references therein.

[165] S. Bose, K. Jacobs, and P. L. Knight. Scheme to probe the decoherence of a macroscopic object. *Phys. Rev. A*, 59(5):3204–3210, May 1999.

[166] A. D. Armour, M. P. Blencowe, and K. C. Schwab. Entanglement and decoherence of a micromechanical resonator via coupling to a Cooper-pair box. *Phys. Rev. Lett.*, 88(14):148301, April 2002.

[167] R. Ramaswami and K. N. Sivarajan. *Optical Networks: A Practical Perspective.* Academic Press, London, 1998.

[168] Lene Vestergaard Hau, S. E. Harris, Zachary Dutton, and Cyrus H. Behroozi. Light speed reduction to 17 metres per second in an ultracold atomic gas. *Nature*, 397(6720):594–598, February 1999.

[169] Kash M. M., V. A. Sautenkov, A. S. Zibrov, L. Hollverg, G. R. Welch, M. D. Lukin, Y. Rostovtsev, E. S. Fry, and M. O. Scully. Ultraslow group velocity and enhanced nonlinear optical effects in a coherently driven hot atomic gas. *Phys. Rev. Lett.*, 82(26):5229–5232, June 1999.

[170] D. Budker, D. F. Kimball, S. M. Rochester, and V. V. Yashchuk. Nonlinear magneto-optics and reduced group velocity of light in atomic vapor with slow ground state relaxation. *Phys. Rev. Lett.*, 83(9):1767–1770, August 1999.

[171] Chien Liu, Zachary Dutton, Cyrus H. Behroozi, and Lene Vestergaard Hau. Observation of coherent optical information storage in an atomic medium using halted light pulses. *Nature*, 409(6819):490–493, January 2001.

[172] M. D. Lukin and A. Imamoğlu. Controlling photons using electromagnetically induced transparency. *Nature*, 413(6853):273–276, September 2001.

[173] G. Lenz, B. J. Eggleton, C. K. Madsen, and R. E. Slusher. Optical delay lines based on optical filters. *IEEE J. Quantum Electron.*, 37(4):525–532, April 2001.

[174] Zheng Wang and Shanhui Fan. Compact all-pass filters in photonic crystals as the building block for high-capacity optical delay lines. *Phys. Rev. E*, 68(6):066616, December 2003.

[175] Jian Liu, Bin Shi, Dengtao Zhao, and Xun Wang. Optical delay in defective photonic bandgap structures. *J. Opt. A.: Pure Appl. Opt.*, 4:636-639, October 2002.

[176] Hatice Altug and Jelena Vučković. Two-dimensional coupled photonic crystal resonator arrays. *Appl. Phys. Lett.*, 84(2):161–163, January 2004.

[177] Mehmet Fatih Yanik and Shanhui Fan. Stopping light all optically. *Phys. Rev. Lett.*, 92:083901, 2004.

[178] Shanhui Fan, Pierre R. Villeneuve, and J. D. Joannopoulos. Theoretical investigation of fabrication-related disorder on the properties of photonic crystals. *J. Appl. Phys.*, 78(3):1415–1418, August 1995.

[179] E. Lidorikis, M. M. Sigalas, E. N. Economou, and C. M. Soukoulis. Gap deformation and classical wave localization in disordered two-dimensional photonic-band-gap materials. *Phys. Rev. B*, 61(20):13458–13464, May 2000.

[180] A. A. Asatryan, P. A. Robinson, L. C. Botten, R. C. McPhedran, N. A. Nicorovici, and C. Martijn de Sterke. Effects of geometric and refractive index disorder on wave propagation in two-dimensional photonic crystals. *Phys. Rev. E*, 62(4):5711–5720, October 2000.

[181] Sharee J. McNab, Nikolaj Moll, and Yurii A. Vlasov. Ultra-low loss photonic integrated circuit with membrane-type photonic crystal waveguides. *Opt. Express*, 11(22):2927–2939, November 2004.

[182] E. Kuramochi, A. Shinya, and M. Notomi. Low propagation loss Si-based photonic crystals slab waveguides. In *Technical Digest, International Symposium on Photonic and Electromagnetic Crystal Structures V*, page 92, Kyoto, Japan, March 2004.

[183] N. Ikeda, Y. Sugimoto, Y. Tanaka, K. Asakawa, and K. Inoue. Low propagation losses in single-line-defect photonic crystal waveguides on gaas membranes. In *Technical Digest, International Symposium on Photonic and Electromagnetic Crystal Structures V*, page 91, Kyoto, Japan, March 2004.

[184] Jiřii Čtyroký. Photonic bandgap structures in planar waveguides. *J. Opt. Soc. Am. A*, 18(2):435–441, 2001.

[185] Wim Bogaerts, Peter Bienstman, Dirk Taillaert, Roel Baets, and Daniel De Zutter. Out-of-plane scattering in photonic crystal slabs. *IEEE Photonics Tech. Lett.*, 13(6):565–567, June 2001.

[186] H. Benisty, D. Labilloy, C. Weisbuch, C. J. M. Smith, T. F. Krauss, D. Cassagne, A. Béraud, and C. Jouanin. Radiation losses of waveguide-based two-dimensional photonic crystals: Positive role of the substrate. *Appl. Phys. Lett.*, 76(5):532–534, January 2000.

[187] G. Ronald Hadley. Out-of-plane losses of line-defect photonic crystal waveguides. *IEEE Photonics Tech. Lett.*, 14(5):642–644, May 2002.

[188] C. Sauvan, P. Lalanne, J. C. Rodier, J. P. Hugonin, and A. Talneau. Accurate modeling of line-defect photonic crystal waveguides. *IEEE Photonics Tech. Lett.*, 15(9):1243–1245, September 2003.

[189] Kevin K. Lee, Desmond R. Lim, Lionel C. Kimerling, Jangho Shin, and Franco Cerrina. Fabrication of ultralow-loss Si/SiO_2 waveguides by roughness reduction. *Opt. Lett.*, 26(23):1888–1890, December 2001.

[190] B. Z. Steinberg, A. Boag, and R. Lisitsin. Sensitivity analysis of narrowband photonic crystal filters and waveguides to structure variations and inaccuracy. *J. Opt. Soc. Am. A*, 20(1):138–146, January 2003.

[191] Wim Bogaerts, Peter Bienstman, and Roel Baets. Scattering at sidewall roughness in photonic crystal slabs. *Opt. Lett.*, 28(9):689–691, May 2003.

[192] Kai-Chong Kwan, Xiangdong Zhang, Zhao-Qing Zhang, and C. T. Chan. Effects due to disorder on photonic crystal-based waveguides. *Appl. Phys. Lett.*, 82(25):4414–4416, June 2003.

[193] T. N. Langtry, A. A. Asatryan, L. C. Botten, C. M. de Sterke, R. C. McPhedran, and P. A. Robinson. Effects of disorder in two-dimensional photonic crystal waveguides. *Phys. Rev. E*, 68(2):026611, August 2003.

[194] D. Marcuse. *Theory of Dielectric Optical Waveguides.* Academic Press, San Diego, second edition, 1991.

[195] D. G. Hall. Scattering of optical guided waves by waveguide surface roughness: a three-dimensional treatment. *Opt. Lett.*, 6(12):601–603, 1981.

[196] D. G. Hall. In-plane scattering in planar optical waveguides: refractive-index fluctuations and surface roughness. *J. Opt. Soc. Am. A*, 2(5):747–752, May 1985.

[197] F. P. Payne and J. P. R. Lacey. A theoretical analysis of scattering from planar optical waveguides. *Optical and Quantum Electron.*, 26:977–986, 1994.

[198] M. L. Povinelli, Steven G. Johnson, Shanhui Fan, and J. D. Joannopoulos. Emulation of two-dimensional photonic-crystal defect modes in a photonic crystal with a three-dimensional photonic band gap. *Phys. Rev. B*, 64:075313, July 2001.

[199] M. L. Povinelli, Steven G. Johnson, J. D. Joannopoulos, and J. B. Pendry. Toward photonic-crystal metamaterials: Creating magnetic emitters in photonic crystals. *Appl. Phys. Lett.*, 82(7):1069–1071, February 2003.

[200] M. L. Povinelli, Steven G. Johnson, Elefterios Lidorikis, J. D. Joannopoulos, and Marin Soljačić. Effect of a photonic bandgap on scattering from waveguide disorder. *Appl. Phys. Lett.*, 84(18):3639–3641, 2004.

[201] M. L. Povinelli, Mihai Ibanescu, Steven G. Johnson, and J. D. Joannopoulos. Slow-light enhancement of radiation pressure in an omnidirectional-reflector waveguide. In review, 2004.

[202] M. L. Povinelli, Steven G. Johnson, and J. D. Joannopoulos. Slow-light, band-edge waveguides for tunable time delays. In review, 2004.

[203] C. M. Soukoulis, editor. *Photonic Crystals and Light Localization*, Dordrecht, 2001. Kluwer Academic. Proceedings of the NATO ASI on Photonic Band Gap Materials, Limin Hersonissou, Crete, Greece, 19–30 June 2000.

[204] Pierre R. Villeneuve, Shanhui Fan, and J. D. Joannopoulos. Microcavities in photonic crystals: Mode symmetry, tunability, and coupling efficiency. *Phys. Rev. B*, 54(11):7837–7842, September 1996.

[205] P. R. Villeneuve, S. Fan, S. G. Johnson, and J. D. Joannopoulos. Three-dimensional photon confinement in photonic crystals of low-dimensional periodicity. *IEE Proc. Optoelectron.*, 145(6):384–390, December 1998.

[206] R. Coccioli, M. Boroditsky, K. W. Kim, Y. Rahmat-Samii, and E. Yablonovitch. Smallest possible electromagnetic mode volume in a dielectric cavity. *IEE Proc. Optoelectron.*, 145(6):391 397, December 1998.

[207] Mario Agio, Elefterios Lidorikis, and Costas M. Soukoulis. Impurity modes in a two-dimensional photonic crystal: coupling efficiency and Q factor. *J. Opt. Soc. Am. B*, 17(12):2037–2042, December 2000.

[208] C. J. M. Smith, T. F. Krauss, H. Benisty, M. Rattier, C. Weisbuch, U. Oesterle, and R. Houdré. Directionally dependent confinement in photonic-crysal microcavities. *J. Opt. Soc. Am. B*, 17(12):2043–2051, December 2000.

[209] R. D. Meade, A. M. Rappe, K. D. Brommer, J. D. Joannopoulos, and O. L. Alerhand. Accurate theoretical analysis of photonic band-gap materials. *Phys. Rev. B*, 48:8434-8437, 1993. Erratum: S. G. Johnson, *ibid.* **55**, 15942 (1997).

[210] Vladimir A. Mandelshtam and Howard S. Taylor. Harmonic inversion of time signals and its applications. *J. Chem. Phys.*, 107(17):6756–6769, November 1997. See erratum [226].

[211] J. D. Jackson. *Classical Electrodynamics*. Wiley, New York, third edition, 1998.

[212] J. D. Jackson. *Classical Electrodynamics*. Wiley, New York, second edition, 1975.

[213] M. I. Antonoyiannakis and J. B. Pendry. Electromagnetic forces in photonic crystals. *Phys. Rev. B*, 60(4):2363-2374, July 1999.

[214] M. L. Povinelli, Steven G. Johnson, and J. D. Joannopoulos. Optical forces between waveguides. In preparation, 2004.

[215] M. Scalora, R. J. Flynn, S. B. Reinhardt, R. L. Fork, M. J. Bloemer, M. D. Tocci, C. M. Bowden, H. S. Ledbetter, J. M. Bendickson, and R. P. Leavitt. Ultrashort pulse propagation at the photonic band edge: Large tunable group delay with minimal distortion and loss. *Phys. Rev. E*, 54(2):R1078–1081, August 1996.

[216] Steven G. Johnson, Peter Bienstman, M. A. Skorobogatiy, Mihai Ibanescu, Elefterios Lidorikis, and J. D. Joannopoulos. Adiabatic theorem and continuous coupled-mode theory for efficient taper transitions in photonic crystals. *Phys. Rev. E*, 66:066608, December 2002.

[217] J. T. Hastings, Michael H. Lim, J. G. Goodberlet, and Henry I. Smith. Optical waveguides with apodized sidewall gratings via spatial-phase locked electron-beam lithography. *J. Vac. Sci. Technol. B*, 20(6):2753–2757, Nov/Dec 2002.

[218] G. E. Jellison and H. H. Burke. The temperature depdendence of the refractive index of silicon at elevated temperatures at several laser wavelengths. *J. Appl. Phys.*, 60(2):841–843, July 1986.

[219] Merrill I. Skolnik. *Introduction to Radar Systems*, chapter 11.5. McGraw-Hill, 1980.

[220] S. J. Spector, M. W. Geis, and T. Lyszczarz. private communication.

[221] P. St. J. Russell. Bragg resonance of light in optical superlattices. *Phys. Rev. Lett.*, 56(6):596 599, February 1986.

[222] C. Martijn de Sterke, David G. Salinas, and J. E. Sipe. Coupled-mode theory for light propagation through deep nonlinear gratings. *Phys. Rev. E*, 54(2):1969–1989, August 1996.

[223] Kevin K. Lee, Desmond R. Lim, Hsin-Chiao Luan, Anuradha Agarwal, James Foresi, and Lionel C. Kimerling. Effect of size and roughness on light transmission in a Si/SiO_2 waveguide: Experiments and model. *Appl. Phys. Lett.*, 77(11):1617–1619, September 2000. See Erratum [227].

[224] Steven G. Johnson, M. Ibanescu, M. Skorobogatiy, O. Weisberg, J. D. Joannopoulos, and Y. Fink. Perturbation theory for Maxwell's equations with shifting material boundaries. *Phys. Rev. E*, 65(6):066611, June 2002.

[225] Wah Tung Lau and Shanhui Fan. Creating large bandwidth line defects by embedding dielectric waveguides in photonic crystal slabs. *Appl. Phys. Lett.*, 81(21):3915 3917, November 2002.

[226] Vladimir A. Mandelshtam and Howard S. Taylor. Erratum: "Harmonic inversion of time signals and its applications". *J. Chem. Phys.*, 109(10):4128, September 1998.

[227] Kevin K. Lee, Desmond R. Lim, Hsin-Chiao Luan, Anuradha Agarwal, James Foresi, and Lionel C. Kimerling. Erratum: Effect of size and roughness on light

transmission in a Si/SiO_2 waveguide: Experiments and model. *Appl. Phys. Lett.*, 77(14):2258, October 2000.